QUANTITATIVE MODELLING OF AUTOPHAGY-RELATED PROTEIN DYNAMICS AND CLUSTERING ON PEROXISOME SURFACES

by

Aidan I Brown

Submitted in partial fulfillment of the
requirements for the degree of
Doctor of Philosophy

at

Dalhousie University
Halifax, Nova Scotia
August 2015

Table of Contents

List of Tables

List of Figures

Abstract

Autophagy is an important process for the degradation of large cellular substrates, such as organelles. Peroxisomes are membrane-bound organelles ranging in size from 0.1-0.8 μm. There can be hundreds of peroxisomes in a single mammalian cell, necessitating regulation of peroxisome numbers, including through degradation by autophagy. Peroxisome autophagy, known as pexophagy, has been shown to be mediated by the common signalling protein ubiquitin, and the autophagy receptor proteins NBR1 and p62. We consider each of ubiquitin, NBR1, and p62 in turn. First, ubiquitin is also involved in the import cycle for peroxisome matrix proteins, and so we quantitatively model the import cycle for systems with ensembles of peroxisomes, each with many import complexes. We consider three different coupling schemes to energetically drive the translocation of matrix proteins across the membrane, and find that our proposed 'cooperative coupling' scheme best agrees with existing experimental phenomenology and provides a ubiquitin signal that plausibly signals for peroxisome degradation. Next, NBR1 is the primary autophagy receptor protein for peroxisomes, and recent evidence suggests autophagy receptor proteins can cluster on substrates. Motivated by the possibility of NBR1 clusters on peroxisomes, we model the dynamics of clusters on polydisperse ensembles of spherical drops. The clusters exhibit Lifshitz-Slyozov-Wagner coarsening behaviour, with the cluster scaling function dependent on the drop radius distribution. Large drops are selected for cluster growth, and small drops for cluster evaporation, so that at late times only the largest drops harbour clusters — this suggests that NBR1 clusters may select large peroxisomes for degradation. Finally, adding cluster formation, ubiquitin recruitment of NBR1, and p62 chains on NBR1 and ubiquitin to the model intensifies the selection of large peroxisomes for NBR1 clusters. Overall, we have shown that signalling for peroxisome degradation through autophagy can self-organize in time and to select a subset of peroxisomes for degradation.

List of Abbreviations and Symbols Used

AAA	ATPases Associated with various cellular Activities
ATP	Adenosine triphosphate
ER	Endoplasmic reticulum
LSW	Lifshitz-Slyozov-Wagner
mPTS	Membrane peroxisome targeting signal
PMP	Peroxisome membrane protein
PTS	Peroxisome targeting signal
RING	Really interesting new gene

Acknowledgements

I would like to thank everyone that has inspired, helped, and been patient with me during my research and work on this thesis. Without everyone named below and unnamed everywhere else, all the work on this thesis would have been less enjoyable and less successful.

I thank my parents. Thank you for supporting me when I moved to, and decided to stay longer in, Halifax. Thank you for always asking about my research even though my explanation might not make any sense. Thank you for feeling proud enough to put my bound Masters on the nice table in the living room that is not allowed to have anything on it — I hope this also makes the cut.

I thank my girlfriend and primary ultimate frisbee critic, Allison. Thank you for reminding me to both take a break when the work is piling high and that I have to keep plugging away when a deadline is drawing nigh. Thank you for listening when I am stuck or confused, and I feel the need explain everything to death. Thank you for listening when I think I know what is going on and just want to tell someone. Thank you for all the things you do that are not specific to writing a thesis, but surely helped me on my way.

Last, but certainly not least, I thank my supervisor Andrew Rutenberg. Thank you for doing things at the last minute when I let you know about them at the second-to-last minute. Thank you for not throwing up when I explained my injured knee. Thank you for not failing to tactfully point out my weaknesses, patiently and repeatedly explaining why it is worth acknowledging and working on each one, and pushing me to strive to turn them into strengths. Thank you for your patience, especially when I am stubborn, both when I come around and when I do not. Thank you for endlessly reminding me, in many ways, to do my best. Thank you for your relentless constructive criticism. Thank you for never letting up at being a fantastic supervisor.

Chapter 1

Introduction

1.1 Motivation

This thesis focuses on the biological process of autophagy, in particular the accumulation of molecules during autophagy signalling of peroxisomes. While the selection of peroxisomes for autophagy is inherently a biological process, this does not mean that physics does not play an important role. The mathematician Ian Stewart has said, *"Nobody is silly enough to think that an elephant will only fall under gravity if its genes tell it to do so, but the same underlying error can easily be made in less obvious circumstances. So we must distinguish between how much behaviour, and what part, has a genetic origin, and how much comes solely because an organism lives in the physical universe and is therefore bound by physical laws."* [1]

Much of our understanding of biological cells is about how cells build things. The things cells build do not last forever and cells have finite resources, and so there are significant advantages to recycling what they have previously built. Therefore, understanding how peroxisomes and other cellular substrates are selected for degradation is essential to understanding how our cells work.

How does the cell 'know' which peroxisomes to get rid of and which ones to keep? It is thought that accumulation of certain proteins on peroxisomes will signal for their degradation. This thesis argues that these proteins accumulate on peroxisomes because of simple physical rules, which govern the protein dynamics.

To further motivate the topic of my thesis, we first answer the questions why autophagy, why peroxisomes, and why physics?

1.1.1 Why Autophagy?

Autophagy, or 'self eating', refers to cellular catabolic processes that involve transport of substrates to the lysosome to be degraded [2]. Autophagy is important to

understanding diseases such as cancer [3] and those that cause neurodegeneration [4], among others.

Until recent years, autophagy was thought to be a non-selective process for the degradation of large cellular substrates [5]. However, autophagy has been shown to be capable of selective degradation of substrates, mediated by what are known as autophagy receptor proteins [6]. Selective autophagy is one of the developments that has made autophagy a hot research topic in recent years [7].

Some recent advances in the understanding of autophagy are important to this work. It has been shown that there is some crossover with another cellular degradation system, the proteasome [8]. Although ubiquitin had been thought only part of the proteasome system, it plays a role in autophagy as well [8]. Importantly, autophagy receptor proteins are capable of clustering in segregated domains on substrates [9, 10].

1.1.2 Why Autophagy of Peroxisomes (Pexophagy)?

To understand why peroxisomes are a good choice for an investigation of autophagy, we first go over a very brief and selective background on peroxisomes.

Peroxisomes are roughly spherical organelles [11] in eukaryotic cells [12], ranging from approximately 0.1 - 0.8μm in diameter [13]. Peroxisomes, as with many other organelles, are bounded by a phospholipid membrane [12]. Proteins in the interior of the peroxisome, a volume known as the peroxisome matrix, perform a variety of important reactions [14]. Peroxisomes also have outward facing proteins embedded in the membrane [15] — many of these membrane proteins participate in the import of proteins to the peroxisome matrix or membrane [16, 15], or play a role in peroxisome division [17] or, important to us, peroxisome degradation [18, 19].

There can be hundreds of peroxisomes in a single cell [20], and thus peroxisome numbers need to be regulated. Peroxisome numbers are increased by division of existing peroxisomes or *de novo* formation from the endoplasmic reticulum [21]. Instead of processes that increase peroxisome numbers, we focus on the decrease of peroxisome numbers by their degradation.

Peroxisome degradation occurs primarily through the autophagy system, with the autophagy of peroxisomes known as 'pexophagy' [19]. Ubiquitin is a common signalling protein [22], and has clearly been shown to play a role in signalling for

degradation of peroxisomes [18]. Autophagy receptor proteins can interact with the proteins of the autophagy system [6]. The autophagy receptor protein NBR1 has been shown to be both necessary and sufficient for pexophagy [19], with another receptor protein, p62, also playing a role [18, 19].

Peroxisomes have a simple spherical geometry and a short list of activities occurring on their membranes, allowing for relatively straightforward modelling of ubiquitin and autophagy receptor protein accumulation. Peroxisomes can also be present in large numbers, suggesting that the processes involved in regulating their number, including degradation by autophagy, are routine and likely lack complex and infrequent initiation mechanisms, such as those required by cell division. The proteins involved in pexophagy are known with little ambiguity: ubiquitin and the autophagy receptor proteins NBR1 and p62, all three of which are well-studied.

1.1.3 Why Physics of Pexophagy?

Recent developments in autophagy and the characteristics of peroxisomes combine to make investigating pexophagy appealing. These topics are also appealing as the subject of a physical model.

As mentioned above, peroxisomes are relatively straightforward to model. Rather than the stereotypical 'spherical cow in a vacuum', peroxisomes may be considered 'spheres in a uniform medium' much more appropriately than many other organelles, due to their relatively small size, abundance, and simple shape. Large numbers also allow average or typical behaviour to be generalized, which cannot always be said for small numbers when stochastic processes are involved.

The proteins we consider that are involved in autophagy — ubiquitin, NBR1, and p62 — are either quite common or have a specific role. For example, ubiquitin, as its name suggests, is involved in many processes in the cell. In contrast, NBR1 seems to primarily be an autophagy receptor protein for specific substrates. These two extremes allow other influences to be ignored — for ubiquitin because our considered processes will change background levels little, and for NBR1 because we may assume the model includes the only relevant process.

The above three paragraphs argue that our system is straightforward enough for a physical model to be relevant. But why is the accumulation of autophagy proteins

on peroxisomes compelling? I think it is a perfect example of trying to understand how a cell 'knows' what to do next. Understanding the accumulation of autophagy proteins literally tells us (or at least brings us a step closer to) how the cell 'knows' which peroxisome to get rid of next.

The choice of system actually lets us address the question, rather than just pose it. The accumulation of ubiquitin and autophagy receptor proteins appears to occur with relatively straightforward component parts. They seem capable of selective control and prone to physical mechanisms. This lets us look at this system as self-organizing.

1.2 Hypotheses

Self-organization hypotheses are common in the biological physics literature. For example, periodic clusters of proteins are thought to self-organize [23], telomere lengths can be maintained without telomerase [24], and DNA repair proteins collectively control the repair rate [25]. The overarching hypothesis in this work is that for the biological processes we model, there is self-organization of the known components — ubiquitin, NBR1, and p62.

For the first paper, in Chapter 4, we hypothesize that the translocation of cargo proteins across the peroxisome membrane is cooperatively coupled to the ATP hydrolysis-driven export of Pex5 from the peroxisome membrane. By cooperative coupling, we mean that more than one Pex5 is involved — the cargo protein bound to one Pex5 is translocated, while a distinct Pex5 is exported. Chapter 4 explores how the cooperative coupling hypothesis can allow for ubiquitin accumulation on the matrix protein import machinery that could plausibly signal for peroxisome degradation by autophagy.

In the second paper, in Chapter 5, we hypothesize that the autophagy receptor protein NBR1, which is thought to bind to the surface of peroxisomes, can form two-dimensional clusters on the surface of peroxisomes. Chapter 5 investigates the dynamics of the hypothesized NBR1 clusters.

Chapter 6 expands on the hypothesis of NBR1 clusters from chapter 5, including a second autophagy receptor protein, p62. Chains of p62 on peroxisome membrane-bound NBR1 are hypothesized to sterically inhibit the participation of those NBR1 in cluster formation and growth. Chapter 6 considers how this p62 chain steric inhibition

hypothesis could affect the formation and dynamics of NBR1 clusters on peroxisome membranes.

1.3 Outline

This thesis is in publication format, with three related papers. These papers are found in chapters 4, 5, and 6. The three 'paper' chapters are preceded and followed by chapters 3 and 7, respectively, to integrate the papers into this thesis.

Chapter 2 provides a background to understanding the work of the following chapters. It covers relevant information about peroxisomes, autophagy, coarsening, diffusion-limited rates, and computational methods.

Chapter 4 describes a stochastic model of the matrix protein import system of peroxisomes, tracking both ubiquitin and the shuttle protein PEX5. We demonstrate that the matrix protein production can control the ubiquitin level on the surface of peroxisomes. We argue that the response of ubiquitin levels to matrix protein production could play a role in regulating peroxisome numbers, as the ubiquitin level contributes to autophagy signalling. This work is published as 'PEX5 and ubiquitin dynamics on mammalian peroxisome membranes', authored by Aidan I Brown (myself), Peter K Kim, and Andrew D Rutenberg, in PLoS Computational Biology in 2014, volume 10, page e1003426, doi 10.1371/journal.pcbi.1003426.

Chapter 5 investigates the growth and evaporation of coarsening clusters on the surface of spherical drops. This investigation is a model for NBR1 clusters on peroxisomes. We find that clusters on sphere surfaces exhibit Lifshitz-Slyozov-Wagner coarsening characteristics. Large drops are selected for cluster growth, while clusters on small drops evaporate, suggesting that NBR1 clusters naturally select large peroxisomes for degradation. This work is published as 'Cluster coarsening on drops exhibits strong and sudden size-selectivity', authored by Aidan I Brown (myself) and Andrew D Rutenberg, published in Soft Matter in 2015, volume 11, pages 3786-3793, doi 10.1039/C5SM00284B.

Chapter 6 adds to the work of chapter 5 by modelling cluster formation and including a second autophagy receptor protein, p62. p62 is taken to inhibit cluster formation and growth. Allowing cluster formation leads to two clear populations of peroxisomes: one population with many receptor proteins and one population with

few receptor proteins. p62 inhibition of clusters leads to stricter size selectivity, pushing clusters to remain on only the largest peroxisomes. This paper is currently in draft form, and we are planning to submit in the summer of 2015.

Chapter 8 discusses the overall themes and speculates on future work.

Chapter 2

Background

2.1 Peroxisomes

Peroxisomes are roughly spherical [11] single membrane organelles found in most eukaryotic cells [12], ranging from approximately 0.1-0.8 μm in diameter [13]. An electron micrograph of a peroxisome is shown in Figure 2.1. In yeast cells the number of peroxisomes varies between approximately one and twenty [26], while mammalian cells can have hundreds of peroxisomes [20]. Peroxisomal defects are associated with disorders such as Zellweger syndrome and adrenoleukodystrophy [27], and may play a role in neurodegeneration [28].

As a single membrane organelle that does not form multi-organelle dynamic networks [20], peroxisomes can be viewed as bags of enzymes that perform reactions. The metabolites for these reactions are able to cross the peroxisome membrane, with peroxisome membranes permeable small metabolites up to 300-400 Da [30], and specific transport proteins for other substrates [31, 32, 33]. The enzymes that perform the reactions must be imported [16] - these proteins are not exchanged between peroxisomes [20] and therefore do not escape the matrix (matrix is the name of the interior of peroxisomes) once imported. Peroxisomes play a role in many anabolic and catabolic pathways, and common functions between mammals, plants, and yeast include the metabolism of hydrogen peroxide and the oxidation of fatty acids [14]. In humans peroxisomes are also involved in synthesis of plasmalogens (lipids) and bile acids, among participation in many other processes [34]. A significant feature of peroxisomes in many species is a crystalline core of urate oxidase, an enzyme for the oxidation of uric acid, seen in Figure 2.1, one of many reactions which produce hydrogen peroxide [35]. Despite being a bag of enzymes, the number of the enzymes and substrates in peroxisomes needs to be maintained and regulated to meet cellular needs.

Below we detail the biological background of peroxisome matrix and membrane

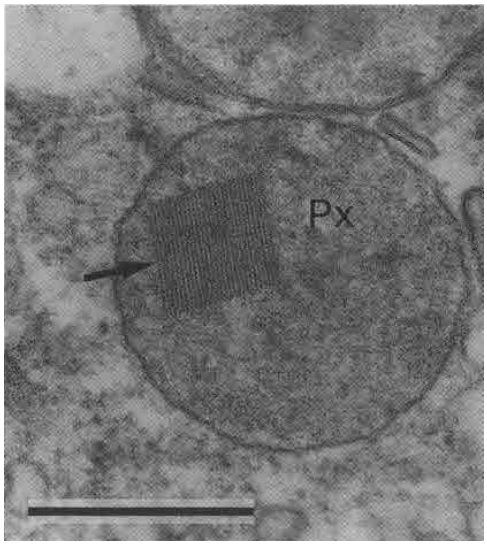

Figure 2.1: **Peroxisome.** An electron micrograph of a peroxisome from Ref. [29]. The roughly circular somewhat dark region labelled 'Px' is the peroxisome, and the roughly square, darker lined region inside the circular region is a urate oxidase crystal. Scale bar is 0.5 μm.

protein import, as well as processes that create new peroxisomes and those that degrade existing peroxisomes. We focus on matrix protein import and degradation, as these are areas of focus later in this thesis. In our subsequent modelling we will considerably simplify the biology below. When necessary, we limit our attention to mammalian processes.

2.1.1 Two Experimental Systems

Experiments investigating peroxisomes are typically performed on either mammalian cells or yeast cells. Mammalian cells yield results that are more relevant to human health, but are relatively difficult to culture. Results from yeast cells are less relevant to human health, but yeast cells are easy to culture. Although what is known about peroxisomes is similar in mammals and yeast, there are significant differences. For example, mammalian cells typically have many more peroxisomes than yeast cells. The exact proteins of the peroxisome matrix protein import system and their localization differ between mammals and yeast. The exact proteins for peroxisome autophagy and their domain structure are distinct in mammals and yeast. These differences and others are included in the discussion below.

2.1.2 Matrix Protein Import

Peroxisomes do not contain DNA or transcription/translation machinery, with all peroxisomal matrix proteins produced by ribosomes in the cytosol and imported post-translationally [16, 36]. The basic idea is that a shuttle protein, usually Pex5, binds to peroxisome matrix proteins and guides them through the import process until they are translocated across the peroxisome membrane into the matrix. A cartoon of the matrix protein import cycle is shown in Figure 2.2.

I begin with a pre-emptive summary, so that the details are anchored to an overall picture.

A matrix protein in the cytosol binds to a shuttle protein, which can then dock at an importomer on the peroxisome membrane. The shuttle protein is ubiquitinated, either by a cytosolic enzyme or by an enzyme associated with the peroxisome membrane. Monoubiquitination signals for export, and an export complex, distinct from the importomer, can export the ubiquitinated shuttle protein. At some time prior to the return of the shuttle protein to the cytosol, the peroxisome matrix protein is translocated across the peroxisome membrane. Either late in the export process, or after returning to the cytosol, the shuttle protein is deubiquitinated and is ready for another import cycle with a new peroxisome matrix protein. Shuttle proteins may also be polyubiquitinated to signal for degradation.

Matrix Protein Targeting and Shuttle Proteins

Most peroxisome matrix proteins have an amino acid sequence allowing them to interact with a shuttle protein, known as a peroxisome targeting signal (PTS) [16]. There are two targeting sequences, PTSI and PTSII [16], with most proteins containing PTSI [38]. In mammals, few proteins are targeted using PTSII, and in yeast only two PTSII proteins have been identified, but in plants approximately one-third of proteins contain PTSII [16]. Some proteins do not contain a peroxisome targeting signal and these proteins interact with a shuttle protein in a non-PTS manner or piggy-back on proteins that do contain a PTS [37].

Peroxisome matrix proteins are guided through the import process by a shuttle protein [37, 16]. The most common shuttle protein is Pex5, which binds PTSI proteins [38, 16]. PTSII proteins interact with Pex7, but require species-specific co-receptors to

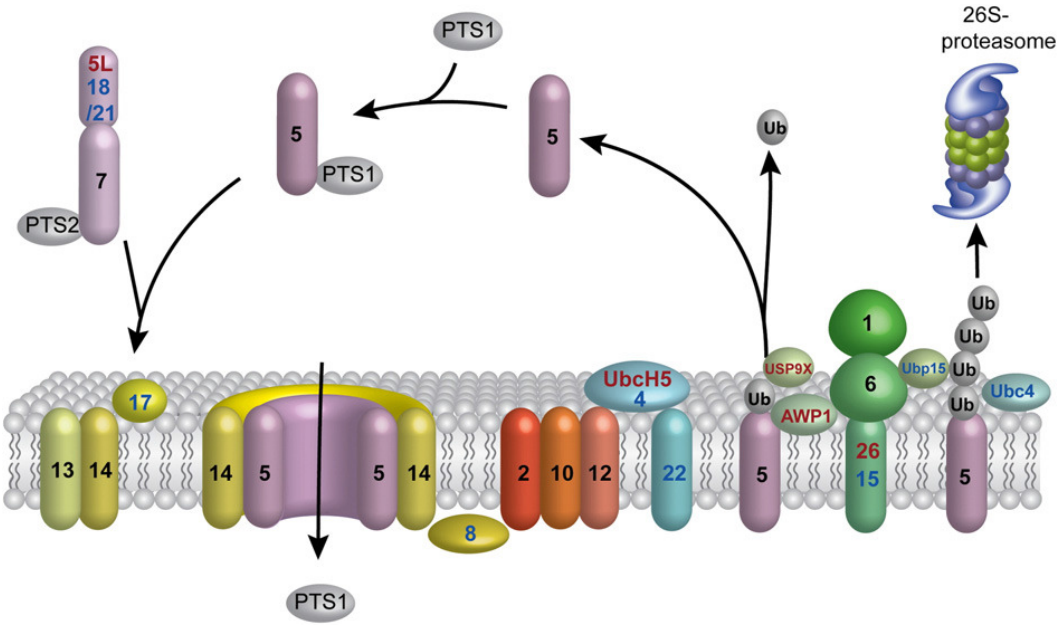

Figure 2.2: **Matrix Protein Import** A biological cartoon of the matrix protein import process, taken from Ref. [37]. The peroxisome membrane is shown with embedded peroxisome membrane proteins — above the membrane is the cytosol, and below is the peroxisome matrix. Peroxisome matrix proteins to be imported are shown as grey ovals, and shuttle proteins and their co-receptors as purple pill shapes — all proteins are labelled with characteristic numbers of characters, such as '5' for Pex5. Many peroxisome matrix proteins contain peroxisome targeting signal 1 (PTS1), allowing import with Pex5 as the shuttle protein. Peroxisome matrix proteins may also contain peroxisome targeting signal 2 (PTS2), allowing import with shuttle protein Pex7 and a co-receptor, such as Pex5L, Pex18, or Pex21. Once a shuttle protein has bound a peroxisome matrix protein in the cytosol, it can dock at a complex of peroxisome matrix proteins containing Pex13, Pex14, and sometimes Pex17. Pex5 (or the shuttle protein used) and Pex14 have been suggested as the proteins which form a translocon to translocate the peroxisome matrix protein across the peroxisome membrane and into the peroxisome matrix. Pex8 can connect the docking proteins to the RING complex, comprised of Pex2, Pex10, and Pex12, which are thought to be ubiquitin ligases, participating in the final stage of ubiquitination, or attachment of ubiquitin. Ubiquitin will be held by a ubiquitin conjugase, which can vary with species and ubiquitination type. Pex22 anchors Pex4, a ubiquitin conjugase, to the membrane in yeast, and in mammals UbcH5 is a cytosolic ubiquitin conjugase — these monoubiquitinate Pex5. Monubiquitinated Pex5 is labelled for routine export from the peroxisome membrane, and the export complex, composed of Pex1 and Pex6 and anchored to the peroxisome membrane by Pex26 in mammals and Pex15 in yeast, will use ATP to remove the monoubiquitinated Pex5 from the membrane. Ubc4 is a ubiquitin conjugase for Pex5 polyubiquitination, which labels the shuttle protein for degradation by the proteasome. Pex5 is deubiquitinated by USP9X in the cytosol in mammals, and by Ubp15 at the end of export in yeast. After Pex5 and other shuttle proteins have been deubiquitinated and returned to the cytosol, they may begin the import cycle with a new matrix protein. Figure is not to scale.

interact with the peroxisome import machinery [16] — in yeast these co-receptors are Pex18, Pex20, and Pex21 [16, 39], and in mammals the co-receptor is Pex5 [16, 40, 41]. In mammals not all Pex5 proteins can bind Pex7, with transcribed Pex5 mRNA either encoding a long isoform which binds Pex7, Pex5L, or a short isoform that cannot bind Pex7, Pex5S [40].

Pex5 and other shuttle proteins cannot bind to the matrix protein import machinery on the peroxisome membrane without a bound 'cargo' peroxisome matrix protein [42]. The proteins that are part of the peroxisome matrix protein import machinery are thought to organize into what are known as 'importomers' [43]. An importomer contains docking proteins, usually at least Pex13 and Pex14 [16, 44, 43], as well as Pex2, Pex10, and Pex12, which together are known as the RING (Really Interesting New Gene) complex [16, 44].

Shuttle Protein Ubiquitination

Ubiquitination of a protein requires the sequential activity of three enzymes: a ubiquitin activating enzyme (E1), followed by a ubiquitin conjugating enzyme (E2), followed by a ubiquitin ligating enzyme (E3) [45]. The E1 activates the ubiquitin with ATP [16, 41], passes the ubiquitin to the E2, and the E3 binds the substrate and the E2 to attach the ubiquitin to the substrate [46].

The E1 is very general, and in yeast ubiquitin is activated by UBA1, the only E1 in yeast [41]. There are two types of shuttle protein ubiquitination [39], known as monoubiquitination and polyubiquitination [39], which require different E2 conjugases and E3 ligases [47]. We will first outline monoubiquitination, as it is the more routine process, and then return to polyubiquitination.

First we summarize the distinction between monoubiquitination and polyubiquitination of Pex5. Monoubiquitination signals for the routine export of Pex5 from the peroxisome membrane so it can facilitate further protein import, while polyubiquitination signals for protein degradation. Monoubiquitination and polyubiquitination have overlapping numbers of ubiquitin attached (1-3 and 1-4, respectively) — the real distinction is in the location of the ubiquitination, with Pex5 ubiquitinated at a cysteine for monoubiquitination, and at a lysine for polyubiquitination. In yeast and plants, monoubiquitination uses a E2 ligase attached to the peroxisome membrane,

with polyubiquitination using a cytosolic E2 ligase. In mammals, both E2 ligases are cytosolic.

Monoubiquitination generally means the attachment of 1-3 ubiquitins and can mean a change of activity or cellular location [39]. In the case of Pex5, the import shuttle protein, the E2 conjugase attaches 2 ubiquitins [48]. In yeast and plants, Pex5 is monoubiquitinated by the E2 Pex4 [44, 41, 49, 50], which is attached to the peroxisome membrane by Pex22 [50]. In mammals, peroxisomes lack their own E2 and Pex5 is monoubiquitinated by the cytosolic E2D1/2/3 (also known as UbcH5a/b/c) [44, 41]. The RING complex is essential for monoubiquitination, with deficiency in a single RING component, either Pex2, Pex10, or Pex12, leading to complete inhibition of monoubiquitination [51], likely because the RING complex degrades if one of the three proteins is absent, suggesting the three RING complex proteins stabilize one another [51]. Many sources support Pex12 as the E3 ligase for Pex5 monoubiquitination [44, 51], although it has been suggested that Pex10 is the E3 for Pex5 monoubiquitination [41]. Monoubiquitination of Pex5 occurs by attaching ubiquitin to a cysteine with a thioester bond [45, 52, 39] (it seems ubiquitination of a cysteine is unusual [48]). The purpose of Pex5 monoubiquitination is to signal for Pex5 export from the peroxisome membrane so that Pex5 may repeat the import cycle [49, 45, 38].

Polyubiquitination is typically the attachment of four or more ubiquitins, and usually results in the degradation of a protein by the 26S proteasome [39]. In the case of Pex5, one to four ubiquitins are attached to two lysine residues [45, 48], and this is performed by a distinct E2 conjugase from monoubiquitination [39]. With polyubiquitination signalling for degradation by the proteasome, the process is important for the quality control of Pex5, removing proteins that are arrested or entangled [49]. Pex5 that is not released from the importomer will be polyubiquitinated and degraded [14]. Both Pex2 [51] and Pex10 [47] have been suggested as the E3 ligase for Pex5 polyubiquitination, and, as with monoubiquitination, no polyubiquitination of Pex5 occurs in the absence of any of the three RING complex proteins [51].

Shuttle Protein Export

Ubiquitinated Pex5 can be recognized by the export machinery to be removed from the peroxisome membrane [45].

Pex1 and Pex6 are AAA (ATPases Associated with various cellular Activities) proteins that export Pex5. In mammals Pex26 attaches Pex1 and Pex6 to the peroxisome membrane [53], while in yeast this role is performed by Pex15 [44]. Pex1 and Pex6 are not permanently localized to the peroxisome, but are recruited from and released to the cytosol [44, 53, 54]. The export complex composed of Pex1, Pex6, and Pex15/26 transiently associates with the importomer [54]. Export of Pex5 from the peroxisome membrane by the export complex requires ATP and therefore costs energy [44, 53, 54].

Before Pex5 is ready for another import cycle, it must be deubiquitinated. In mammals Pex5 is deubiquitinated in the cytosol by the deubiquitinase Usp9X, however knocking down most of this deubiquitinase does not induce a peroxisomal protein import defect, suggesting it can also be deubiquitinated by other enzymes [55]. In yeast Pex5 is deubiquitinated by Ubp15, which can be associated with peroxisomes and interact with Pex6 [45].

Cargo Protein Translocation

In this section we have mostly focused on the shuttle protein, which is typically Pex5. This is because the actual translocation of cargo proteins across the peroxisome membrane is not well understood.

Pex5 has the properties of a pore-forming intrinsic membrane protein, and Pex5 and Pex14 (one of the docking proteins) can form a transient pore opening up to a diameter of 9nm [16, 43, 56]. Translocation of a 9 nm colloidal gold has been demonstrated, indicating that the properties of the cargo are likely not important [57]. Pex5 and Pex14 have been found in complexes in a 1:1 ratio, and the Pex14 binding domain of Pex5 spends part of the import cycle exposed to the peroxisome matrix [56]. Overall it seems that one or more Pex5 play a role in providing a channel for a cargo protein to translocate, possibly with Pex14.

There are questions over how the cargo protein could be released into the peroxisome matrix. It has been suggested that Pex8 could be involved in release [16, 38, 58],

but Pex8 is only found in yeast, and so this provides no release mechanism for mammals. It has also been suggested that Pex14 [38] or an unidentified protein [40] could release the cargo protein. Also suggested is that the Donnan effect (charged particles near a semi-permeable membrane do not evenly distribute on both sides) [40] or a pH gradient [58] could release the cargo protein, which could be consistent with a pH gradient between the cytosol and the peroxisome matrix [59] and observations that Pex5 binding behaviour with cargo proteins and importomer proteins depends on pH [60].

There is also the question of how energy is provided for cargo protein translocation. This question is central to chapter 4. It has even been suggested that there is no direct provision of energy and that translocation is simply thermodynamically favoured, due to a report that translocation occurs prior to ubiquitination [40]. It has also been more reasonably proposed that cargo translocation is energetically coupled to export of Pex5 by the AAA complex, since the AAA complex is the only known ATP-consuming process in peroxisomes [61, 62, 63].

2.1.3 Membrane Protein Import

Here we provide some detail on the import of peroxisomal membrane proteins (PMPs). Although we do not model this process in the thesis, peroxisomal membrane proteins are important to all the model processes we do investigate. Chapter 4 models the import of peroxisome matrix proteins — this involves many different peroxisome membrane proteins. Chapters 5 and 6 model the dynamics of peroxisome autophagy receptor proteins NBR1 and p62, which are recruited by ubiquitin, which is attached to a peroxisome membrane protein. This section also provides context and completeness. Peroxisomes are made from matrix proteins, membrane proteins, and membrane, and so some background on membrane proteins provides a better picture of peroxisomes as a whole. Part of why we have not modelled the dynamics of peroxisome membrane proteins, besides opportunity cost, is that their import process is quite controversial and may include significant involvement of other organelles such as the endoplasmic reticulum, complicating an already challenging modelling process.

The import of peroxisomal membrane proteins uses a different process from the

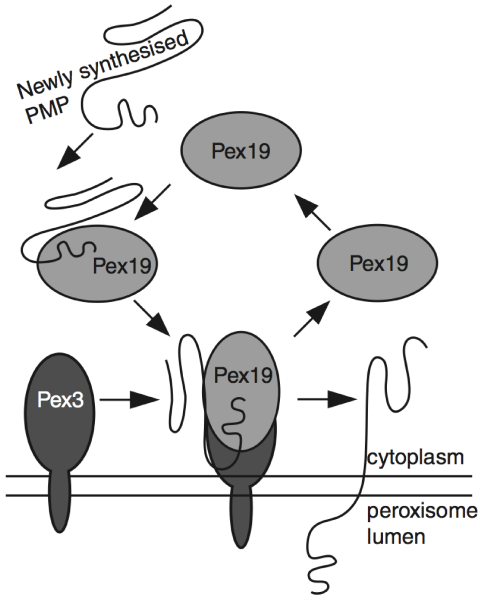

Figure 2.3: **Class II Membrane Protein Import** Cartoon of class II peroxisome membrane protein (PMP) import from Ref. [64]. A PMP in the cytosol binds to the shuttle protein Pex19. Pex19 can then dock at Pex3 on the peroxisome membrane. Once the new PMP has integrated into the cell membrane, the Pex19 can return to the cytosol to begin the import cycle with another PMP. Note that the peroxisome matrix and lumen are both terms that refer to the peroxisome interior.

import of peroxisome matrix proteins. PMPs can be imported by two distinct pathways. Class I PMPs are sent to the endoplasmic reticulum (ER) before being directed to peroxisomes, while Class II PMPs are imported to peroxisomes directly from the cytosol [65, 20].

Class I PMPs are transported to the peroxisome via the ER [26, 16, 55, 64]. It has been demonstrated that Pex16 is imported co-translationally into the ER membrane and then trafficked to the peroxisome [16], and there is some evidence that transport of peroxisomal proteins from the ER is linked to N- or O-linked glycosylation of the proteins [58].

Class II PMPs (see Figure 2.3) have a membrane peroxisome targeting signal (mPTS) which is recognized in the cytosol by the import receptor, Pex19 [16, 14]. The Pex19-cargo complex docks at Pex3 on the peroxisome membrane, followed by PMP integration into the membrane and Pex19 recycling to the cytosol [16]. Evidence suggests the PMP integration into the membrane is ATP-dependent, but that export of Pex19 is not [16].

In mammals, it has been shown that both pathways are used to transport membrane proteins to existing peroxisomes, with some proteins Class I and others Class II [65]. However, there is evidence that at least some proteins can use both pathways [65], with suggestions that the route through the ER is the primary path [65, 58]. In yeast, PMPs also use both pathways [66, 67, 20], but the ER does not provide PMPs to existing peroxisomes, but rather for the formation of new peroxisomes [68, 69]. In yeast, this leaves Class II targeting to maintain existing peroxisomes [65].

A block on PMP assembly or import into peroxisome membranes soon leaves no peroxisomes, as PMPs are necessary for matrix protein import. Such a block could arise through a defect in Pex3, Pex16, or Pex19 [58, 12]. If only matrix protein import is blocked, PMPs are present on membranes but the matrix is empty, these are known as ghosts or remnants [58].

2.1.4 Peroxisome Division and *De Novo* Formation

Here we provide some detail on the processes that increase peroxisome numbers, although we do not model or investigate these processes in this thesis. This section provides context, as we focus on processes related to peroxisome degradation, and

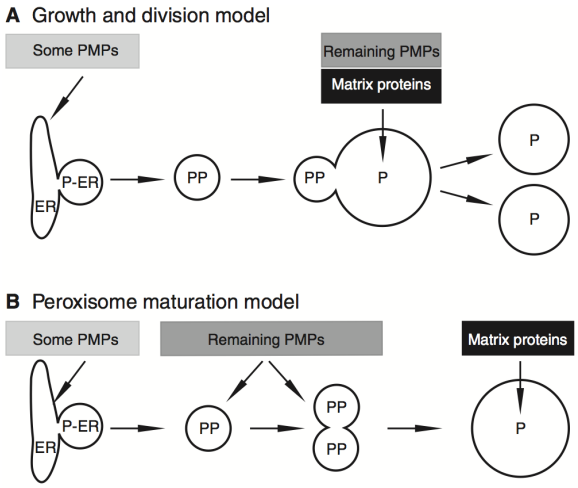

Figure 2.4: **Division Modes** Diagram of peroxisome proliferation models from Ref. [12]. With growth and division (A), peroxisomes are sent membrane and peroxisome membrane proteins (PMPs) from the ER as peroxisomal proteins collect in regions on the ER, noted in the diagram as P-ER, and bud off as pre-peroxisomal vesicles PP to traffic to peroxisomes. Peroxisomes also obtain more membrane proteins and matrix proteins from the cytosol. The peroxisome increases in size and divides into two peroxisomes. With *de novo* peroxisome formation from the ER (B), pre-peroxisomal vesicles bud from the ER and fuse to form a pre-peroxisome which has membrane and membrane proteins, which can then mature by importing matrix proteins.

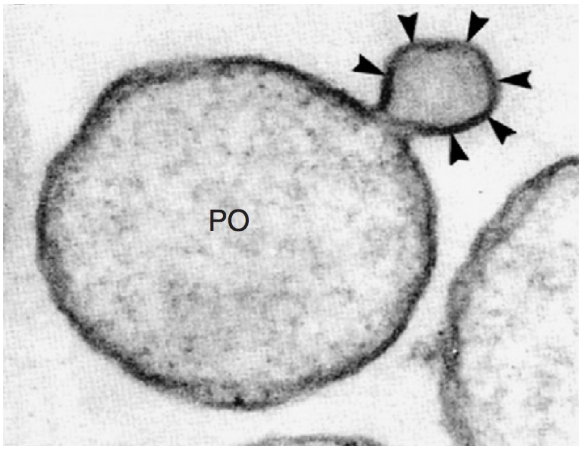

Figure 2.5: **Asymmetric Peroxisome Division** EM image of an asymmetrically dividing peroxisome, from Ref. [70]. PO indicates the parent peroxisome, and the arrowheads a budding peroxisome.

so processes that increase peroxisome numbers are the other main component to understanding peroxisome number regulation. Fission and *de novo* formation are both quite controversial and lack comprehensive understanding, and modelling either or both would be a significant challenge.

Peroxisomes can form by fission of existing peroxisomes [36, 70], or by *de novo* formation from the ER [12, 71, 72]. These two processes are shown schematically in Figure 2.4.

Peroxisome division is thought to be an asymmetric process [73], with a smaller peroxisome budding off the initial large peroxisome, as shown in the image of Figure 2.5. The Pex11 family of proteins starts the division process, by growing and shaping the membrane, as well as recruiting other necessary proteins [73]. The first stage is membrane elongation, followed by membrane constriction, with Pex11 concentrated at the constriction site [73, 74]. Pex11 is not the only peroxisomal protein that is distributed asymmetrically during peroxisome division. Matrix proteins are thought to be restricted to the old peroxisome, with the new peroxisome only containing newly imported matrix proteins [73, 20]. Membrane proteins are also asymmetrically distributed between the old peroxisome and the budding new peroxisome, with certain proteins concentrated on the budding new peroxisome and others distributed uniformly [73, 75, 76]. Final fission requires dynamin-like proteins and energy input [73]. A newly fissioned peroxisome will mature by importing both matrix and membrane proteins [73].

At least in wild-type cells, *de novo* peroxisome formation from the ER begins with the localization of some peroxisome membrane proteins to the ER, concentrated in specific subdomains which bud off [16, 12]. Many maturation models have been proposed for *de novo* formation of peroxisomes from the ER [71, 77], but all involve the budding of vesicles containing PMPs from the ER [78, 79]. It is thought that different classes of preperoxisomal vesicles bud from the ER, with a sorting mechanism localizing different proteins to different classes of vesicles [11, 68]. The fusion of the preperoxisomal vesicles is coordinated so that no vesicle has all the protein components for matrix protein import until all the fusion processes are complete, possibly to ensure the correct ratio of protein components [11, 68]. Import of matrix proteins after the fusion process will allow the fused vesicles to mature into peroxisomes. The

preperoxisomal vesicles are also unable to fuse with mature peroxisomes [11].

Formation of peroxisomes *de novo* was discovered in mutant cells which initially completely lacked peroxisomes [73], but the process may also occur under normal conditions [21, 66], and specifically have been both observed to occur in human fibroblasts [64]. The balance of contributions from the two pathways are subject to speculation, and the proportions are thought to vary among organisms and with cellular conditions [73, 11]. In both pathways, membrane from the ER is thought to be the source of membrane material [65].

2.1.5 Peroxisome Degradation

Peroxisomes in mammalian cells appear to have a half life of approximately 1.5 - 2 days in basal conditions [13, 20]. Peroxisome degradation can be induced by a change of cellular conditions or environment. In mammalian cells, peroxisome numbers significantly increase following the introduction of peroxisome proliferator-activated receptor α (PPARα) — removal of PPARα leads to peroxisome degradation in days [80]. Peroxisome degradation can be induced in yeast by switching *Pichia pastoris* from methanol to ethanol media, or by adding glucose or ethanol to *Hansenula polymorpha* in methanol media, with peroxisome numbers decreasing in hours, following a reversal of the change in growth medium [81, 82].

There are three distinct modes of peroxisome degradation: macroautophagy, microautophagy, and 15-lipoxygenase-mediated autolysis [20, 83, 80]. During macroautophagy, the peroxisome is surrounded by an autophagosome which fuses with the lysosome, leading to degradation within the lysosome [20, 83, 80]. During microautophagy, the peroxisome is directly engulfed by the lysosome, leading to degradation within the lysosome [20, 83, 80]. During 15-lipoxygenase-mediated autolysis, 15-lipoxygenase introduced to the peroxisome membrane lyses the organelle, leading to degradation by proteases and/or the proteasome [80, 20]. In mammals, peroxisomes are primarily degraded by macroautophagy [84], where in yeast there can be significant degradation through both macroautophagy and microautophagy [83, 85, 86, 87].

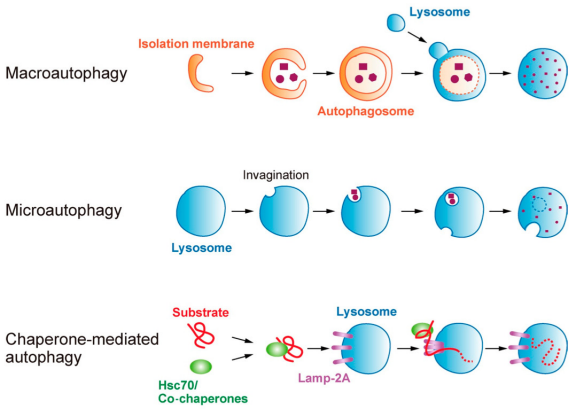

Figure 2.6: **Autophagy Modes.** Three distinct modes of autophagy: macroautophagy, microautophagy, and chaperone-mediated autophagy, shown in cartoons from Ref. [88]. Macroautophagy is the dominant mode of pexophagy. In macroautophagy, an autophagosome forms around autophagy substrates, and then fuses with a lysosome where the autophagy substrates are degraded by enzymes. In microautophagy, the autophagy substrates are directly engulfed by the lysosome, and the resulting vesicle is pinched off to release the substrates for degradation. In chaperone-mediated autophagy, substrate proteins are delivered to the lysosome, and translocated across the membrane for degradation.

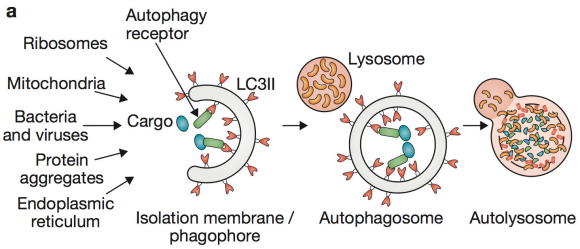

Figure 2.7: **Autophagosome Formation in Macroautophagy** An autophagosome formation cartoon from Ref. [89]. Autophagy substrates, or cargo, are shown as blue ovals. Autophagy receptor proteins, green rectangles, can bind to both the autophagy substrate and LC3, red v-shapes, which are on the autophagosome membrane. The autophagosome expands to surround autophagy substrates. Once the autophagosome is closed, it may fuse with a lysosome, to become an autolysosome. The lysosome contains enzymes that will degrade the autophagy substrates that were surrounded by the autophagosome.

2.2 Autophagy

Autophagy refers to degradation of substrates from the cytosol inside lysosomes [6]. There are three types of autophagy — these are shown schematically in Figure 2.6. Macroautophagy refers to degradation where the substrate is surrounded by a double membrane structure known as an autophagosome, which fuses with the lysosome to degrade the substrate [6, 89], as shown in more detail in Figure 2.7. During microautophagy a substrate is directly engulfed by the lysosome [6, 89]. Chaperone-mediated autophagy primarily targets proteins, where substrate proteins are recognized by chaperone proteins, before translocation across the lysosome membrane [6]. The work presented in this thesis focuses on degradation of mammalian peroxisomes, which are primarily degraded by macroautophagy [84], and so in this section we will focus on macroautophagy, and refer to this process simply as autophagy.

The autophagosome is nucleated with specific proteins of the autophagy system [6, 90], followed by elongation using membrane supplied by transport of vesicles from clathrin-coated pits on the cell membrane [91]. Elongation of the membrane is driven by ubiquitin-like reactions, where one autophagy protein is activated by another protein, and passed to a third protein [90]. One of these ubiquitin-like reactions involves the protein microtubule-associated protein 1 light chain 3, often referred to as LC3 [92]. Cytosolic LC3-I is conjugated to a lipid to become LC3-II and, along with the other ubiquitin-like reaction products, is essential for autophagosome membrane elongation and closure to form a closed vesicle [92]. Autophagosomes are moved along microtubules to lysosomes, requiring dynein motors [92]. Autophagosomes fuse with the lysosome, delivering the autophagy substrates to the lysosome for degradation by enzymes [89].

Autophagy was initially thought a non-selective process that consumed regions of cytosol as a starvation response to obtain resources [5]. However, this view has changed, with the autophagy system shown capable of selectively degrading substrates [8].

Selective degradation of substrates by autophagy is achieved by what are known as autophagy receptor proteins [6]. These receptor proteins contain domains to interact with the autophagy substrates as well as the proteins of the autophagy system. The idea is that different receptor proteins and receptor protein combinations will

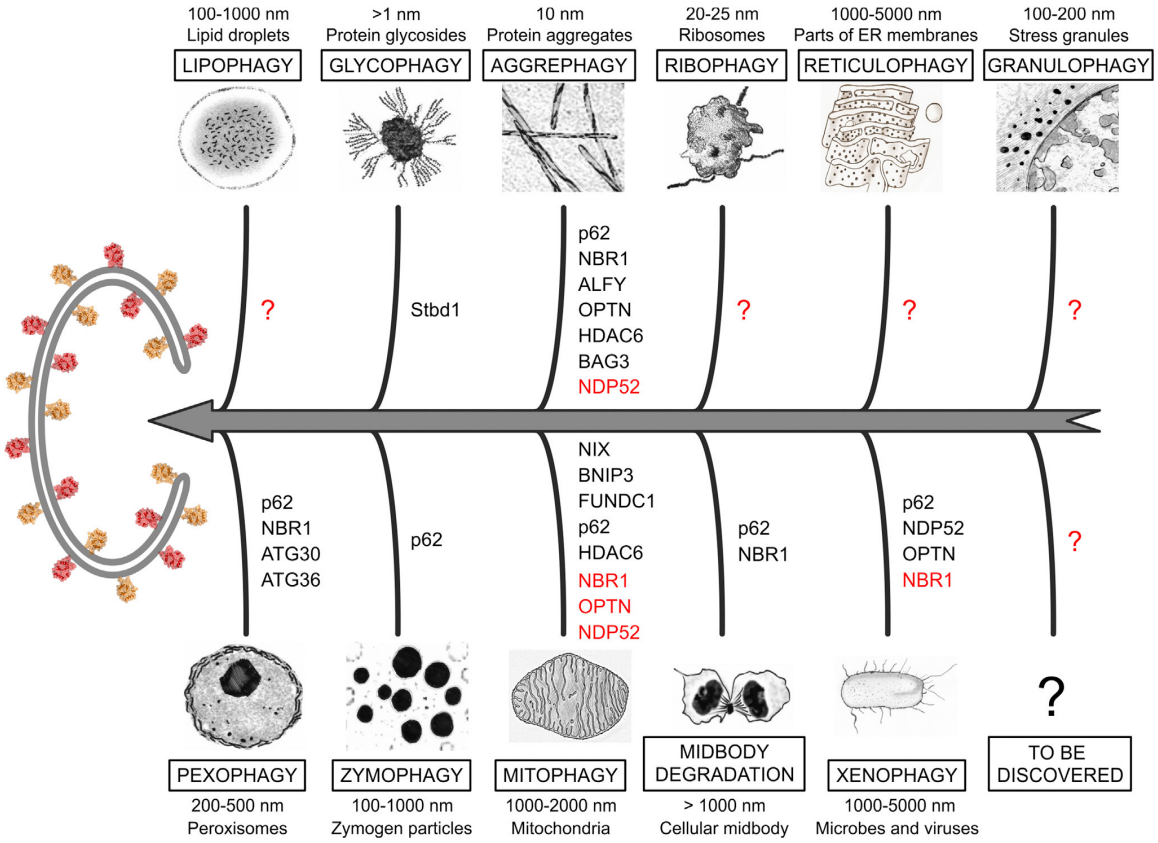

Figure 2.8: **Receptor Proteins.** Mammalian autophagy receptor proteins, from Ref. [6]. The terms aggrephagy, ribophagy, pexophagy, etc. refer to autophagy of protein aggregates, ribosomes, peroxisomes, etc. Different receptor proteins are thought to select different substrate types for degradation. Receptor proteins written in black have been established for the substrate, while those written in red are proposed. Question marks indicate substrates thought to be degraded by autophagy, but with receptor proteins as yet unidentified.

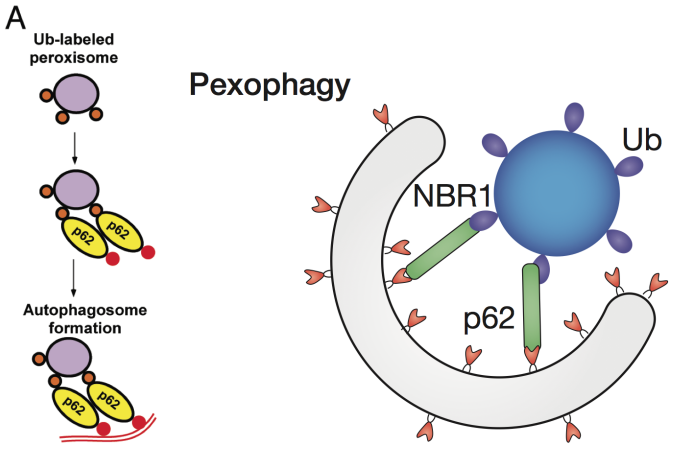

Figure 2.9: **Pexophagy** Left: a pexophagy cartoon from Ref. [93]. A peroxisome (large purple circle) is labelled with multiple ubiquitin (small red circles with black edge). p62 binds to the ubiquitin and to proteins of the autophagy system (small red circles without black edge), such as LC3. LC3 is bound to an elongating autophagosome membrane (red lines). Right: a pexophagy cartoon from Ref. [89]. A peroxisome (blue circle) is labelled with ubiquitin (Ub, blue ovals). NBR1 and p62 (green rods) can bind to both ubiquitin and proteins on the autophagosome, such as LC3 (red v-shapes). The autophagosome grows to engulf the peroxisome.

select distinct substrate types, for example selecting peroxisomes rather than other available substrates such as mitochondria [6, 89]. The mammalian receptor proteins for peroxisomes are p62 and NBR1, and the receptor proteins for other substrates are shown in Figure 2.8. Ubiquitin labelling of peroxisomes in mammals can also induce autophagy [18]. Macroautophagy of peroxisomes is shown in the cartoons of Figure 2.9. ATG30 and ATG36 are pexophagy receptors for different yeast species, and unlike NBR1, are specific to peroxisomes [94]. Macroautophagy does not appear to be as well-understood in yeast, although this may be due to differences between species and the variety of conditions in which yeast can survive — frustrating the effort to assemble a cohesive understanding.

p62 and NBR1 are also thought to be involved in degradation of midbody remnants [95, 96] — midbodies are singular organelles formed between daughter cells during the final stages of cell division [95, 96]. Midbody degradation may play a role in cell fate [95, 96], which would suggest very different degradation regulation than peroxisomes, despite using the same autophagy receptor proteins. Certainly with only one midbody remnant, the size selection mechanisms discussed in this thesis do not appear to apply.

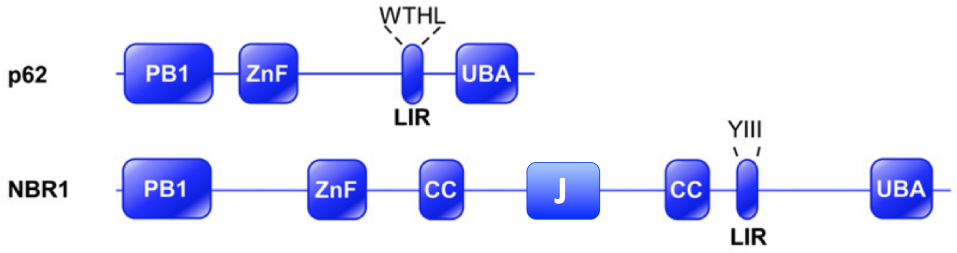

Figure 2.10: **Domains of NBR1 and p62** Diagram of the domains of the autophagy receptor proteins p62 and NBR1 from Ref. [97]. p62 contains the PB1 domain for homo-oligomerization and hetero-oligomerization with other proteins containing PB1, LIR for interaction with the LC3 protein of the autophagy system, and the UBA domain for binding to ubiquitin. NBR1 contains the PB1 domain, LIR, and UBA domain, in common with p62, but also contains two CC domains for self-interaction, and a 'J' domain for membrane association.

p62 was the first mammalian autophagy receptor protein discovered [98, 99, 6], and plays a role in selecting many substrates for degradation by autophagy [6]. It has several regions or domains that are essential for its role in autophagy. The LC3-interacting region (LIR) interacts with the LC3 protein of the autophagy system to recruit the autophagosome membrane around the substrate [100, 101]. The UBA domain binds to ubiquitin, and allows p62 to bind to ubiquitinated substrates [100, 102, 8]. The Phox and Bem1p (PB1) domain has two faces, each of which can bind to the opposite face, allowing p62 to stack or oligomerize into chains [103].

NBR1 is another autophagy receptor protein, which also plays a role in selecting multiple substrate types for degradation [6]. Importantly, NBR1 is both necessary and sufficient for peroxisome autophagy [19]. In addition to a LIR, UBA domain, and PB1 domain, NBR1 contains a distinctive 'J' domain for membrane anchoring, and a coiled-coil (CC) domain for self-interaction — all of these domains are essential for pexophagy [19]. NBR1 is made monomeric by deleting its coiled-coil domain, as it forms oligomers through this domain, which has has been mapped to be responsible for NBR1 self-interaction [104]. In addition, deleting the coiled-coil domain leads to less efficient peroxisome clustering and targeting of peroxisomes to lysosomes, with no significant difference between the NBR1 with deleted coiled-coil domains and a control, suggesting that oligomerization of NBR1 is required for NBR1 to target peroxisomes to autophagosomes [19].

Receptor proteins have been observed in non-overlapping domains on the surface

of bacteria targeted for autophagy [9, 10, 105], and there have been observations of puncta with one autophagy receptor protein not containing another autophagy receptor protein, and vice versa [9]. It has been speculated that these domains are due to affinity of different receptor proteins for different length ubiquitin chains [10] or for different surface domains of the bacteria, but the mechanism of segregation remains unknown [9]. However, overall there is no concrete evidence of NBR1 clusters on membranes, and so our work later in this thesis is under the hypothesis of NBR1 clustering.

Ubiquitin labelling is a signal for degradation by the proteasome, a degradation system distinct from autophagy which primarily degrades individual proteins to regulate cellular processes, and can degrade misfolded or damaged proteins [8]. The proteasome recognizes polyubiquitinated substrates [106]. However, recently ubiquitination has also been shown to be a signal for degradation by autophagy [8]. This is in line with the emerging understanding of autophagy receptor proteins, which are able to bind ubiquitin, (both p62 and NBR1 have UBA domains to bind ubiquitin [104, 107]). Autophagy receptor proteins do not appear to systematically prefer monoubiquitinated or polyubiquitinated substrates, for example with p62 having higher affinity for polyubiquitin chains [104], and NBR1 having a higher overall affinity for ubiquitin than p62 but lacking a preference for single ubiquitin vs. ubiquitin chains [107]. Ubiquitin has very explicitly been demonstrated to induce autophagy of peroxisomes [18].

2.3 Coarsening

A two-phase system taken from a disordered phase into an ordered phase will not phase separate instantaneously, but rather the length scale of the separated phases will grow with time, approaching the new equilibrium [108]. This is illustrated for a two-dimensional system in Figure 2.11. Domain growth is thought to scale — the domain patterns at later times are statistically similar to earlier times [108]. The combination of larger domains with the same statistical shape led this phenomenon to be known as coarsening. In systems where both phases percolate, mass flows from the weak links of the random network to the strong ones, coarsening the network [109], as material is transported from interfaces of high curvature to those of lower

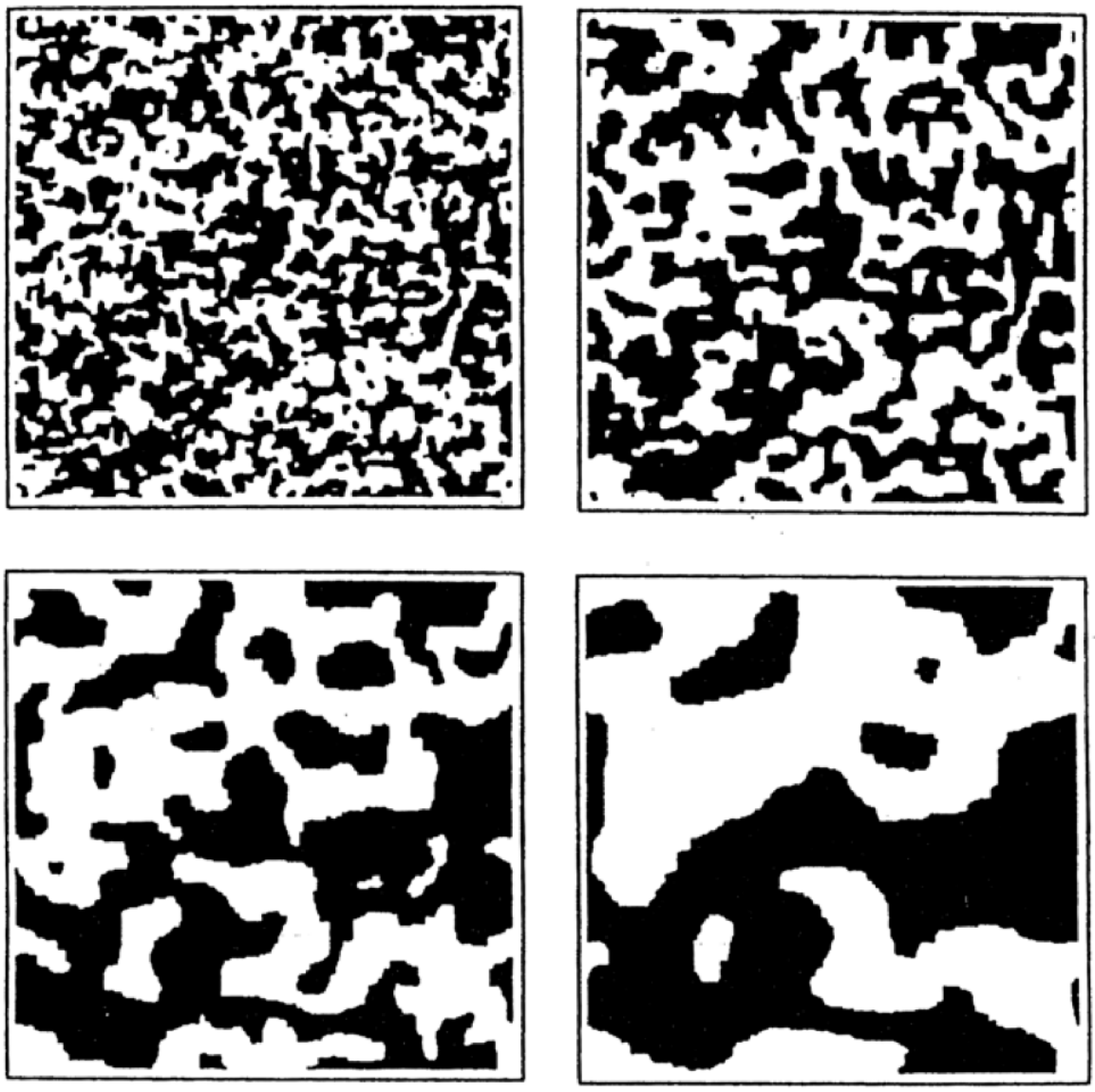

Figure 2.11: **Coarsening** Monte Carlo simulation of two-dimensional domain growth with the Ising model, from Ref. [108]. Time (in arbitrary units) starts at 5 top left, increasing to 15 top right, 60 bottom left, and 200 bottom right. The typical domain size increases as time increases.

curvature [108].

For systems with a conserved order parameter, and a double well potential for the order parameter, the change in order parameter $\phi(\vec{r}, t)$ is described by the Cahn-Hilliard equation [108],

$$\frac{\partial \phi}{\partial t} = -\nabla^2 \left[\nabla^2 \phi - V'(\phi) \right]. \tag{2.1}$$

At late times, and with well-defined interfaces, the ∇^4 term is negligible, and the Cahn-Hilliard equation reduces to the diffusion equation [108]. The diffusion field relaxes much faster than the interfaces can move and so the diffusion field is always in equilibrium with the interfaces [108]. A further simplification is to assume that in the system one phase is a small minority, and that most of the system is taken up by the majority phase. The majority phase is neglected, and the minority phase comprises a dilute system. For such a system the dilute particles can initially be considered to nucleate droplets [109]. Neighbouring droplets can grow by coalescence, and this mechanism may be greatly enhanced for mobile droplets, with the cluster diffusion constant in fluid systems only decreasing with the inverse of the cluster radius [109].

In the late stages of phase separation, supersaturation is small (precluding further nucleation) and cluster mobility is low, and so coarsening occurs by competition between clusters for material, with material diffusing between clusters [109] — a process known as Ostwald ripening [110]. The classic Ostwald ripening theory for a dilute phase is attributed to Lifshitz and Slyozov [111], and Wagner [112] (LSW). LSW treat an ensemble of spherical clusters fixed in space, and assume that all particles interact with a mean-field concentration at infinite radial distance [113]. For continuous cluster sizes (i.e. clusters become smaller or larger clusters, but do not suddenly appear or disappear at non-zero size, which assumes zero nucleation and coalescence) and the Gibbs-Thomson boundary condition [114], LSW coarsening makes two important predictions. The first is that the average cluster radius would follow a power law, $\langle R(t) \rangle \sim t^{1/3}$, with $\langle R \rangle$ the average radius and t time. The power law of this exponent, $1/3$, implies that the clusters will grow slower at later times, and in the thermodynamic limit equilibrium is never achieved [108]. The second prediction is that the late time particle radius distribution is self-similar and dynamically scales [113]. The cluster size distribution has the same shape at all late times, allowing a wide variety of Ostwald ripening processes to be described [113].

The Gibbs-Thomson boundary condition is key to the LSW results for Ostwald ripening. One expression of the Gibbs-Thomson condition is the chemical potential $\mu = -\sigma K/2$, where σ is surface tension and K is curvature [108], so that larger clusters have a greater chemical potential. The Gibbs-Thomson condition requires an elevated vapour pressure for a curved cluster interface to be in equilibrium with the vapour. The Gibbs-Thomson formula for the equilibrium vapour pressure p at the edge of a cluster of radius R is [114]

$$p(R) = p_\infty \exp\left(\frac{\nu}{R}\right), \tag{2.2}$$

with p_∞ the equilibrium vapour pressure for a flat interface, and ν the capillary length, which describes the decay of the vapour pressure with increasing radius. However, the cluster edge is often taken to be sharp, implying a small capillary length $\nu \ll R$, and so the Gibbs-Thomson boundary condition is often written [110]

$$p(R) = p_\infty \left(1 + \frac{\nu}{R}\right). \tag{2.3}$$

Equation 2.2 can be derived from free energy considerations, assuming that the cluster density is much larger than the vapour density [114]. The Gibbs-Thomson equation is most valid for low vapour densities, which require large clusters for stability [114]. A Monte-Carlo investigation suggests that the origin of the Gibbs-Thomson effect is that for smaller clusters there is greater curvature at the interface, leading to a lower coordination number and a lower energy barrier to detachment [114].

Investigation of two-dimensional coarsening systems has been hindered by the logarithmic divergence in the steady-state solution to the two-dimensional diffusion equation [110]. Limited to vanishing capillary length, Rogers and Desai found the critical cluster radius $R_c \sim (t/\ln t)^{1/3}$ [115]. Yao *et al.* similarly found $R_c \sim (t/\ln \phi)^{1/3}$, with ϕ the volume fraction [110]. These different results are due to taking volume fraction $\phi \to 0$ before or after taking $t \to \infty$, respectively [108], and highlight the difficulties encountered investigating two-dimensional Ostwald ripening.

2.4 Diffusion-limited Rates

Diffusion in liquid typically involves a molecule whose motion has a very short mean free path 'trembling' about its position. Much of its motion is due to longer (but still

short) motions when the solvent randomly cooperates. After a time τ, a diffusing molecule in three dimensions has 'searched' an available volume of volume $8\pi DR\tau$, where D is the diffusivity and R is the molecule radius. The nature of a diffusional path means that a molecule is likely to come close to its starting point a number of times prior to significant separation from its original location. This means that the mean time that molecules remain nearby one another is $\simeq R^2/D$, and can be significantly longer than a brief collision [116].

Diffusion-limited processes are limited by the amount of time it takes for reactants to be close enough together so that they may carry through a reaction. Diffusion-limited rates provide an upper limit to the rate of a reaction, but due to the properties of biological macromolecules, apparent association rates can approach this limit. The reaction process may be slowed by chemical processes — if these are rate limiting, a reaction is considered reaction-limited [116].

Diffusion-limited reactions may be distinguished by inhomogeneous reactant concentrations, as the reaction region depletes of unreacted molecules. A viscosity dependence of the reaction rate can also imply a diffusion-limited reaction, due to the inverse relationship between diffusivity and viscosity. Weak temperature dependence may indicate diffusion control [116].

In general, macromolecules are not reactive over their entire surfaces, instead only an active site may be involved in the reaction. Fully describing diffusion-limited association may require consideration of molecule orientation as well as position. The time spent by diffusive molecules nearby one another may help mitigate orientational effects, as molecules are given time to reorient. Additionally, inter-molecule interactions may also mitigate orientational issues once the molecules are in close proximity [116].

In Ref. [117], Berg and Purcell solve for diffusive flux for a variety of diffusion-limited problems. A simple example is the diffusion-limited flux to an absorbing sphere of radius R. For a system that is radially symmetric, the diffusion equation is

$$\frac{\partial c}{\partial t} = D\nabla^2 c = \frac{D}{r^2}\frac{\partial}{\partial r}\left(r^2\frac{\partial c}{\partial r}\right), \tag{2.4}$$

where c is the concentration, D is the diffusivity, and r is the radial distance from the centre of the sphere. The system is assumed to be in steady state, so $\partial c/\partial t = 0$. The equation then generally solves to $c(r) = Ar^{-1} + B$. The concentration far from

the sphere is assumed to be some asymptotic concentration, $c(r \to \infty) = c_\infty$, and the concentration at the surface of the absorbing sphere is zero, $c(r = R) = 0$. These lead to $c(r) = c_\infty(1 - R/r)$. The radial flux towards the sphere is then $I = D\partial c/\partial r = Dc_\infty R/r^2$. The total flux through a spherical surface of radius r is then $J = 4\pi r^2 J = 4\pi D c_\infty R$ — this quantity is independent of r, so that it is also the flux to the surface of the absorbing sphere. Other geometries have also been explored, e.g. in Ref. [116].

Berg and Purcell [117] also make a useful analogy between capacitance and diffusive flux, expressing it as

$$J = 4\pi C D c_\infty \tag{2.5}$$

in CGS units, where C is the capacitance (in SI the relationship is $J = CDc_\infty/\epsilon_0$, with ϵ_0 the permittivity of free space). The capacitance for concentric spherical conductors, inner radius a and outer radius b, is

$$C = 4\pi\epsilon_0 \frac{ab}{b-a}. \tag{2.6}$$

If $b \to \infty$, leaving only the inner spherical conductor, the capacitance becomes $C = 4\pi\epsilon_0 a$. Using the SI capacitance-diffusive rate relationship, the diffusive flux to a spherical absorbing surface is

$$J = (4\pi\epsilon_0 a) D c_\infty/\epsilon_0 = 4\pi D c_\infty a, \tag{2.7}$$

recovering the result derived from the diffusion equation above.

Dimensionality is important for determining the length of a diffusion-limited search. For a domain of radius L, the search time contains an L^2/D factor in one, two, and three dimensions. In three dimensions the search time is $\tau_3 = (L^2/(3D))(L/b)$ for target of radius b, so that target size can significantly affect the search time. However, the search times are $\tau_2 = (L^2/(2D))\log(L/b)$ in two dimensions and $\tau_1 = L^2/(3D)$ in one dimension, with target size becoming less important as dimensionality decreases. The diffusional search for a small target is much more efficient in one or two dimensions than three dimensions [116].

A search could be divided into a three-dimensional search for a structure, followed by a two-dimensional (e.g. membrane) or one-dimensional (e.g. linear polymer) search [116]. The efficiency of such a multi-dimensional search will depend on the

details of the searching molecule, its target structure, and their interactions. One process that has been intensely studied is the diffusive search for a binding site on DNA [118, 119, 120]. Proteins can appear to find their binding sites faster than diffusion-limited rates [118, 119]. The diffusive search is thought to be a combination of three-dimensional motion to bind a DNA strand, and one-dimensional sliding along a strand to search for the specific binding site [118, 119, 120].

2.5 Gillespie Algorithm

Continuous and deterministic rate equations are not always appropriate to simulate the trajectory of reactions in a system, as they rely on bulk reactions and a very large number of molecules. The Gillespie algorithm [121] can perform discrete and stochastic simulations of systems with few molecules, as each reaction is explicitly simulated. This is important as stochastic systems can produce important non-deterministic effects [122].

The Gillespie algorithm treats different molecular species or reaction species as distinct groups, rather than individually. Given a set of reactions with deterministic rates, the simulation identifies which reaction occurs next and at what time the reaction occurs, and they are identified probabilistically. As the number of reactants changes, the probabilities of the reactions changes as well.

We have a system initially in state $\psi(t)$ at time t. The system is such that N reactions can occur, each with rate R_i, with $i = 1, 2..., N$. If the sum of all reaction rates is $\sum_{i=1}^{N} = R_{tot}$, and the time of the next reaction is Poisson-distributed because the reactions are random, the the next reaction will occur after a time

$$\tau = (1/R_{tot}) \log(1/r_1), \tag{2.8}$$

where $r_1 \in [0, 1]$ is a random number. The j'th reaction will occur, with the value of j determined by

$$\sum_{i=1}^{j-1} R_i < r_2 R_0 \leq \sum_{i=1}^{j} R_i, \tag{2.9}$$

where $r_2 \in [0, 1]$ is a random number distinct from the random number r_1.

Using random numbers to determine the time of the next reaction and the identity of the next reaction, we can stochastically simulate a system.

First, the system is initialized. The simulation time is set to zero, $t = 0$. The state of the simulated system is initialized, $\psi(0) = \psi_0$. From the system state, the rates of the reactions, R_i, are calculated, and the total rate, R_0, calculated.

The system is then iterated. Random numbers r_1 and r_2 are generated. The random numbers determine the time until the next reaction, τ, and the identity of the next reaction, j. The time is increased from t to $t+\tau$, and the state of the system is adjusted to reflect reaction j, so that $\psi(t) \to \psi(t+\tau)$. The reaction rates R_i are recalculated, as well as the total rate R_0. The system is iterated until a maximum or time or some other criterion is reached.

2.6 Previous Work

Chapter 4 investigates a quantitative model of the peroxisome matrix protein import system, and tracks ubiquitin levels to understand how they may play a role in regulating peroxisome numbers by signalling for autophagy. Mukherji and O'Shea [123] quantitatively model processes increasing and decreasing organelle number as stochastic processes, and focus on peroxisomes. They find that distinct noise measurements in different organisms indicate whether new peroxisomes are primarily created by fission of existing peroxisomes or *de novo* formation from the ER. Borlin *et al.* [124] quantitatively model the activities of autophagy vesicles, such as creation and degradation, and fit to observations to determine parameters of the model. These parameters provide estimates of several quantities that have not been measured, and insight into autophagy vesicle dynamics. Nayak *et al.* [125] modelled the bacterial Tat translocon, allowing translocon elements to associate and dissociate with the translocon, and explored quality control of non-translocatable substrates. Zilman *et al.* [126] modelled a kinetic mechanism for the selectivity of 'always open' nanochannels.

Chapters 5 and 6 explore a quantitative model of the dynamics and formation of autophagy receptor protein clusters on peroxisomes. Biological coarsening models have previously been quantitatively investigated. Ryan and Rutenberg [127] used a lattice model and two-stage nucleation to predict lysis timing. Derr and Rutenberg [128] showed how proteolysis could stabilize cluster size distributions of clustering proteins. Wang *et al.* [23] demonstrated that protein clusters could self-organize into a periodic pattern [23]. Howell *et al.* [129] showed that multiple polarization clusters

on the yeast cell membrane could compete and resolve into a single polarity cluster. Turner *et al.* [130] found that recycling membrane domains allowed for steady-state domain sizes of intermediate size.

Two dimensional coarsening has been studied by Rogers and Desai [115] and Yao *et al.* [110], both of which aimed to find scaled cluster size distributions and average cluster growth dynamics, among other standard coarsening measurements. Krishnamachari *et al.* [114] investigated a single two-dimensional cluster in a finite-size system.

Chapter 3

Introduction to Chapters 4, 5, and 6

In the paper of chapter 4 we will consider the accumulation of ubiquitin on peroxisomes, and how it may provide a signal for autophagy. This paper has been published in 2014 in PLoS Computational Biology, volume 10, page e1003426, authored by myself, Peter Kim, and Andrew Rutenberg.

In the paper of chapter 5 we will consider the dynamics of clusters on spherical drops, inspired by the observation of domains of receptor proteins on autophagy substrates and the roughly spherical peroxisome geometry. This paper has been published in 2015 in Soft Matter, volume 11, pages 3786-3793, authored by myself and Andrew Rutenberg.

In the paper of chapter 6 we will consider a system of peroxisomes with NBR1 cluster formation and dynamics, and p62 chain formation on NBR1 and ubiquitin. This paper is motivated by the observation of autophagy receptor protein domains, and the participation of both NBR1 and p62 in peroxisome degradation by autophagy. This paper is currently in preparation.

Overall we will look at how peroxisome degradation by autophagy is organized in time and to select a subset of peroxisomes. As part of the peroxisome matrix protein import system, it is possible for ubiquitin to organize peroxisome degradation, as matrix protein import interacts with the rest of the cell. Responding to other cellular events allows organization of peroxisome degradation in time. NBR1 can allow selection of a subset of peroxisomes for degradation, as the behaviour of our hypothesized NBR1 clusters depends on peroxisome size. p62 interaction with NBR1 clustering dynamics modifies the selection of peroxisomes for degradation.

3.1 Chapter 4

First, we briefly review the two roles ubiquitin is known to play on peroxisome membranes.

Ubiquitin plays an important role in the degradation of peroxisomes through autophagy, known as pexophagy. This has been explicitly shown, with artificial ubiquitin labelling of peroxisomes inducing a decrease peroxisome numbers [18]. It is also consistent with evidence of crosstalk between the ubiquitin-proteasome system and the autophagy system [8]. NBR1 and p62 have been shown to be receptor proteins for peroxisomes, which interface between the peroxisome and the autophagy system — both NBR1 and p62 have UBA domains to bind ubiquitin. In chapter 4 we consider only the effects of ubiquitin dynamics, and leave the roles of NBR1 and p62 to later chapters.

In section 2.1.2 of chapter 2, the peroxisome matrix protein import process was described. A key step in this process is the ubiquitination of the shuttle protein Pex5, which signals for the shuttle protein to exported from the peroxisome membrane to the cytosol. The level of ubiquitinated Pex5 is expected to depend on the production of cargo proteins to be imported to the peroxisome matrix, as this would control the supply of Pex5 provided for ubiquitination and the number of targets for ubiquitinating enzymes. The number of proteins in the peroxisome matrix protein system is also important, as it would determine the number of Pex5 that can bind to the import system, and how quickly they could be ubiquitinated and exported. The details of protein translocation across the peroxisome membrane, an open question, could also be important as they may affect under what conditions Pex5 could be ubiquitinated or exported.

In chapter 4 we ask whether the ubiquitin levels associated with matrix protein import can provide a plausible signal for autophagy.

This question directly addresses the self-regulation and cooperative coupling hypotheses presented in chapter 1. We are investigating whether ubiquitin associated with the peroxisome matrix protein import system can naturally provide a plausible signal for peroxisome degradation. The cooperative coupling is important to this investigation because the modelled ubiquitin levels in the import system depend on the coupling between cargo protein translocation across the peroxisome membrane and Pex5 export from the peroxisome membrane. To my knowledge, there are no other routine processes on the peroxisome membrane that involve ubiquitin. Therefore, the alternative to self-regulation of the autophagy signalling through ubiquitin is a signal

external to the peroxisome membrane that causes an increase in ubiquitin which is not typically associated with the peroxisome.

3.2 Chapter 5

Autophagy is a cellular system for degradation of primarily large substrates. Until recently, autophagy was thought to be non-selective, however it has recently been shown capable of selectivity. The selection of different types of substrates in the cell, e.g. peroxisomes vs. mitochondria, is thought to be mediated by autophagy receptor proteins or their combinations, although understanding of how this occurs is very limited. Receptor proteins were recently observed in segregated domains on an autophagy substrate, an invading bacterium [9, 10]. There has been some speculation on how the receptor proteins separate into domains, but there appears to have been no comment on the implications of domains or clusters for autophagy selectivity.

The standard framework for understanding the behaviour of clusters is Lifshitz-Slyozov-Wagner (LSW) coarsening [111, 112, 108]. Clustering dynamics are well understood in greater than two dimensions, with a consistent power law for the radius of the average cluster with exponent 1/3, and dynamic scaling of cluster size distributions. In two dimensions, the standard diffusive approach gives a divergent result, but there are multiple investigations [115, 110, 108] of the two-dimensional system which determine the average cluster size in time and the cluster size scaling function. Coarsening of proteins or other molecules on biological membranes has been theoretically addressed on surfaces which do not explicitly account for the finite size or curvature of an organelle surface [127, 128]. In cases where the finite surface size [130] or curvature [129] are accounted for, only systems comprised of a single surface are considered.

In chapter 5 we ask two distinct questions. Our first question is specific to coarsening. Do clusters on the surface of spheres coarsen in an LSW manner, and if so what changes are introduced by clustering on many, finite surfaces compared to a bulk system? The second emphasizes application of the resulting cluster dynamics to understanding autophagy selectivity. Do clusters on spheres behave in a way that impacts the selection of autophagy substrates? How are clusters on spheres different from the binding of molecules to spheres without clustering?

Chapter 5 investigates the dynamics of these coarsening clusters of receptor proteins, which assumes our hypothesis from chapter 1 that receptor proteins have the necessary characteristics for coarsening behaviour. We also address our hypothesis of self-organization. We simply posit the existence of clustering proteins and assume they have nucleated widely, and then follow their dynamics. Organization of peroxisome degradation could then follow, without other signals to label some peroxisomes for degradation and not others.

Chapter 4 had a very specific and well-known biological open question — how is peroxisome matrix protein translocation energetically driven during the import cycle. The context of this question, the peroxisome matrix protein import cycle, is fairly well understood. The paper of the following chapter, chapter 5, also speaks to an open question, but one that is more nebulous. Autophagy is a rapidly developing field and understanding of autophagy substrate selection is limited. Work in the autophagy field has focused on selection of different substrate types. We examine a different issue, the selection of individual substrates of a certain type, in our case selecting some peroxisomes for degradation by autophagy, and leaving others. To go along with a lack of attention, there is a corresponding relative lack of evidence and literature for context for this specific problem. Despite the lack of attention, cells are capable of degrading a fraction of a certain type of substrate, rather than the entire substrate population, and there must be mechanisms behind this regulation. The selection mechanism we find could play a significant role in regulating the degradation of peroxisomes by autophagy.

3.3 Chapter 6

Chapter 6, similar to chapter 5, investigates how receptor protein clusters can select some peroxisomes for degradation, but not others. Interactions between combinations of receptor proteins are thought to play a role in autophagy selectivity, although the details or principles of these interactions have not been elucidated. The receptor proteins also interact with their autophagy substrates, and the characteristics of the substrate, for example the levels of surface proteins, influence selectivity.

For peroxisomes, the two autophagy receptor proteins are NBR1 and p62. NBR1

is both necessary and sufficient for pexophagy [19], but p62 can also modulate pexophagy [18, 19]. Ubiquitin labelling of peroxisome membrane proteins has also been shown to induce pexophagy [18], and in chapter 4 we argued that changing ubiquitin levels, in response to peroxisome matrix protein production, could regulate pexophagy.

In chapter 6 we ask several related questions. How could the presence of both NBR1 and p62, and interactions between the two receptor proteins, affect peroxisome degradation by autophagy? How could the ubiquitin level influence the accumulation of NBR1 and p62 on peroxisomes? In chapter 5 cluster nucleation was neglected, with a cluster present on all drops as an initial condition. Could cluster formation play a significant role in autophagy selectivity?

Chapter 6 addresses the self-regulation hypothesis of chapter 1 in much the same way as chapter 5. Self-organization of clusters to select peroxisomes for degradation is investigated further, with chapter 6 looking at a more complex system than chapter 5. To introduce non-trivial interactions between NBR1 and p62, we hypothesize that chains of p62, with an NBR1 base, will sterically inhibit these NBR1 from participating in cluster formation or growth. NBR1 cluster formation and changing ubiquitin levels are also introduced, and are part of determining how labelling peroxisomes for degradation is organized.

In chapter 6 we put forward a plausible model of how different receptor proteins could interact, be recruited by ubiquitin, and form clusters. The implications of the model are explored, and the selection mechanism and consequences of the different interactions are followed to determine their effect on pexophagy.

3.4 Overall

We first modelled ubiquitin accumulation, followed by NBR1 clustering, and then p62 interaction. This order is due to a combination of several factors. The contribution of ubiquitin accumulation to pexophagy [18] was published earlier than evidence that NBR1 is the primary pexophagy receptor protein [19]. Modelling ubiquitin accumulation as part of the peroxisome matrix protein import system allowed us to first investigate a the relatively well-understood import system and obtain a broader view of how peroxisomes work. Modelling NBR1 clustering moved us into the somewhat

speculative territory of autophagy receptor protein behaviour. Further along, looking at the interaction between NBR1 and p62 was even more speculative. Examining ubiquitin, then NBR1, and then p62 also allowed us to move along the order of protein recruitment to the peroxisome membrane — ubiquitin is recruited in the normal course of protein import, NBR1 is recruited to the membrane by ubiquitin, and p62 can bind both ubiquitin and NBR1.

The models of chapters 4, 5, and 6 are distinct, but can inform the others.

Although it is not explicitly mentioned, the ubiquitin signal of chapter 4 could play a role in chapter 5. In chapter 5 the initial condition always has clusters on all the spheres. This could be thought of as following a relatively sudden increase in the ubiquitin level on peroxisomes, which would quickly increase the NBR1 numbers on peroxisomes. On many of the peroxisomes NBR1 clusters could form — we consider the peroxisome subpopulation on which these clusters form. The cluster formation scenario is explored, along with the role of p62, in chapter 6, while chapter 5 focuses on the dynamics of existing clusters, which are found to qualitatively hold later.

Chapter 4 considers different levels of cargo protein traffic, which control the peroxisomal ubiquitin levels — each simulation run uses a single cargo protein flux. As mentioned above, chapter 5 considers a system that can be thought of as following a sudden increase in the ubiquitin level. Chapter 6 explicitly considers scenarios where the ubiquitin level goes from low to high. This change in the ubiquitin level could be due to a switching of the cargo protein traffic from a high level to a low level.

Chapter 4

PEX5 and Ubiquitin Dynamics on Mammalian Peroxisome Membranes

This chapter is a reproduction of the paper 'PEX5 and ubiquitin dynamics on mammalian peroxisome membranes', authored by Aidan I Brown, Peter K Kim, and Andrew D Rutenberg, published in PLoS Computational Biology in 2014, volume 10, page e1003426, doi 10.1371/journal.pcbi.1003426.

4.1 Introduction

Peroxisomes are single membrane organelles found in most eukaryotic cells [131]. They are involved in various anabolic and catabolic reactions including fatty acid oxidation, cholesterol biosynthesis, hydrogen peroxide metabolism, bile acid and plasmalogen synthesis [132]. Peroxisomal defects have been associated with serious genetic disorders such as Zellweger syndrome and neonatal adrenoleukodystrophy [27].

Peroxisomes are highly dynamic organelles, changing their numbers based on the specific metabolic needs of different tissues and cell types [81]. For example, in rodent livers, peroxisome numbers can rapidly increase two- to ten-fold in a matter of days by the activation of the receptor Peroxisome Proliferator-Activated Receptor-alpha (PPARα) [133]. In yeast, changing the carbon source to oleic acid from glucose induces the rapid proliferation of peroxisomes [81].

Conversely, removal of peroxisome proliferators results in degradation of peroxisomes in mammalian cells with peroxisome numbers returning to basal levels within a week [134, 84]. Similarly, changing the carbon source from oleic acid back to glucose results in the decrease of peroxisome numbers in yeast within several hours [81, 82]. Peroxisomal degradation in mammals is mostly mediated by selective autophagy, the process of targeting cytosolic components to lysosomes for degradation (reviewed in [80, 83]) — called 'pexophagy' for peroxisomes. In pexophagy, superfluous or damaged peroxisomes are recognized by autophagic receptors that target peroxisomes

either to autophagosomes or to lysosomes [135]. How peroxisomes are designated for degradation is not well understood. In mammalian peroxisomes, it has been hypothesized that sufficient ubiquitination of peroxisomal membrane proteins induces pexophagy by recruiting sufficient autophagy receptors such as NBR1 to peroxisomes [19, 18].

There are indications that any ubiquitinated membrane protein can recruit NBR1 [18], however the specific peroxisomal membrane protein(s) ubiquitinated to induce peroxisome degradation are not known. One candidate is the matrix shuttle protein PEX5, as preventing its recruitment to peroxisomes prevents NBR1 mediated pexophagy [19]. PEX5 is a cytosolic receptor that binds newly translated peroxisomal matrix proteins (cargo) through their peroxisome targeting sequence 1 (PTS1) [136]. PEX5, with cargo, is imported onto the peroxisomal membrane via its interaction with two peroxisomal membrane proteins PEX14 and PEX13 [137, 138, 139]. On the membrane PEX5 is thought to form a transient pore via an interaction with PEX14 to facilitate subsequent cargo translocation [43]. On the membrane, PEX5 is ubiquitinated by the RING complex, which is comprised of the peroxisomal ubiquitin ligases PEX2, PEX10, and PEX12. We call the RING complex, together with PEX13 and PEX14, an 'importomer'. PEX5 can be polyubiquitinated, labelling it for degradation by the proteasome as part of a quality control system [140, 141, 142], or monoubiquitinated, labelling it for removal from the peroxisome membrane and subsequent recycling [49, 39]. Ubiquitinated PEX5 is removed from the membrane by the peroxisomal AAA ATPase complex (comprised of PEX1, PEX6 and PEX26) [143]. In mammals, monoubiquitinated PEX5 is deubiquitinated in the cytosol [55], completing the cycle and leaving PEX5 free to associate with more cargo.

The temporal coordination of cargo translocation, with respect to PEX5 ubiquitination by the RING complex and PEX5 removal by AAA, is not yet clear. This raises the basic question of how energy is provided to move cargo into the peroxisome. It has been suggested that there is no direct energy coupling, since it has been reported that cargo translocation happens before ubiquitination [40]. In this case, translocation of cargo would occur upon binding of PEX5 to the importomer. Subsequent removal of PEX5 would simply allow more PEX5-cargo to bind to the importomer,

and the AAA ATPase is not necessarily involved in the energetics of cargo translocation. Conversely, an immediate or direct coupling of cargo import with PEX5 removal has been proposed in which energy for translocation would be provided by the AAA ATPase complex as it removes PEX5 from the membrane [61, 62, 63].

Using stochastic computational simulations, we have explored the implications of several models of how the PEX5 cycle couples cargo translocation with PEX5 removal by the AAA complex (see Figs. 4.1 and 4.2). The first, 'uncoupled', model corresponds to no direct or immediate coupling [40]. The second, 'directly coupled' model translocates PEX5 cargo as the same PEX5 is removed from the membrane by the AAA complex [61, 62, 63]. Our third, 'cooperatively coupled' model translocates PEX5 cargo when a different PEX5 is removed from the peroxisomal membrane. While this can be seen as a qualitative variation of directly coupled import, we show that this novel model behaves significantly differently than both uncoupled and directly coupled models of PEX5 cargo translocation.

We focus our modelling on accumulation of PEX5 and of ubiquitin on the peroxisomal membrane, as the traffic of PEX5 cargo in the cell is varied. This allows us to connect our models, of how PEX5 cargo translocation is coupled with PEX5 removal, with possible ubiquitin-regulated control of peroxisome numbers through pexophagy. Since both PEX5 levels and peroxisomal ubiquitination levels are accessible experimentally, this suggests an alternative approach to resolving how cargo translocation couples with PEX5 removal. Our modelling also shows that, regardless of what mechanism couples cargo translocation with PEX5 export, translocation coupling may have significant effects on ubiquitin levels of peroxisomes and so on regulation of pexophagy in mammalian cells. For example, both the uncoupled and directly coupled models lead to more ubiquitination with more cargo traffic. In contrast, the cooperatively coupled model leads to less ubiquitination with more cargo traffic. For cooperative coupling, this suggests a mechanism where lack of cargo results in the accumulation of ubiquitinated PEX5 on the peroxisomal membrane, thus leading to the degradation of underused peroxisomes.

Our figures are organized as follows. In the Methods section, Figs. 4.1 and 4.2 illustrate the three translocation coupling models. In the Results/Discussion section,

Figs. 4.3 and 4.4 compares the behavior of these models. We then focus on cooperative coupling. We explore the fluctuations around possible ubiquitin thresholds for pexophagy with Fig. 4.5, and examine the role of numbers of peroxisomes with Fig. 4.6. Finally we investigate the effects of PEX5 export complexes with Fig. 4.7.

4.2 Methods

4.2.1 Translocation Coupling Models

We model four processes in the PEX5 cycle, each with an associated rate: the addition of peroxisomal matrix proteins, or cargo, to the cytosol (Γ_{cargo}), binding of PEX5-cargo to an empty site of an importomer (Γ_{bind}), ubiquitination of a PEX5 at an importomer (Γ_{Ub}), and export of ubiquitinated PEX5 from the importomer (Γ_{AAA}). Binding of PEX5-cargo is illustrated in Fig. 4.1(A), association of PEX5 with the RING complex in Fig. 4.1(B), and ubiquitination of bound Pex5 in Fig. 4.1(C). RING association is assumed to be immediate relative to other modelled processes, and so has no associated rate. Fig. 4.2 illustrates the three distinct models of cargo protein translocation that we consider, discussed immediately below: uncoupled (Fig. 4.2(A) and (B)), directly coupled (Fig. 4.2(C)), and cooperatively coupled (Fig. 4.2(D)). These cargo translocation models differ in the details of how cargo translocation coordinates with AAA ATPase activity.

Uncoupled and Directly Coupled Translocation Models

Following reports that PEX5-cargo association with the peroxisomal membrane was ATP independent [144, 145], it was suggested that cargo translocation may occur without concurrent ATPase activity [146]. We call this uncoupled translocation. AAA ATPase activity removes ubiquitinated PEX5 from the peroxisomal membrane [44]. Accordingly, the report that cargo translocation occurs before ubiquitination [40] supports an uncoupled model. We illustrate our uncoupled translocation model in Figs. 4.2(A) and (B), where cargo immediately translocates upon PEX5-cargo binding to an importomer.

Alternatively, it has been suggested that there may be a direct (immediate) coupling between the translocation of cargo bound to a membrane associated PEX5,

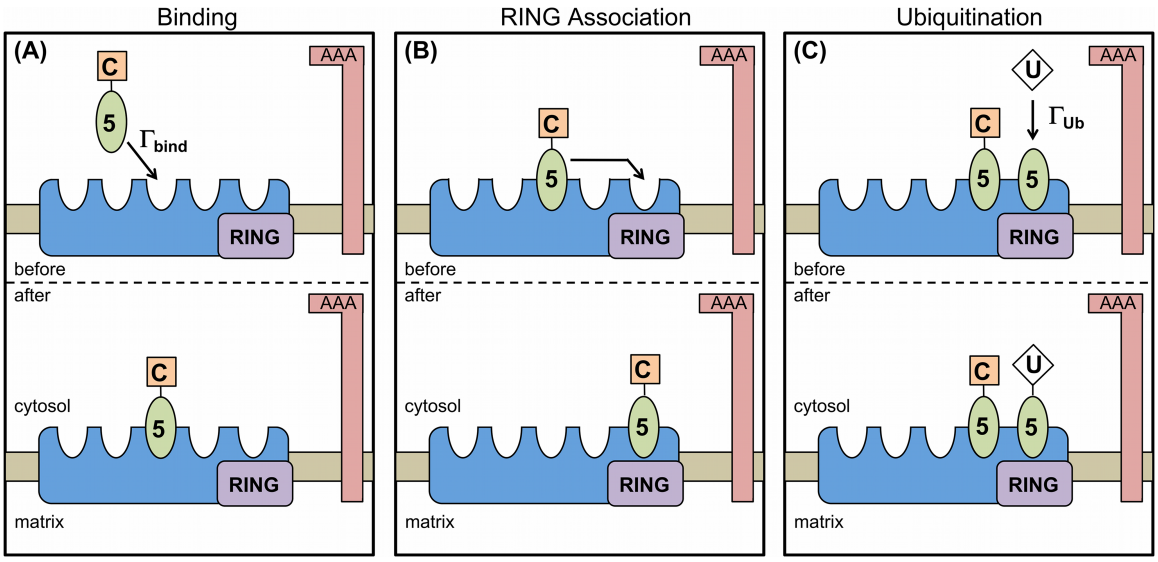

Figure 4.1: **Illustration of Model Processes and Associated Rates that are Shared Between Models** (A) PEX5 (green oval) associated with cargo (orange square) binds to available binding sites on a peroxisomal importomer (blue irregular shape) at a rate Γ_{bind}. There are w binding sites per importomer; here we illustrate $w = 5$. (B) If unoccupied, the RING complex site is immediately occupied by another PEX5 on the importomer. (C) The RING complex (purple rectangle) will ubiquitinate an associated PEX5 at rate Γ_{Ub}. We generally allow only one ubiquitinated PEX5 per importomer. For (A), (B), and (C) the AAA complex is shown, and will participate in PEX5 export as described in Fig. 4.2.

and the AAA-driven removal of the same PEX5 from the peroxisomal membrane [63, 62]. Direct coupling is supported by results indicating that ATP is needed for cargo translocation [147] and that PTS2-targeted cargo translocation is directly linked to Pex18p shuttle removal in yeast [148]. We illustrate directly coupled translocation in Fig. 4.2(C), where cargo translocation occurs when ubiquitinated PEX5 is removed from the membrane by the AAA complex. For simplicity, the PEX5 in Fig. 4.2(C) is illustrated simultaneously both cargo-loaded and ubiquitinated.

In the uncoupled model individual PEX5-cargo translocate immediately upon membrane association, while in the directly coupled model translocation only occurs after both ubiquitination and AAA activity. Nevertheless, in both models each PEX5 binds, is ubiquitinated, and is exported by AAA activity at the same rates independently of the details of the cargo status. The dynamics of PEX5 and of ubiquitin are indistinguishable in these two models; only the precise timing of cargo translocation differs between them.

Cooperatively Coupled Model of Cargo Translocation and PEX5 Export

We propose an additional possibility, in which more than one PEX5 is involved in the coupling between cargo translocation and AAA activity. This is our cooperatively coupled model of translocation, which we investigate for the simplest case of two PEX5. As illustrated in Fig. 4.2(D), this requires at least two PEX5 on an importomer — one of which has cargo, and the other of which is ubiquitinated. The import of the cargo of one PEX5 is coupled with the export of the second, ubiquitinated, PEX5. This is a variety of direct coupling between cargo translocation and AAA driven removal of PEX5 from the membrane [62, 63]. We further propose that the coupling of translocation and export is 'tight', i.e. export does not occur without coupled import. This would always leave at least one PEX5 per importomer, which is consistent with the *in vitro* observation of Oliveira *et al.* [144] of a peroxisomal PEX5 population that remains even after prolonged incubation with ATP to promote AAA activity.

4.2.2 Simulation Details

We implement the models of the PEX5 cycle computationally using the Gillespie algorithm [121], for N_P peroxisomes each of which has N_I importomers, each with

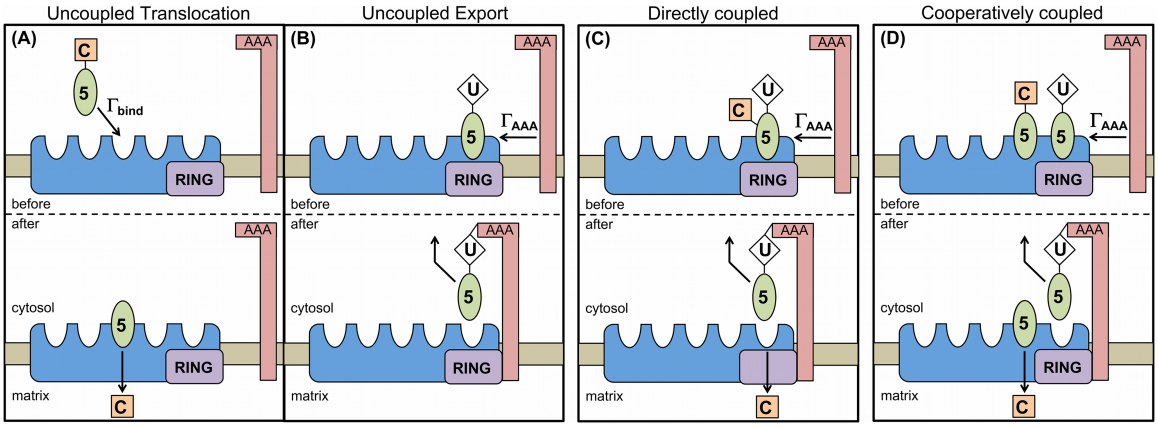

Figure 4.2: **Illustration of Translocation and Export Models and Associated Rates** (A) PEX5 (green oval) associated with cargo (orange square) binds to available binding sites on a peroxisomal importomer (blue irregular shape) at a rate Γ_{bind}. In uncoupled translocation, associated cargo is translocated spontaneously after binding to the importomer. (B) If translocation is uncoupled, then export of ubiquitinated PEX5 by the AAA complex at rate Γ_{AAA} does not have a relationship with cargo translocation. (C) In directly coupled translocation, the cargo translocation occurs as the ubiquitinated PEX5 is removed from the importomer by the AAA complex at rate Γ_{AAA}. The PEX5 is shown simultaneously both cargo-loaded and ubiquitinated — this figure is meant to be illustrative; see Methods for discussion. (D) In cooperatively coupled translocation, the removal of PEX5 by the AAA complex (Γ_{AAA}) can only occur when coupled to the cargo translocation of a distinct PEX5-cargo in the same importomer. This always leaves at least one PEX5 associated with each importomer.

w independent binding sites for PEX5-cargo, and all of which share a cytoplasmic pool of PEX5-cargo with concentration c_{PEX5}. We track the number of bound PEX5 for every importomer, together with ubiquitination status of every bound PEX5. Association rates have not been determined experimentally, so we assume diffusion-limited association rates (see next subsection). This allows us to explicitly avoid fine-tuning of parameters. Parameter definitions and values for the quantitative model are summarized in Table 4.1.

In the model the total number of cellular PEX5 (N_5) is held fixed, as is the cytoplasmic volume (V_{cyto}), but the number of cytoplasmic PEX5 will vary as they cycle between the cytosol and the peroxisomes. We stochastically add cargo to the cytosol at fixed rate Γ_{cargo}. We assume the association rate is fast, and so we immediately bind cargo to any cytoplasmic PEX5 without cargo. Cargo accumulates in the cytosol if free PEX5 is not available. PEX5-cargo is removed from the cytosol when it binds to a peroxisome importomer [42] with a diffusion-limited rate Γ_{bind} that depends on the number of importomers with available binding sites.

We generally assume that for each importomer there can be at most one ubiquitinated PEX5 by not allowing the RING complex to associate with more than one PEX5. We do not explicitly model RING complex motion or PEX5 motion within a given importomer, but once a ubiquitinated PEX5 has been removed from the peroxisome we allow ubiquitination of another PEX5 at a rate Γ_{Ub}. We have checked that our results are qualitatively unchanged, though with slightly higher ubiquitin levels, if we instead allow the RING complex to ubiquitinate all of the PEX5 associated with an importomer (see Fig. 4.8).

The AAA complex can remove ubiquitinated PEX5 from the peroxisomal membrane while the complex is transiently associated with the importomer [54]. This export occurs with a diffusion-limited rate Γ_{AAA} that depends on the number of export complexes, together with the number of importomers with ubiquitinated PEX5.

Every importomer is initially primed with a single PEX5 that is not ubiquitinated, since we do not have peroxisome or importomer biogenesis processes in our model. For most of our results, the system is run for ten simulated minutes, but data is not taken until after the first 10 simulated seconds; the simulation has reached steady state after this time and is run longer for improved statistics. The peroxisomal PEX5

fraction and ubiquitin per peroxisome are recorded every simulated 0.1s. Average times above and below thresholds in Figs. 4.5(B) and (C) were measured differently, as described below. Vertical bars indicate standard deviations. Statistical error bars are much smaller than the standard deviations, and are much smaller than the size of data points.

Diffusion-limited Rates

Both cytosolic PEX5-cargo and E2-ubiquitin [41] diffuse to bind with peroxisomal importomers on the peroxisomal surface. The diffusion limited binding rate per importomer in terms of the appropriate cytosolic concentration c and diffusivity D, peroxisomal radius r, and number N of available importomers each of radius s is [117]

$$R_{3d} = \frac{4\pi Dcsr}{Ns + \pi r}. \tag{4.1}$$

We use this to determine PEX5-cargo binding rates, so that $\Gamma_{bind} = R_{3d}$ where $D = D_{PEX5}$ is the PEX5-cargo diffusivity, $c = c_{PEX5}$ is the PEX5-cargo concentration, and N is the number of importomers with available binding sites — and both c and N are time-dependent. We also use this to determine ubiquitination rates, so that $\Gamma_{Ub} = R_{3d}$ where $c = c_{E2-Ub}$, $D = D_{E2-Ub}$, and N is the number of importomers without ubiquitinated PEX5 but with PEX5 — and only N is time-dependent.

AAA ATPase complexes are thought to transiently interact with importomers [54], so we assume that they diffuse on the peroxisomal membrane. On a surface, each diffusing complex of diffusivity D within a region of radius b will be captured by an absorbing receptor of radius s on average after a time [117]

$$\tau_{2d} = \frac{b^4\ log(b/s)}{2D(b^2 - s^2)} - \frac{3b^2 - s^2}{8D}. \tag{4.2}$$

We take the diffusion limited rate to be the inverse of this time, but proportional to the number N_{AAA} of AAA complexes, so that $\Gamma_{AAA} = N_{AAA}/\tau_{2d}$ where s is the importomer radius and $D = D_{AAA}$. Assuming that the peroxisomal surface (sphere of radius r) is evenly divided among N importomers that have ubiquitinated PEX5 then $4\pi r^2 = \pi b^2 N$ — i.e. $b = 2r/\sqrt{N}$. Unless otherwise noted, we assume that $N_{AAA} = N_I$, i.e. a 1:1 stoichiometry of AAA complexes and importomers.

4.2.3 Computational Model Parameterization

Table 4.1: **Model Parameter Definitions and Values.** Shown are standard values used. Further discussion can be found in the Methods section.

Variable	Description	Value/Eqn
c_{PEX5}	PEX5-cargo cytosolic concentration	variable
c_{E2-Ub}	concentration of E2 enzyme with ubiquitin	$300\mu\text{m}^{-3}$
D_{PEX5}	PEX5-cargo diffusivity	$0.72\mu\text{m}^2/\text{s}$
D_{E2-Ub}	diffusivity of E2 enzyme with ubiquitin	$1.04\mu\text{m}^2/\text{s}$
D_{AAA}	diffusivity of AAA export complex	$0.036\mu\text{m}^2/\text{s}$
Γ_{cargo}	rate of addition of matrix proteins to cytosol	Varied
Γ_{bind}	PEX5-cargo binding rate to empty importomer site	Eqn. 4.1
Γ_{Ub}	rate of ubiquitination of PEX5 at importomer	Eqn. 4.1
Γ_{AAA}	rate of export of ubiquitinated PEX5	Eqn. 4.2
N_P	number of peroxisomes	100
N_I	number of importomers per peroxisome	150
N_{AAA}	number of AAA export complexes per peroxisome	150
N_5	total number of cellular PEX5	3×10^5
r	peroxisome radius	$0.25\mu\text{m}$
s	importomer radius	7.2nm
V_{cyto}	cytosolic volume	$1776\mu\text{m}^3$

To approximate the diffusivity of PEX5 in the cytosol we note that the diffusion constant of EYFP in the cytosol has been measured at $0.75\pm0.3\mu\text{m}^2/\text{s}$ for NLFK cells and $1.83 \pm 0.28\mu\text{m}^2/\text{s}$ in HeLa cells [149]. We assume globular shape, and scale the diffusivity with the inverse radius, and the radius with the cube-root of the molecular mass. The molecular mass of PEX5 is 70kDa [150] with an additional 49kDa for cargo [38] giving $M_{tot} = 119\text{kDa}$. Using $D_{YFP} = 1\mu\text{m}^2/\text{s}$ with mass $M = 27\text{kDa}$, this gives $D_{PEX5} = 0.72\mu\text{m}^2/\text{s}$.

Monoubiquitination of PEX5 in mammals is associated with the cytosolic UbcH5 family of proteins [41], which have a molecular mass of 16kDa [151, 152]. Adding ubiquitin (8 kDa) we have $M_{tot} = 24\text{kDa}$, which scaled from YFP gives a diffusivity $D_{E2-Ub} = 1.04\mu\text{m}^2/\text{s}$. HeLa cell extracts have a UbcH5 concentration of $c_{E2-Ub} = 0.5\mu\text{M} = 300\mu\text{m}^{-3}$ [153], assuming most of the E2 is activated with ubiquitin.

Diffusion in membranes of rat basophil leukemia (RBL) cells has a measured diffusion constant of $3 \times 10^{-10}\text{cm}^2/\text{s} = 0.03\mu\text{m}^2/\text{s}$ [154]. It has also been measured to be $0.1\mu\text{m}^2/\text{s}$ for mammals and $0.0025\mu\text{m}^2/\text{s}$ in yeast [155]. Most recently membrane

diffusivity has been measured in yeast as $0.036\mu\text{m}^2/\text{s}$ [156]. We use this most recent value, $D_{AAA} = 0.036\mu\text{m}^2/\text{s}$, for the diffusivity of the export complex within the peroxisomal membrane.

The radius of a globular protein or protein complex can be approximated by $R = 0.066M^{1/3}$ for R in nm and M in Daltons [157]. We estimate the size of an importomer complex by including both the docking machinery involving PEX14 and the RING complex, which have masses of 800 kDa and 500 kDa respectively [44]. For a total mass of 1300 kDa we obtain a radius of $s = 7.2\text{nm}$.

Since very little is known about the population structure of peroxisomes, we use a fixed peroxisomal radius $r = 0.25\mu\text{m}$ in the middle of the range of reported peroxisomal sizes (0.1 - 0.8μm in diameter [13]). We use $N_P = 100$ peroxisomes, unless otherwise stated, which for purposes of computational efficiency is slightly smaller than the average number of 300 reported for mammalian cells [20]. For a spherical cell of radius 10μm, with 44.4% cytosol [38], then $V_{cyto} = 1776\mu\text{m}^3$. This is used to obtain concentrations of PEX5-cargo. A measured cytoplasmic concentration of PEX5, $c = 0.75\mu\text{M}$ [38], corresponds to approximately 8×10^5 PEX5. We take a comparable but smaller number $N_5 = 3 \times 10^5$, corresponding to the slightly smaller number of peroxisomes in our system.

We set the number of importomers per peroxisome $N_I = 150$. With $N_5 = 3 \times 10^5$, this works out to 20 PEX5 per importomer when $N_P = 100$. This is much more than the number of possible PEX5 binding sites w per importomer that we explore, which reflects the small proportion of PEX5 typically reported on peroxisomes [158].

Threshold Calculations

For the numerical computation of average time intervals above and below specific ubiquitination thresholds, shown below in Figs. 4.5(B) and (C), we found that the averages are biased towards smaller intervals in short simulations. Accordingly, data was taken until averages no longer increased with increased sampling, where we increased the number of intervals averaged in factors of ten. For a threshold of 50 ubiquitin, this required 10^5 intervals and for all other thresholds this required 10^4 intervals.

We also found that the distribution of time-intervals either above or below specific

ubiquitin thresholds was bimodally distributed. Fig. 4.9 shows an example distribution of recorded times spent below a threshold of 100 ubiquitin. We found that all distributions have a short-time peak below 10^{-4}s and another above 10^{-4}s. The shorter peak arises from many rapid crossings of the threshold (see Fig. 4.5(A) for an example trajectory) and are unlikely to be resolvable experimentally or be relevant to autophagy regulation. Accordingly, interval times below 10^{-4}s were not included in the computation of average intervals.

4.3 Results/Discussion

4.3.1 Uncoupled and Directly Coupled PEX5 and Ubiquitin Dynamics

We first examined uncoupled and directly coupled models of protein translocation coupling, shown schematically in Figs. 4.2(A)-(B) and (C), respectively. As mentioned above, the dynamics of PEX5 and ubiquitin are indistinguishable for these two models. We consider different number of sites w on each importomer for PEX5 binding in Fig. 4.3, guided by studies showing distinct [43, 56, 159] PEX5:PEX14 stoichiometries on the peroxisomal surface — as well as explicit suggestions of multiple PEX5 sites at the importomer [144]. For each w, we vary the cargo addition rate Γ_{cargo} and consider both PEX5 populations and ubiquitination levels.

As shown in Fig. 4.3(A), the cytosolic PEX5-cargo concentration increases approximately linearly for small Γ_{cargo} then sharply increases before reaching a constant plateau at larger Γ_{cargo}. The linear regime arises from a dynamic balance between cytosolic concentration and concentration-dependent binding to peroxisomes through Γ_{bind}. The plateau arises from saturation of the PEX5 cycling rates, together with complete binding of cytoplasmic PEX5 with cargo. The steep rise before the plateau occurs when the PEX5 cycling becomes rate limited by PEX5 removal through Γ_{AAA}, and coincides with sharply increased peroxisomal PEX5 fraction (see below) — essentially more and more importomers are fully occupied by PEX5 and so cannot contribute to PEX5-cargo binding (see Fig. 4.4(A) inset). Increasing the number of binding sites per importomer, w, decreases the cytosolic fraction of PEX5-cargo. The experimentally measured value of $c = 450\mu\text{m}^{-3}$ (0.75μM [38]) is consistent with all w, and roughly corresponds to where the PEX5-cargo concentration sharply increases

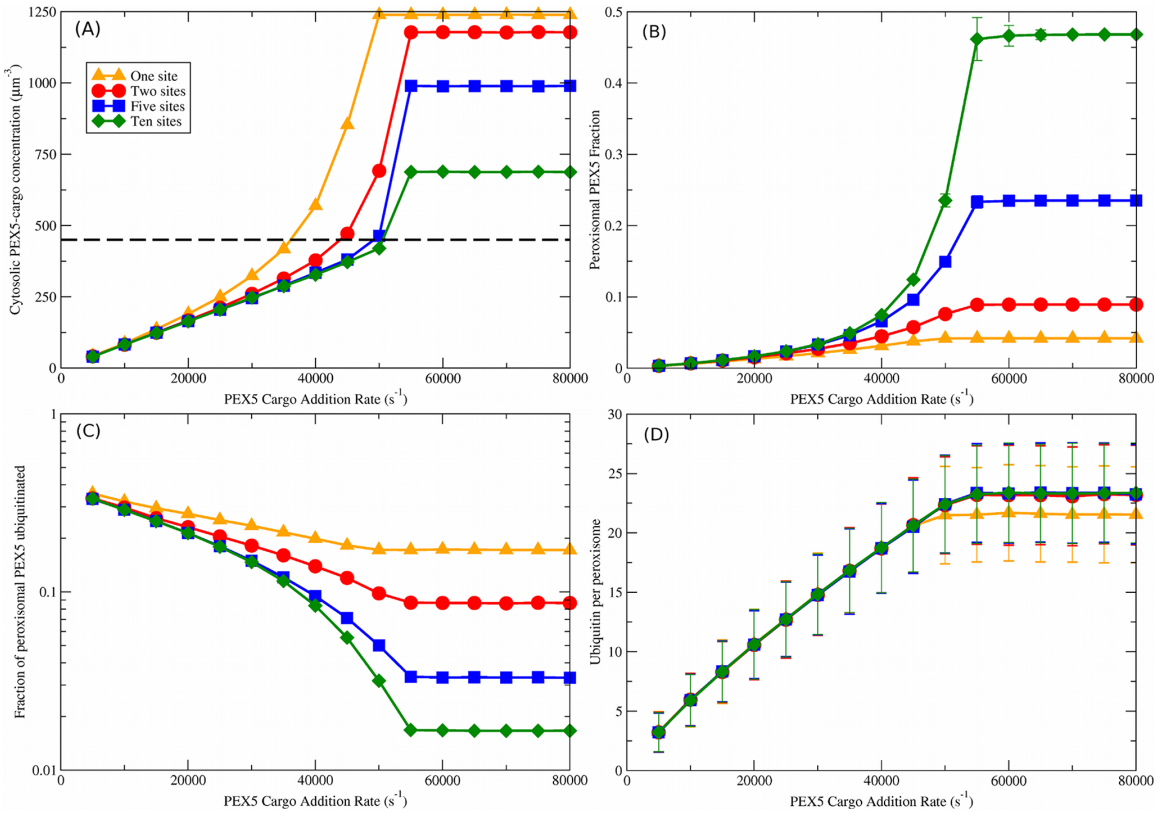

Figure 4.3: **Uncoupled and Directly Coupled Cargo Translocation.** Both uncoupled and directly coupled translocation models have identical PEX5 and ubiquitination behavior and so they are reported together. (A) cytosolic PEX5-cargo concentration vs. cargo addition rate, Γ_{cargo}. Different numbers of binding sites per importomer are shown from $w = 1$ (orange triangles) to $w = 10$ (green diamonds), as shown in the legend; the legend also applies to (B), (C), and (D). The dashed black line is the measured cytosolic PEX5 concentration of $0.75\mu\text{M} = 450\mu\text{m}^{-3}$ [38]. This is consistent with $\Gamma_{cargo} \approx 50000/s$ when $w = 5$. (B) Peroxisomal PEX5 fraction vs. Γ_{cargo}. (C) Fraction of peroxisomal PEX5 that is ubiquitinated vs. PEX5 cargo addition rate, Γ_{cargo}. (D) Ubiquitin per peroxisome vs. Γ_{cargo}. A characteristic increase of ubiquitination with Γ_{cargo} is seen that is largely independent of the number of binding sites w. Vertical bars represent the standard deviation of observed values; error bars are smaller than point sizes.

due to saturation of importomer binding sites (around $\Gamma_{cargo} \approx 50000/\text{s}$).

Mirroring cytosolic PEX5-cargo concentrations, Fig. 4.3(B) shows that the peroxisomal PEX5 fraction also increases with Γ_{cargo}. The mutual increase is possible with a fixed number of PEX5 (N_5) at the expense of the reservoir of cytosolic PEX5 that is not associated with cargo. PEX5 accumulates on the peroxisome because of the increasing binding rate due to increasing cytosolic PEX5-cargo concentrations. Increasing the number of binding sites per importomer w increases the peroxisomal fraction of PEX5. Fig. 4.3(C) shows us that we have a lower fraction of ubiquitinated PEX5 as the cargo addition rate increases. This reflects the higher peroxisomal PEX5 fraction, in combination with our restriction that at most one PEX5 can be ubiquitinated on each importomer. Since the peroxisomal fraction increases with the number of binding sites w, while the restriction remains unchanged, the ubiquitinated fraction decreases with increasing w.

The number of ubiquitinated PEX5 per peroxisome is shown in Fig. 4.3(D). The number of ubiquitin increases roughly linearly with Γ_{cargo} until it reaches a plateau slightly above 20 ubiquitin per peroxisome. The plateau value corresponds to the balance between ubiquitination (Γ_{Ub}) and export (Γ_{AAA}). With the uncoupled and directly coupled models of translocation, neither of these processes depend on the number of PEX5 bound to an importomer — so the plateau is independent of w. An exception is when $w = 1$, since the importomer is empty after every PEX5 export and this slightly decreases the ubiquitination rate. In comparison with the peroxisomal fraction of ubiquitinated PEX5 (Fig. 4.3(B)), there is a significantly larger standard deviation for the ubiquitin per peroxisome. The difference arises since each cellular fraction is averaged over $N_P = 100$ peroxisomes while ubiquitin per peroxisome is not.

4.3.2 Cooperatively Coupled PEX5 and Ubiquitin Dynamics

We have measured the same quantities for the cooperatively coupled model as for the uncoupled and directly coupled models. The cooperatively coupled results for cytosolic PEX5-cargo concentration, shown in Fig. 4.4(A), are very similar to those for uncoupled and directly coupled, shown in Fig. 4.3(A). Results with only one binding site per importomer ($w = 1$) are not shown, as at least two PEX5 are needed

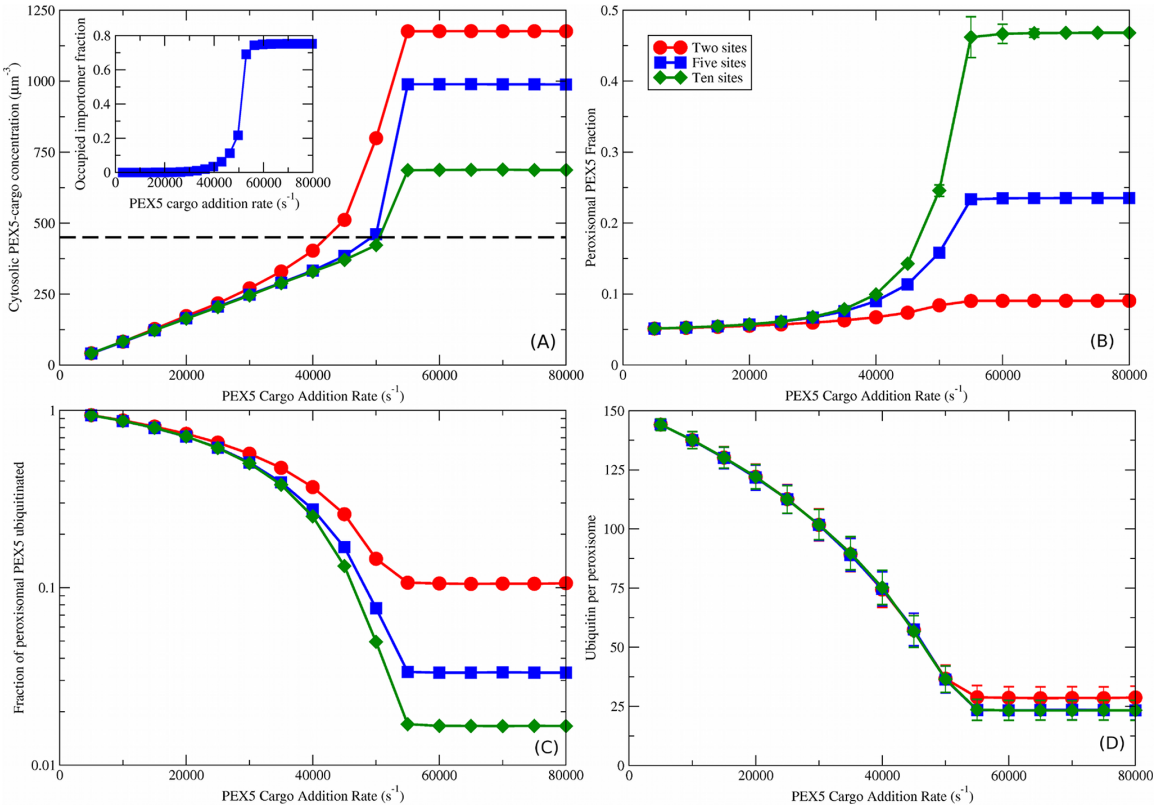

Figure 4.4: **Cooperatively Coupled Cargo Translocation.** (A) Cytosolic PEX5-cargo concentration vs. PEX5 cargo addition rate, Γ_{cargo}. The dashed black line is the measured cytosolic PEX5 concentration of $0.75\mu\text{M} = 450\mu\text{m}^{-3}$ [38]. Inset shows the fraction of importomers that are fully occupied by PEX5 vs. PEX5 cargo addition rate, with five PEX5 sites per importomer and cooperative coupling. (B) peroxisomal PEX5 fraction vs. Γ_{cargo} for cooperatively coupled cargo translocation. (C) Fraction of peroxisomal PEX5 that is ubiquitinated vs. Γ_{cargo}. (D) ubiquitin per peroxisome vs. Γ_{cargo}. A characteristic decrease of ubiquitination with Γ_{cargo} is seen that is largely independent of the number of binding sites w. Different number of binding sites per importomer are shown from $w = 2$ (red circles) to $w = 10$ (green diamonds), as shown in the legend in (B). Cooperative coupling cannot function with $w = 1$, so that is not shown. Subsequent figures use $w = 5$ (blue squares). Note that the vertical scale of ubiquitin per peroxisome in (D) is much larger than in Fig. 4.3.

for translocation and export with cooperative coupling.

Peroxisomal PEX5 accumulation with cooperative coupling (Fig. 4.4(B)) is also similar to uncoupled and directly coupled (Fig. 4.3(B)). One important difference is that at low cargo addition rates Γ_{cargo} the peroxisomal PEX5 fraction vanishes for uncoupled and directly coupled but approaches a finite value (approximately 5%) with cooperatively coupled translocation. We see from Fig. 4.4(B) that cooperative coupling implies a finite ratio between the peroxisomal fraction at high and low Γ_{cargo}, and that this ratio is controlled by the number of binding sites per importomer w. A 1:5 ratio of PEX5:PEX14 has been reported in normal conditions [56], and a 1:1 ratio when PEX5 export is blocked [43]. Assuming PEX14 levels do not change with cargo traffic, these observations imply a 1:5 ratio of PEX5 in low:high Γ_{cargo} conditions, or $w \approx 5$ for cooperatively coupled translocation. With this choice of w, we also recover an absolute change of peroxisomal PEX5 between 5% in wild-type cells to 25% in those lacking a RING complex [158, 159]. The 1:5 ratio is also possible with uncoupled and directly coupled models, but requires fine-tuning of Γ_{cargo}.

The cooperatively coupled results for the fraction of peroxisomal PEX5 that is ubiquitinated, shown in Fig. 4.4(C), are also similar to those for uncoupled and directly coupled, shown in Fig. 4.3(C). One important difference is that the ubiquitinated peroxisomal fraction approaches 100% for small Γ_{cargo} with cooperative coupling. Each importomer has at least one bound PEX5, and small Γ_{cargo} allows the bound PEX5 to be ubiquitinated long before a second PEX5 binds and allows cooperative translocation to occur.

The number of ubiquitin per peroxisome vs. the cargo addition rate Γ_{cargo}, shown in Fig. 4.4(D) for cooperative coupling, shows strikingly different behavior from uncoupled and directly coupled translocation models. We see that the number of ubiquitin per peroxisome decreases with increasing Γ_{cargo}. The amount of ubiquitinated PEX5 is high for low cargo addition rates because ubiquitinated PEX5 must wait for another PEX5 to arrive before it can be exported. Ubiquitinated PEX5 decreases as the cargo addition rate increases since PEX5-cargo arrives at the peroxisome more rapidly, allowing ubiquitinated PEX5 to be exported. At large Γ_{cargo}, the asymptotic number of ubiquitinated PEX5 is approximately the same between the uncoupled and directly coupled, and cooperatively coupled translocation models. A slightly higher

level is seen for cooperatively coupled translocation with $w = 2$, since after translocation the remaining PEX5 must wait for both ubiquitination and another PEX5 binding in the cooperative model.

Similar results have also been obtained for the five-site cooperatively coupled model without the restriction of only a single ubiquitinated PEX5 on each importomer. Fig. 4.8 shows that the single ubiquitin restriction does not qualitatively change the PEX5 or ubiquitin behaviours.

The cooperatively coupled model leads to high ubiquitin levels when there is little cargo addition. Since ubiquitinated peroxisomes will be degraded in mammals [18, 160] through NBR1 signalling of autophagy [19], high ubiquitin levels could be used as a degradation signal for peroxisomal disuse. We explore how a threshold level of ubiquitination could function as a trigger for specific peroxisomal autophagy (pexophagy) in greater detail below. We restrict ourselves to a five-site ($w = 5$) cooperatively coupled model of cargo translocation, since this recovers reported PEX5:PEX14 stoichiometries [43, 56] and a fivefold change in peroxisomal PEX5 when RING activity is absent [159].

4.3.3 Ubiquitin Thresholds with Cooperative Coupling

A simple threshold model of pexophagy would trigger peroxisomal degradation when the number of ubiquitin on a peroxisome exceeds a certain threshold. While this appears straightforward in light of the average ubiquitin levels of Fig. 4.4(D), the substantial fluctuations around these averages must be considered.

To illustrate the challenge, in Fig. 4.5(A) we show a time-trace of the number of ubiquitin for a single peroxisome when $\Gamma_{cargo} = 45000/\text{s}$ and $w = 5$ with cooperatively coupled translocation. This value of Γ_{cargo} is chosen to lead to a relatively low level of ubiquitination (see Fig. 4.4(D)). Also shown with dashed lines are two example thresholds, at 50 and at 75 ubiquitin, which are below and above the rounded average of 58 ubiquitin. Stochastic fluctuations in the ubiquitination level lead to crossing of both thresholds.

To investigate stochastic threshold crossing more systematically, we show in Figs. 4.5(B) and (C) the average interval of time spent above and below various thresholds, respectively. We consider four thresholds, chosen between the minimum and maximum

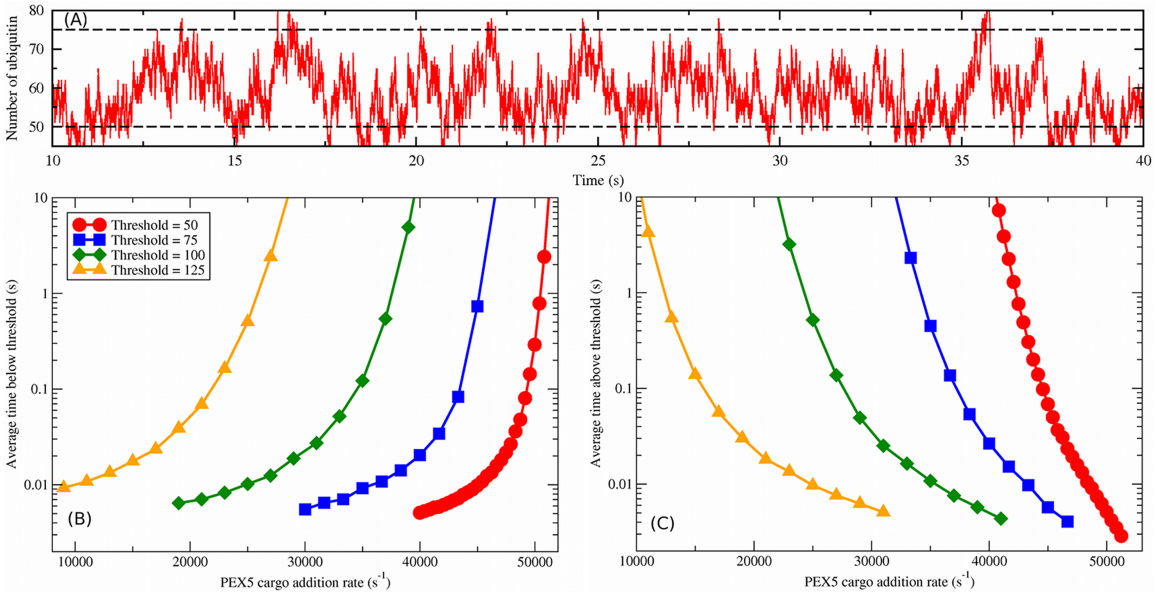

Figure 4.5: **Ubiquitin Thresholds for Cooperative Coupling.** (A) Example time dependence of total peroxisomal ubiquitin for cargo addition rate $\Gamma_{cargo} = 45000/\text{s}$, with the default number of peroxisomes ($N_P = 100$) and importomers per peroxisome ($N_I = 150$). The characteristic timescale for fluctuations in the ubiquitination level is several seconds. Two possible threshold values are illustrated with dashed lines. (B) The average interval of time spent below a given threshold vs. Γ_{cargo} for thresholds as indicated by the legend, which also applies to (C). (C) The average interval of time spent above a given threshold vs. Γ_{cargo}.

ubiquitin levels from Fig. 4.4(D), as indicated in the legend. For a given threshold, we only present data from a relatively narrow range of cargo addition rates Γ_{cargo}. Beyond this range the threshold is only very rarely crossed, and any such crossings are very brief. This is true whether we are considering a threshold above or below the mean ubiquitin level.

The ubiquitin level is able to fluctuate over a given threshold number only for a limited range of PEX5 cargo addition rates. Within this range, the amount of time spent on either side of the threshold changes by more than three orders of magnitude. Since the range is limited, if the system is outside of the range then a simple threshold model could give a clear signal for pexophagy. Even within the range, a simple threshold model may be sufficient because the time spent on either side of the threshold changes very rapidly with changing cargo addition rate. If the pexophagy response is sufficiently slow, rapid excursions across the threshold might be ignored. It would be interesting to study how NBR1 accumulation [19] might refine this scenario.

4.3.4 Varying Peroxisome Number with Cooperative Coupling

In mammals, the proliferation of peroxisomes can be stimulated by treatment with peroxisome proliferators [161]. After treatment with the proliferators is stopped the expression of peroxisomal matrix proteins (cargo) and peroxisome biogenesis factors decrease [162, 163] and the number of peroxisomes rapidly returns to normal levels [84, 134]. In mammals, 70-80% of peroxisome degradation in these circumstances is performed by autophagy [83]. Because the degradation of ubiquitinated peroxisomes is by autophagy [18, 19, 160], it is then plausible that the ubiquitin disuse signal we have proposed to signal degradation is involved in returning the peroxisome population to normal levels.

To investigate whether the ubiquitin disuse signal could be involved in returning cells to normal peroxisome levels, we have held the number of total PEX5 in our system constant and varied the number of peroxisomes, considering both a halving and doubling of the number. The peroxisomal PEX5 fraction for 50, 100, and 200 peroxisomes is shown in Fig. 4.6(A) and it behaves as expected: the increase from low PEX5 to high PEX5 is preserved, with the 50 peroxisome system halving and the

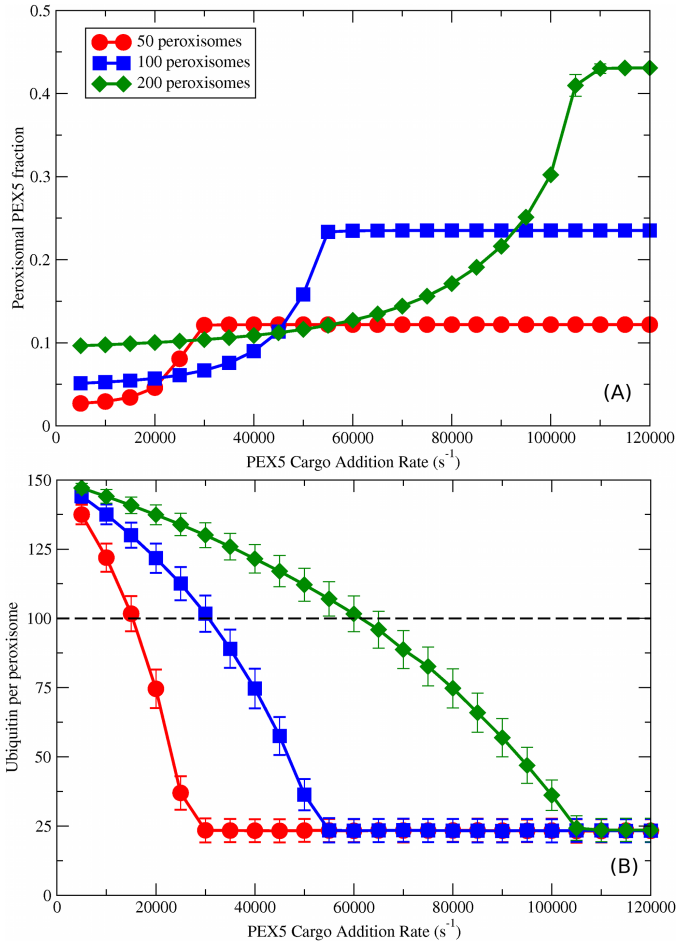

Figure 4.6: **Peroxisome Number Variation for Cooperative Coupling.** Here we investigate the effects of varying the number of peroxisomes (N_P, as indicated by legend in (A)) when the other parameters are kept constant (with $w = 5$ sites per importomer). (A) Peroxisomal PEX5 fraction vs. Γ_{cargo} for cooperatively coupled cargo translocation. (B) Ubiquitin per peroxisome vs. Γ_{cargo}. Horizontal black dashed line represents a possible ubiquitin threshold for peroxisome degradation.

200 peroxisome system doubling the peroxisomal PEX5 fraction relative to the 100 peroxisome system.

As seen in Fig. 4.6(B), the peroxisomal ubiquitin accumulation curve is a similar shape for all three N_P, but with systematically *lower* ubiquitin accumulation for fewer peroxisomes at a given Γ_{cargo}. This reflects the role of PEX5-cargo traffic in clearing ubiquitin from importomers, within the cooperative coupling model of translocation. This could then provide the cell with a straightforward feedback mechanism to adjust the number of peroxisomes to match the rate of matrix protein expression. At a given Γ_{cargo} and a given ubiquitin threshold, between approximately 50 and 125 in this instance, an excess of peroxisomes would lead peroxisomes to be above the threshold and subsequently degraded. As they are degraded the ubiquitin level would decrease, until a stable number of peroxisomes was reached with ubiquitin levels below the threshold.

Given that ubiquitin signals degradation through autophagy [18, 19, 160], this mechanism is consistent with observations that autophagy is responsible for the degradation of excess peroxisomes in mammals [84]. Peroxisome proliferators increase the expression of PEX5 cargo proteins, and removing proliferators results in a decrease of cargo proteins [162, 163]. We have shown that this decrease in cargo would increase the level of ubiquitinated PEX5 on peroxisomes, and could then induce peroxisome degradation through this simple threshold model. Once decreased peroxisomal numbers reduced ubiquitin numbers below the threshold, background levels of peroxisomal biogenesis would stabilize peroxisomal numbers. Decrease of peroxisomal numbers above the threshold would occur rapidly, while increase below the threshold would be slow in the absence of a proliferation signal.

4.3.5 Varying Export Complex Number with Cooperative Coupling

We have been unable to determine the number of AAA export complexes on each peroxisome from the literature. Since PEX1 and PEX6 only transiently associate with peroxisomes [164] we may not have, as we assume, $N_{AAA} = N_I$. For example, the reduction in PEX26 expression during the removal of peroxisome proliferating signal [165] would result in the decrease of PEX1 and PEX6 on peroxisomes. Peroxisomal damage may also change the stoichiometry of N_{AAA}/N_I.

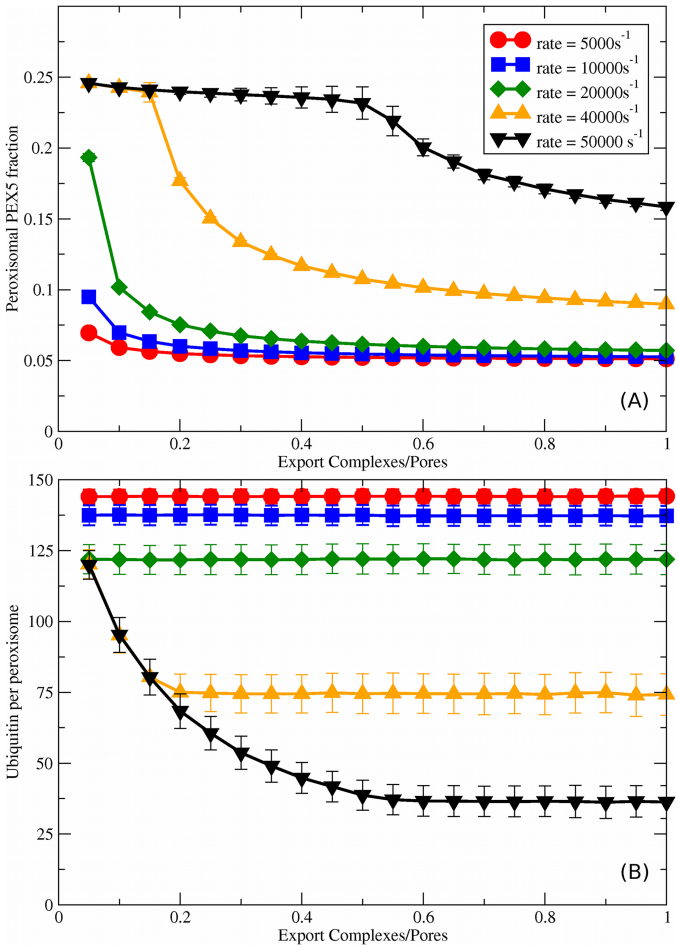

Figure 4.7: **Export Complex Number Variation for Cooperative Coupling.** For cooperatively coupled systems with $N_P = 100$, $N_I = 150$, and $w = 5$ we vary the number of export complexes N_{AAA}, which directly scales the PEX5 export rate, Γ_{AAA}. (A) Peroxisomal PEX5 fraction vs. stoichiometry of export complexes to importomers (N_{AAA}/N_I). As shown in the legend, we consider different fixed rates of cargo addition, Γ_{cargo}; this legend also applies to (B). (B) Ubiquitin per peroxisome vs. N_{AAA}/N_I, for the same set of Γ_{cargo}.

Fig. 4.7(A) shows the peroxisomal PEX5 fraction vs N_{AAA}/N_I for the different Γ_{cargo} indicated by the legend. The peroxisomal PEX5 fraction is independent of larger N_{AAA}/N_I ratios, indicating that our results will not be very sensitive to our choice of $N_{AAA} = N_I$. Nevertheless, at smaller ratios the peroxisomal PEX5 fraction increases as export becomes impaired. This happens first at larger Γ_{cargo}, as expected.

Corresponding to PEX5 changes, the peroxisomal ubiquitin is shown in Fig. 4.7(B). Again, at larger N_{AAA}/N_I ratios the ubiquitin levels are unchanged. However, as the ratios get smaller the ubiquitin per peroxisome increases — and this happens first at higher Γ_{cargo}. This means that if the AAA complex numbers of a particular peroxisome are significantly decreased, the ubiquitination levels of that peroxisome will increase. Nevertheless, for smaller Γ_{cargo} the ubiquitin levels do not change until the number of AAA complexes is below 5% of the number of importomers. This suggests that peroxisomes may be resilient to losses of export complexes, except at high Γ_{cargo}.

4.3.6 Summary and Further Discussion

We have modelled PEX5 cycling through the peroxisomal importomer, and measured the temporal dynamics of both PEX5 and ubiquitinated PEX5 associated with peroxisomes, as the matrix cargo traffic is varied via Γ_{cargo}. PEX5 cycling takes matrix proteins from the cytosol to the peroxisome, where they translocate into the peroxisomal matrix. However, the energetics of cargo translocation have remained unclear.

We have implemented three models of cargo translocation, illustrated in Figs. 4.1 and 4.2. The first is uncoupled cargo translocation, where the translocation of cargo happens spontaneously on PEX5-cargo association with a peroxisomal importomer. The second is directly coupled translocation, where cargo translocation happens at the same time as export of the ubiquitinated PEX5 to which the cargo is attached. The third is cooperatively coupled translocation, where cargo translocation happens at the same time as export of a different ubiquitinated PEX5 from the PEX5 to which the cargo is attached. Both directly coupled and cooperatively coupled models have cargo translocation driven by the AAA-dependent export of PEX5 from the peroxisomal membrane [63, 62].

All three translocation models have peroxisomal ubiquitin numbers that strongly

depend on matrix cargo protein traffic. Both uncoupled and directly coupled translocation models have indistinguishable PEX5 and ubiquitin dynamics in which peroxisomal ubiquitinated PEX5 increases as cargo traffic increases. In contrast, cooperatively coupled translocation has decreasing levels of peroxisomal ubiquitinated PEX5 as cargo traffic increases.

Ubiquitin on the surface of peroxisomes leads to the recruitment of NBR1, which recruits the autophagic machinery [19] and leads to peroxisome degradation [19, 18]. For cooperatively coupled translocation, ubiquitin buildup at low cargo traffic could be used as a disuse signal to initiate autophagic peroxisome degradation. This feedback mechanism could be used to rapidly return peroxisome numbers to normal after induced peroxisome proliferation [161, 84, 83].

For uncoupled and directly coupled translocation models, the increase of ubiquitin levels at high cargo traffic levels means that to avoid unwanted pexophagy at high cargo traffic the autophagic response to ubiquitin must be insensitive to the maximal levels of PEX5-ubiquitin expected. This then provides a challenge to identify ubiquitinated peroxisomal membrane proteins other than PEX5 that could control pexophagy. If we assume that peroxisomal damage has a range of severity, with lightly damaged peroxisomes avoiding pexophagy, this also implies that additional pexophagy of lightly damaged peroxisomes would be quickly triggered by increases in matrix cargo traffic — as the PEX5-ubiquitin levels tipped the balance of these peroxisomes towards pexophagy.

This work investigates only the cycling and mono-ubiquitination of PEX5. We do not model the ubiquitination of other proteins or polyubiquitination of PEX5. How might these effect pexophagy signalling and/or PEX5 cycling? Polyubiquitinated PEX5 can be removed from the peroxisome membrane by the AAA complex [166], and polyubiquitinated PEX5 is targeted for degradation [140, 141, 142]. We assume that this background process does not significantly change PEX5 levels as cargo traffic is changed. While the ubiquitination of other peroxisomal proteins, including the polyubiquitination of PEX5, can contribute to the induction of autophagy [18, 160], we assume that these ubiquitination levels do not change significantly as cargo traffic is varied. If so, then they will simply bias or offset the PEX5 mono-ubiquitination signal and any threshold could be appropriately shifted as well. Here, we have focused

on PEX5 and its accumulation on the peroxisomal membrane during changes in the import of matrix cargo. If ubiquitination of proteins other than PEX5, or polyubiquitination of PEX5, do change significantly as cargo traffic is varied, then they will need to be considered in conjunction with the PEX5 cycling of our model.

A 1:5 ratio of PEX5:PEX14 is observed with normal conditions [56], and a 1:1 ratio in systems with no PEX5 export [43]. This fivefold change is also observed when peroxisomal PEX5 goes from 5% in wild-type to 25% in cells without a functional RING complex [159, 158], implying no ubiquitination and so no export. It is possible to recover this fivefold change with uncoupled and directly coupled translocation, but only by tuning parameters – and only for specific Γ_{cargo} values. These ratios are more naturally recovered for a five-site importomer with cooperatively coupled translocation because with cooperative coupling the importomer cannot remove all PEX5. The 1:5 ratio would then correspond to low cargo traffic, and the 1:1 ratio to high cargo traffic or no export.

Miyata *et al.* [167] were able to measure peroxisome associated PEX5 and ubiquitinated-PEX5. Our modelling indicates that PEX5 cycling responds in just a few seconds to changes in matrix cargo traffic. This response is much faster than timescales to change other protein expression or peroxisome numbers, so we expect that changes in peroxisomal ubiquitin with traffic could directly distinguish between the contrasting predictions of uncoupled or directly coupled translocation models and cooperatively coupled translocation models. From Fig. 4.3(D) and Fig. 4.4(D), we see that in the linear regime a doubling of matrix cargo traffic leads to a doubling of peroxisomal PEX5-ubiquitin for uncoupled or directly coupled models, and a halving of peroxisomal PEX5-ubiquitin for the cooperatively coupled model. Complicating this is that we might expect to be close to the end of the linear regime (i.e. $\Gamma_{cargo} \approx 50000\text{s}^{-1}$) in normal conditions, so that the linear response would be seen only for a marked decrease of matrix cargo traffic. Nevertheless, we might expect to be in the linear regime after induced peroxisomal proliferation and before pexophagy has reduced the number of peroxisomes significantly.

Our model is tuned for mammalian peroxisomes, since the E2 enzyme for monoubiquitination of PEX5 is cytosolic and is embodied in our model via a 3d diffusion-limited rate Γ_{Ub} from Eqn. 4.1. In yeast, the E2 for monoubiquitination of Pex5 is Pex4, which

is attached to the peroxisome membrane by Pex22 so that Γ_{Ub} should be determined by a 2d diffusion-limited rate from Eqn. 4.2. We do not expect any qualitative changes to the Pex5 cycling because of this, and cooperatively coupled translocation should lead to an increase of ubiquitinated Pex5 in yeast when matrix cargo traffic is reduced. This could be used to probe the translocation mechanism of peroxisomal matrix proteins in yeast. Nevertheless, the role of peroxisomal ubiquitin in pexophagy appears to be, at best, indirect in yeast [8, 83, 168, 169] so that our discussion of ubiquitin thresholds and pexophagy is restricted to mammalian systems.

4.4 Supporting Information

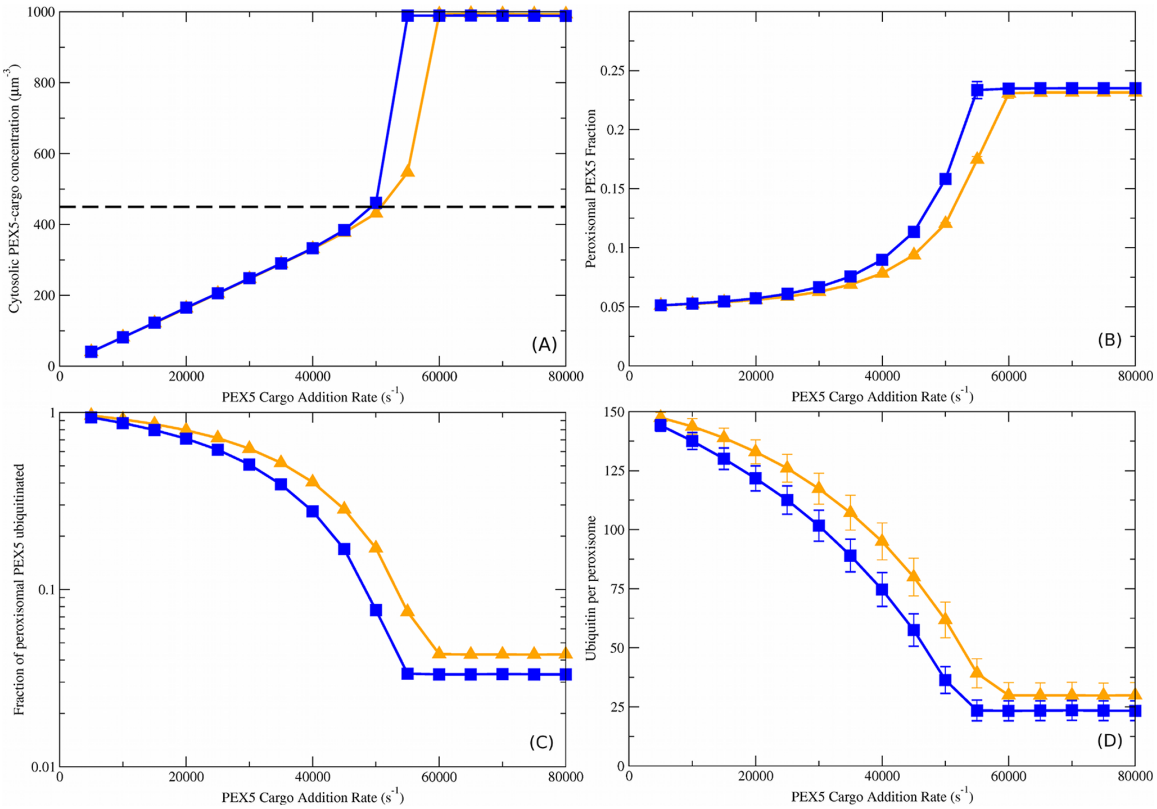

Figure 4.8: **Allowing Multiple Ubiquitin per Importomer, with Cooperative Coupling.** We generally impose a restriction that each importomer have at most one ubiquitinated PEX5. Here we relax this restriction for the cooperatively coupled $w = 5$ site model, and allow all bound PEX5 to be ubiquitinated. Blue squares are the same data as Fig. 3, with at most one ubiquitinated PEX5. Orange triangles are without the restriction, and show qualitatively similar behavior. (A) Cytosolic PEX5-cargo concentration vs. PEX5 cargo addition rate, Γ_{cargo}. The dashed black line is the measured cytosolic PEX5 concentration of $0.75\mu\text{M} = 450\mu\text{m}^{-3}$ [38]. (B) peroxisomal PEX5 fraction vs. Γ_{cargo}. (C) Fraction of peroxisomal PEX5 that is ubiquitinated vs. Γ_{cargo}. (D) ubiquitin per peroxisome vs. Γ_{cargo}.

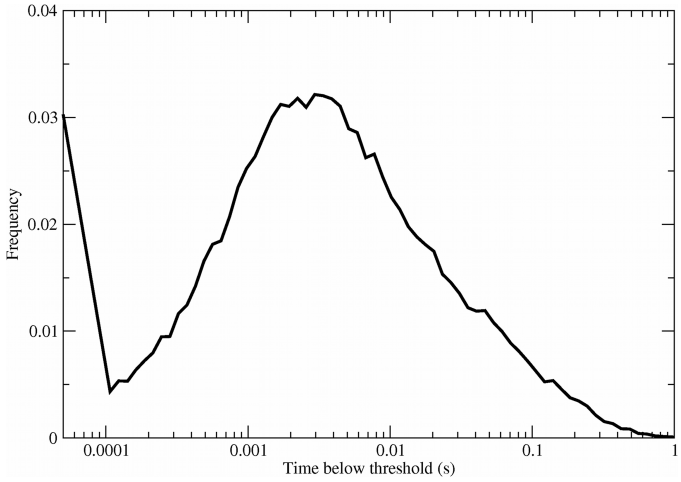

Figure 4.9: **Distribution of Time Intervals Below Ubiquitination Threshold.** Frequency distribution of time intervals spent below a threshold of 100 ubiquitin for the cooperatively coupled five-site model with 100 peroxisomes and $\Gamma_{cargo} = 29000\text{s}^{-1}$. Data is taken for one simulated minute. A characteristic bimodal distribution is seen.

Chapter 5

Cluster Coarsening on Drops Exhibits Strong and Sudden Size-selectivity

This chapter is the paper 'Cluster coarsening on drops exhibits strong and sudden size-selectivity', authored by Aidan I Brown (myself) and Andrew D Rutenberg, published in Soft Matter in 2015, volume 11, pages 3786-3793, doi 10.1039/C5SM00284B, reproduced with the permission of the Royal Society of Chemistry (RSC).

5.1 Introduction

Domain coarsening describes multiple clusters growing in average size but decreasing in number, due to the conserved amount of constituents in the system [108]. Biological coarsening has been considered in models of clustering on bacterial membranes [128, 127] and for membrane polarization [170]. However, these models have focused only on a single membrane or membrane patch, whereas cells have multiple organelles and hence multiple disconnected surfaces.

Autophagy is an important system for the degradation of large cellular substrates [89], including protein aggregates, organelles, and pathogenic bacteria. While autophagy was initially described as a non-selective "self-eating" degradation pathway [5], it is capable of selective substrate degradation. Autophagy substrates are directed to the lysosome for degradation in a multi-stage process that requires receptor protein attachment, and selectivity appears to be mediated by a growing list of autophagy receptor proteins [6]. Although there is a developing understanding of how different receptor proteins select distinct organelles for autophagy [6, 5], e.g. peroxisomes vs. mitochondria, there has been little investigation of how individual organelles are selected from among a subcellular population. Specifically, what physical cues could lead to the selection of individual organelles?

Peroxisomes are drop-like organelles that range in size [13] from $\sim$0.1-0.8 μm , and there can be hundreds in a single mammalian cell [20]. The autophagy of peroxisomes,

or pexophagy, can occur after peroxisome proliferation in order to reduce peroxisome numbers. Intriguingly, this autophagy response varies with peroxisome size [171, 85]. This suggests that organelle size might *directly* affect autophagy selectivity, i.e. size may be directly sensed by the autophagy machinery. We explore that possibility in this paper.

Self-interaction of receptor proteins is common. For the NBR1 receptor, which is necessary and sufficient for pexophagy, self-interaction is driven by coiled-coil domains that are essential for normal autophagy [19]. Consistent with self-interaction, domains of receptor proteins have been observed on the surface of bacteria targeted for autophagy [9, 10]. NBR1 also has the distinctive "J" domain [19] that allows it to anchor to membranes, and that is also essential for normal autophagy. The combination of self-interaction, domains, and membrane anchoring suggests that NBR1 could exhibit biological coarsening dynamics. Since a threshold number of NBR1 appears to be required on a peroxisome to trigger pexophagy [19], coarsening could then be a mechanism to concentrate receptor proteins on particular organelles and so select them for degradation.

In order to understand how the physics of coarsening might influence biological processes such as autophagy substrate specificity, we model the coarsening of surface clusters on a polydisperse collection of spherical drops. There has been little study of coarsening on such a collection of disconnected objects, though coarsening is well understood in bulk systems. For well-separated bulk clusters, coarsening is driven by Ostwald ripening at late times – where material evaporates from clusters smaller than the critical radius r_c and condenses onto clusters larger than r_c [110, 113]. The key features are a growing critical cluster size [111, 112], with $r_c(t) \sim t^{1/3}$, and dynamic scaling [108] of cluster size distributions with respect to $r_c(t)$. While scaling distributions vary with spatial dimension [108, 111, 115, 110], the universal dynamical exponent 1/3 does not [108].

We work in the dilute limit of Lifshitz-Slyozov-Wagner (LSW) [111, 112, 108], with a uniform bulk concentration [111, 108] of molecules $\rho(t)$ that couples clusters on different drops. A uniform bulk concentration is a good approximation when cluster separation is larger than cluster size [111, 110, 108]. Our investigation considers three questions. First, in what way is canonical coarsening changed by having surface

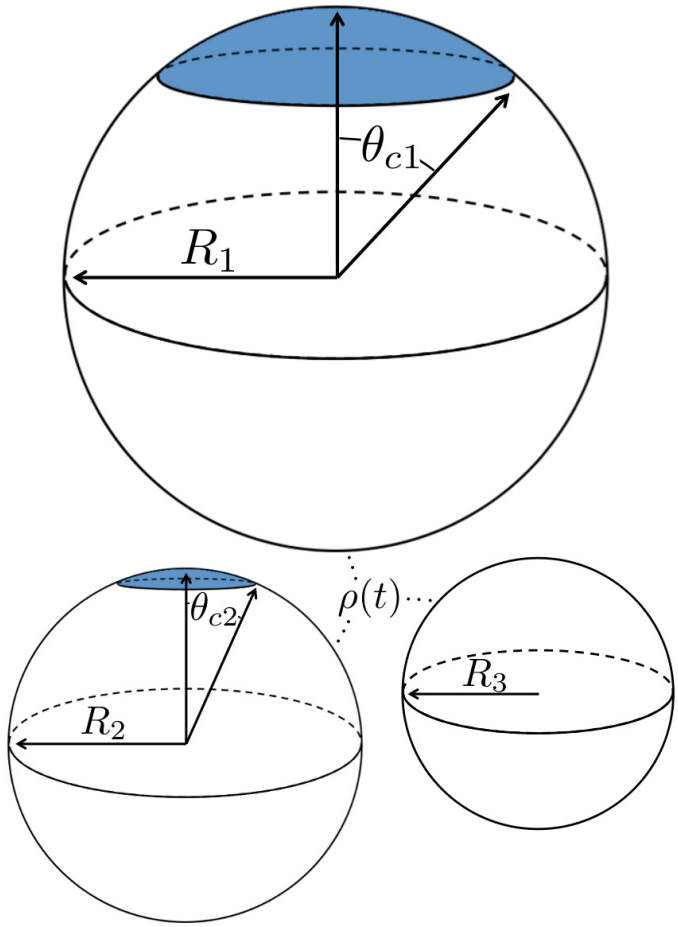

Figure 5.1: Illustration of our model geometry, not to scale, using three spherical drops. Drops 1 and 2 have clusters (symbolized by the circular blue cap) and drop 3 does not have a cluster. Drops may have different radii (R_i), and any clusters subtend a polar-angle θ_{ci}. Molecules on the surface of each drop exchange material with the bulk concentration $\rho(t)$.

clusters on drops rather than bulk clusters in space? Second, how do the details of drop polydispersity, i.e. the drop size distribution, affect coarsening behaviour? Third, what aspects of this system could affect biological behaviour — in particular autophagy selectivity? We aim to understand the physical behaviour of idealized coarsening clusters on drops, and identify how the qualitative characteristics of this process could play a role in protein cluster selection of substrates for autophagy.

5.2 Model

The growth and evaporation of coarsening clusters on drops will be determined by the vapour phase surrounding the clusters on the drop surface. Accordingly, we first consider the dynamics of a dilute concentration field of molecules, $f(\theta, \phi, t)$, on the surface of a single spherical drop of radius R, coupled to the bulk by association and dissociation from the drop surface:

$$\frac{\partial f}{\partial t} = D_s \nabla^2 f + \frac{\rho(t) D_b}{R} - \frac{\Gamma_{off}}{R} f. \tag{5.1}$$

The first term on the right is surface diffusion, with diffusivity D_s. The second term is diffusion-limited molecule association with the surface, proportional to a time-dependent bulk molecule concentration ρ and the bulk diffusivity D_b, and inversely proportional to the drop radius R due to diffusion-limited association [117]. Note that the total diffusive flux of molecules associating with the entire sphere surface is thus $4\pi\rho(t)D_bR$. The third term is molecule dissociation from the surface, proportional to the parameter Γ_{off} and molecule concentration f, and inversely proportional to the drop radius R — see Appendix A for development of this term. In steady state ($\partial f/\partial t = 0$), a uniform surface density is then independent of drop radius, with $f_{ss} = \rho(t)D_b/\Gamma_{off}$.

The molecule flux to the perimeter of a circular cluster of molecules on the sphere surface will be determined by the concentration field. There will not be a cluster on all spheres at all times since below a critical surface concentration clusters will be unstable to evaporation. Above this threshold concentration, clusters will nucleate and grow. Clusters in small biological systems, such as holin domains in bacteria [127, 172] and polarity clusters in yeast [129], often nucleate and coalesce rapidly. Similarly, we assume that nucleated clusters have resolved into (at most) a single circular cluster per drop.

To determine the growth of a cluster of N particles subtending a polar angle θ_c on a spherical drop of radius R (see Figure 5.1), the concentration field f must be found. In steady state, Eqn. 5.1 can be rewritten as a general Legendre equation and solved [173, 174]. (This solution, and subsequent development are shown in more detail in Appendix B.) We apply the Gibbs-Thomson boundary condition at the perimeter of the circular cluster, at θ_c, $f(\theta)|_{\theta=\pi-\theta_c} = f_\infty \left(1 + \frac{\nu}{R\sin\theta_c}\right)$, with f_∞

the concentration at a flat interface and ν the capillary length, which determines the decay length of the number density at the edge of the cluster and that we assume to be small [110, 175, 114, 176]. This gives us $f(\theta) = CP_\lambda(\cos\theta) + D_b\rho/\Gamma_{off}$, with the limiting form of the hypergeometric function of index λ $P_\lambda(x) = \frac{\sin(\lambda\pi)}{\pi}[\ln(\frac{1+x}{2}) + \gamma + 2\psi(\lambda+1) + \pi\cot(\lambda\pi)]$ [174], γ the Euler-Mascheroni constant, ψ the digamma function, $\lambda = -\frac{1}{2} \pm \frac{1}{2}\sqrt{1-4a}$, and $a \equiv \Gamma_{off}R/D_s$. The coefficient C is given by

$$C \equiv \frac{f_\infty(1+\nu/(R\sin\theta_c)) - D_b\rho/\Gamma_{off}}{(\sin(\lambda\pi)/\pi)\left[\log(\frac{1}{2} - \frac{1}{2}\cos\theta_c) + \gamma + 2\psi(\lambda+1) + \pi\cot(\lambda\pi)\right]}. \tag{5.2}$$

Mass balance with the diffusive flux of molecules to the cluster edge then determines the change in cluster size with time:

$$\frac{d\theta_c}{dt} = \frac{CD_s b\sin(\lambda\pi)}{\pi R^2}\frac{\sin\theta_c}{1-\cos\theta_c}, \tag{5.3}$$

where b is the area per molecule in a surface cluster.

The denominator of C has a logarithmic term, as seen in two-dimensional coarsening [115, 110, 108]. For fast diffusive equilibration compared to molecule number equilibration, $a = \Gamma_{off}R/D_s \ll 1$, and a small cluster $\theta_c \ll 1$, the denominator of C is dominated by the $\cot(\lambda\pi) \simeq \cot(-a\pi) \simeq -1/a$ term. Using this approximation, dependence on the surface diffusivity D_s is cancelled, and we can express the result in terms of the number of molecules N in the cluster for small θ_c,

$$\frac{dN}{dt} \simeq 4\pi R\left(D_b\rho(t) - f_\infty\Gamma_{off}\left(1+\nu\sqrt{\frac{\pi}{bN}}\right)\right). \tag{5.4}$$

This is similar in form to typical $d = 3$ descriptions of cluster dynamics [108, 110].

We investigate ensembles of many drops using two qualitatively-distinct radius distributions $P_0(R)$ with the same mean $\overline{R}$: one with and the other without a continuous tail. A uniform distribution has no tail, with $R \in [\overline{R} - R_0,\ \overline{R} + R_0]$, and $P_0(R) = 1/(2R_0)$. The exponential distribution has a tail, with $R \in [R_{min}, \infty)$, $P_0(R) = R_0^{-1}e^{-(R-R_{min})/R_0}$, and $R_{min} = \overline{R} - R_0$. We choose $\overline{R} = 0.25\mu$m to be consistent with peroxisome sizes [177].

To obtain a simplified dynamical equation for number of particles N_i in the cluster on the ith drop, we define $\alpha \equiv 4\pi D_b/\overline{R}^2$, a corresponding dimensionless time $t' \equiv \alpha t$, the bulk density corresponding to surface saturation $\rho_c \equiv f_\infty\Gamma_{off}/D_b$, and the

corresponding bulk supersaturation $\Delta\rho \equiv \rho(t) - \rho_c$, so that

$$\frac{dN_i(t')}{dt'} = \overline{R}^2 R_i \left[\Delta\rho - \frac{\beta}{\sqrt{N}}\right], \tag{5.5}$$

where we also conserve molecular numbers, so that $d\Delta\rho/dt' = -\langle dN_i/dt'\rangle/L^3$ where L^3 is the bulk cellular volume per drop. The parameter $\beta \equiv \sqrt{\pi}\Gamma_{off} f_\infty \nu/(D_b\sqrt{b})$ characterizes the effect of cluster curvature through the supersaturation necessary to avoid evaporation of finite-size surface clusters.

What is the expected scale of β? Capillary lengths of approximately one [114] and several [176] particle widths have been found for $2d$ and $3d$ systems, respectively. Assuming that the capillary length is approximately the size of a cluster molecule, $\nu/\sqrt{b} \simeq 1$, then $\beta \simeq \sqrt{\pi}\Gamma_{off} f_\infty/D_b$. A typical cytosolic protein diffusivity [177] is $D_b \simeq 1\mu\text{m}^2/\text{s}$, and an approximate lower-bound for f_∞ is determined by a single molecule per sphere, i.e. $f_\infty \gtrsim 1/(4\pi\overline{R}^2) \simeq 1\mu\text{m}^{-2}$. The timescale for number equilibration on the drop surface is $\overline{R}/\Gamma_{off}$. We choose as our default value $\beta = 0.01\mu\text{m}^{-3}$, corresponding to equilibration in tens of seconds, and explore the effects of varying β below. We note that for a typical cellular volume $V = 5000\mu\text{m}^3$, this choice of β corresponds to supersaturation by only 50 cytosolic molecules. Larger capillary lengths, $\nu/\sqrt{b} > 1$, require larger surface number equilibration times to achieve the same β.

To get better statistics, 10^7 drops are used for each simulation, all of which initially have clusters, and results are also averaged over 100 sets of initial conditions, unless otherwise stated. The initial supersaturation $\Delta\rho(0) = \Delta\rho_0$, and cluster sizes are initially proportional to their drop surface area, $N_i(0) = N_0(R_i/\overline{R})^2$. Other initial conditions, such as equal cluster sizes or cluster sizes randomly drawn from a uniform distribution, give qualitatively similar results at late times. Unless otherwise stated, $\Delta\rho_0 = 0.1\mu\text{m}^{-3}$, and $N_0 = 50$ — variation of these parameters is explored below. Our bulk volume is $L^3 = 100\mu\text{m}^3$ per drop, so that the initial available bulk number of molecules is $\Delta\rho_0 L^3 = 10$ per drop. For stable numerical results at early times timesteps must be small, but can be larger at later times [178]. We use a timestep $\Delta t' = 10(10t')^{1/3}$ until $\Delta t' = 10^5$, after which $\Delta t'$ is held constant.

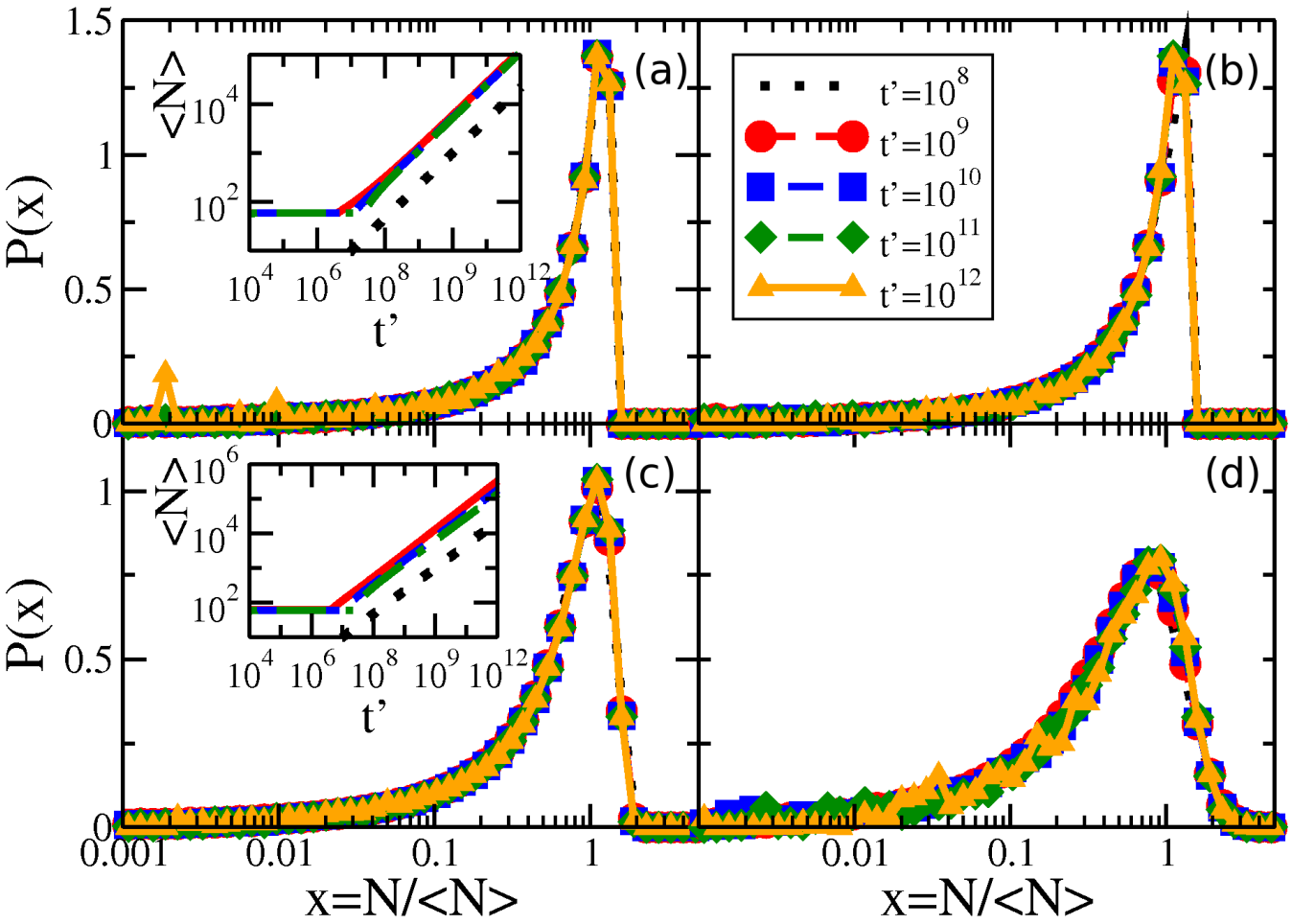

Figure 5.2: Scaling of the cluster size distribution for the times indicated by the legend in panel (b): (a) linear-log plot of $P(N/\langle N\rangle)$ vs. $N/\langle N\rangle$ for a narrow uniform drop radius distribution with $R_0 = 0.001\mu$m, (b) wide uniform drop radius distribution with $R_0 = 0.05\mu$m, (c) narrow exponential drop radius distribution with $R_0 = 0.001\mu$m, and (d) wide exponential drop radius distribution with $R_0 = 0.05\mu$m. Inset of (a) shows the average cluster size in time for uniform drop radius distributions with $R_0 = 0.05\mu$m (solid red line), $R_0 = 0.01\mu$m (dashed blue), and $R_0 = 0.001\mu$m (dashed-dotted green), along with the expected $t^{2/3}$ growth law indicated by the dotted black line. Inset of (c) is similar, with exponential drop radius distributions with $R_0 = 0.05\mu$m (solid red line), $R_0 = 0.01\mu$m (dashed blue), and $R_0 = 0.001\mu$m (dashed-dotted green).

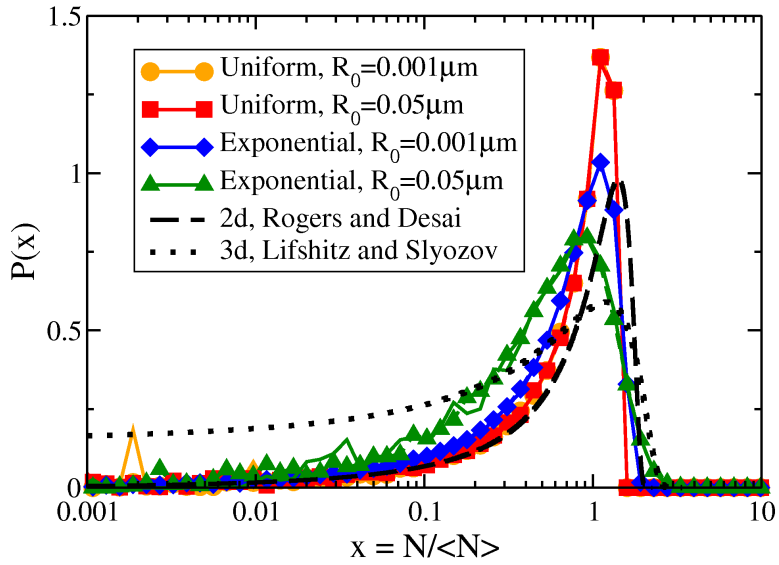

Figure 5.3: Non-universal cluster size distributions. Linear-log plot of cluster-size distributions $P(N/\langle N\rangle)$ vs. $N/\langle N\rangle$ for several drop radius distributions as indicated in the legend. Two times, $t' = 10^{11}$ and 10^{12}, are shown overlapping for each condition with dashed and solid coloured lines, respectively. Although each drop radius distribution exhibits scaling collapse, the different types of drop radius distributions do not collapse to the same scaling function. All uniform sphere radius distributions collapse to the same scaling function, while the exponential sphere radius distributions collapse to functions that vary with the drop distribution width. The black lines show analytic scaling distributions from the literature [115, 111] for $d = 2$ and $d = 3$, both in the dilute limit.

5.3 Results

The critical cluster size $r_c(t)$ is an important quantity for LSW coarsening — we measure the average number of molecules in a cluster, $\langle N\rangle$, where $\langle N\rangle \sim r_c^2$. By numerically evolving Eqn. 5.5 we confirmed that the average cluster size follows the LSW [111, 108] power-law $\langle N\rangle \sim t^{2/3}$ at later times, as shown in the insets of Figs. 5.2(a) and (c). Fig. 5.2 shows the cluster size distributions for uniform and exponential drop radius distributions. The cluster size distributions exhibit good dynamical scaling for at least three decades in time. The power-law growth and scaling was seen for all tested initial conditions, as well as for a range of two decades variation of β, the initial bulk supersaturation $\Delta\rho_0$, and the initial cluster size N_0 values.

However, Fig. 5.3 illustrates how the scaling function depends on the type of drop radius distribution. The scaled distribution is distinctly different for uniform

vs. exponential drop radius distributions. For the uniform drop radius distribution, there is no dependence on the distribution width parameter, R_0. For the exponential drop radius distribution, the scaled cluster size distributions depend on the width parameter R_0, becoming sharper as R_0 decreases. We also show two analytic solutions for scaling distributions of bulk clusters in $2d$ (dashed black line) [115] and $3d$ (dotted black line) [111]. The scaling distributions for clusters on drops are qualitatively similar to the $2d$ distribution, rapidly approaching zero as the cluster size $N \to 0$. Near the peak, the effect on the scaling function of changing the form of the drop size distribution is similar in magnitude to the effect of changing the spatial dimension between $2d$ and $3d$ for bulk coarsening.

At later times only the larger drops retain clusters — a phenomenon we call size-mediated cluster selectivity. Figs. 5.4 (a) and (b) show the radius of the smallest drop with a cluster, R_{min}. With increasing times, R_{min} suddenly increases at a characteristic onset time. This t_{onset} coincides with the beginning of the power-law coarsening regime shown in the insets of Fig. 5.2, after which dynamical scaling collapse of cluster size distributions is observed. Further, by considering the size distribution of drops that retain clusters, as shown in Fig. 5.5, we see that the smallest of the drops still retaining clusters are always next to lose their clusters. The distribution of larger drops with clusters remains unchanged, indicating larger drops do not lose their clusters until all smaller drops have done so.

As seen in Fig. 5.4(c), the timing of t_{onset} is controlled by β, $\Delta\rho_0$, N_0, and R_0. Both $\Delta\rho_0$ and N_0 would be directly affected by protein expression rates: $\Delta\rho_0$ is related to the initial bulk concentration of proteins, and represents how much protein remains in the bulk once clusters have nucleated on drops, while N_0 represents the number of proteins initially present in each cluster. While β, which is proportional to how quickly a protein dissociates from a membrane, may not be easily controlled, we do expect it to vary *in vivo* due to changes in membrane lipid composition [179, 180], such as between organelles. The width of the drop size distribution, R_0, is related to the amount and magnitude of organelle size variation, which could vary with conditions or cell type. We note that changing the initial cluster size distribution, so that instead of clusters proportional to drop area we used either initially equal or initially random cluster sizes from a uniform distribution, delayed t_{onset}.

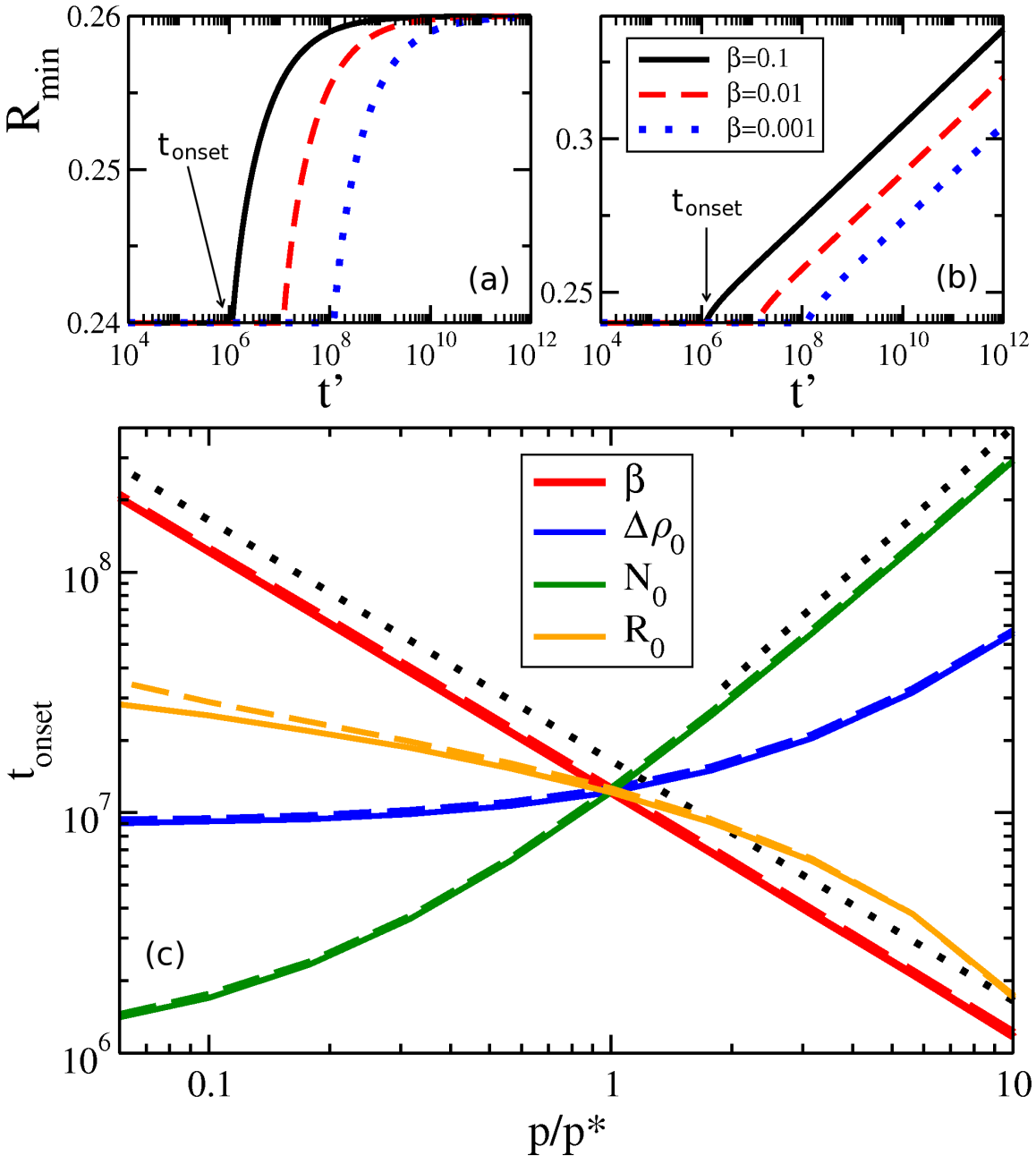

Figure 5.4: Minimum drop size with clusters R_{min} vs. time t' for (a) uniform and (b) exponential drop size distributions. In (a) and (b) we vary β as shown and hold other parameters at default values. The abrupt increase of R_{min} defines a time t_{onset}, shown by arrows for the $\beta = 0.1\mu\text{m}^{-3}$ curves. In (c), t_{onset} is shown as various parameters p [where p equals each of β (thicker, red), initial bulk supersaturation $\Delta\rho_0$ (darker, blue), initial cluster size N_0 (green), or drop-size distribution width R_0 (orange)] are varied with respect to their default values p^*. We use $p^* = 0.01\mu\text{m}^{-3}$, $0.1\mu\text{m}^{-3}$, 50, and $0.01\mu\text{m}$ for β, $\Delta\rho_0$, N_0, and R_0, respectively, and average over 10 sets of random initial conditions. Solid and dashed curves show results for uniform and exponential drop size distributions, respectively. The black dotted lines indicate expected asymptotic power law behaviour with exponents -1 and 1.5, following the β or N_0 data, respectively.

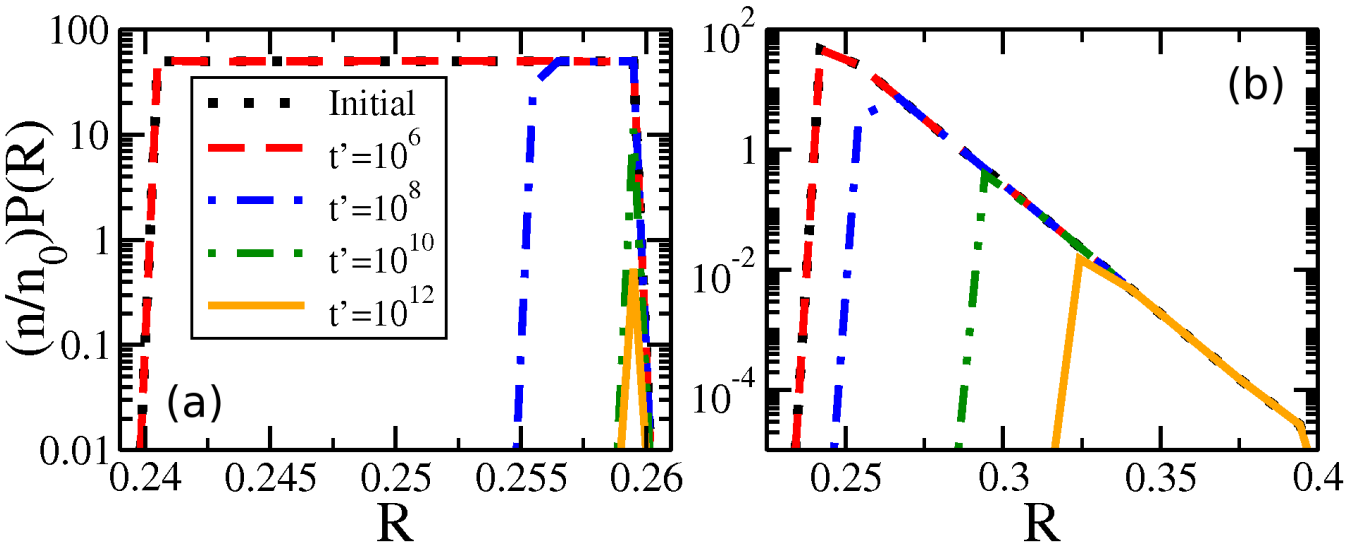

Figure 5.5: Number density of drop radii with clusters remaining, $(n/n_0)P(R)$, vs R for (a) uniform drop radius distribution with $R_0 = 0.01\mu$m and (b) exponential drop radius distribution with $R_0 = 0.01\mu$m. The times indicated by the legend in (a) apply to both panels, and the default parameters are used in both cases. We note that n is the number of spheres with clusters remaining, n_0 the initial number, and $P(R)$ is the drop size distribution.

We can qualitatively understand some of the asymptotic behavior shown in Fig. 5.4(c). For example, $t_{onset} \sim 1/\beta$ reflects the β dependence of the evaporative term in Eqn. 5.5 – indicating that cluster evaporation largely determines t_{onset}. Consistent with this, at larger values of N_0 we see that $t_{onset} \sim N_0^{1.5}$. The cluster size-dependent term in Eqn. 5.5 is $dN/dt \sim -N^{-0.5}$, which gives an evaporation time $\sim N_0^{1.5}$ for a cluster of initial size N_0. The dependence on the initial bulk density $\Delta\rho_0$ is similar to N_0. At smaller values of $\Delta\rho_0$ (at fixed N_0) we see that t_{onset} approaches a constant value. This occurs when the material in the initial clusters dominates the bulk density, and a similar cross-over is seen with smaller values of N_0 at fixed $\Delta\rho_0$. Increasing R_0 decreases t_{onset}, as drop size differences drive the the migration of material.

5.4 Discussion

Coarsening of clusters on drops exhibits LSW-like power law cluster growth [108] and dynamic scaling, as shown in Fig. 5.2. Scaling distributions typically depend on both spatial dimension and volume fraction [108], but are also known to depend on some

aspects of the evolution equations such as spatial anisotropy [181]. In this paper we have shown that the scaling cluster-size distribution depends on the shape of the drop radius distribution, and can also depend on its width. Distinct distributions are seen with uniform vs. exponential drop-size distributions. We expect that drop-size distributions with compact support (e.g. the uniform distribution) will have the same cluster size scaling functions as the uniform distribution, while drop-size distributions with tails (e.g. power laws) may have scaling functions that vary with the drop-size distribution width. Power law growth, scaling collapse, and similar t_{onset} behaviour are seen for both the uniform distribution, which has no tail at large drop sizes, and the exponential distribution, which does have a tail. At late times the remaining clusters are on large drops. Given the similarity of behaviour between uniform and exponential drop-size distributions, we expect similar behaviour independent of the details of the distribution. Both peroxisome [182, 183] and vesicle [184] size distributions are qualitatively similar to our exponential distribution, with a continuously decreasing tail at large sizes.

We have demonstrated that at later times larger drops are selected to retain clusters, while smaller drops have no clusters. The start of size-based selectivity is sudden, and described by the time t_{onset} that approximately coincides with the onset of dynamical scaling in these systems. Once selectivity has begun, and as coarsening progresses, the clusters on the smallest occupied drops progressively evaporate while clusters on larger drops will grow.

The autophagy receptor protein NBR1 is able to both self-interact and bind to membranes, and is a receptor protein for peroxisome autophagy, i.e. pexophagy [19]. In line with our results, we propose that NBR1 clusters on small peroxisomes will evaporate, while those on larger peroxisomes will grow. As NBR1 clusters on small peroxisomes shrink and evaporate, and those on larger peroxisomes grow, the NBR1 cluster growth on larger peroxisomes would push these peroxisomes over any threshold number of NBR1 for autophagy [19]. This would be a physical mechanism leading to the selective degradation of larger organelles by autophagy, on the basis of size.

Our proposed mechanism of size-selection through receptor cluster coarsening is consistent with the observation of receptor protein clusters [9, 10]. It is also consistent with the observation by Deosaran *et al.* [19] who show (see Fig. 5) significant

colocalization of NBR1 and peroxisomes (indicated by catalase), but with an all-or-none character. Catalase spots either colocalize with significant amounts of NBR1 or background levels. Indeed, our model shows that significantly higher NBR1 levels on drops with clusters than without – and only some drops supporting clusters at later times. Finally, our mechanism could also explain the observation that, in situations inducing a reduction in peroxisome number, larger peroxisomes degrade earlier and preferentially relative to smaller peroxisomes [171]. Degradation also depends upon peroxisome size in yeast [85].

How does the timing of our cluster selectivity correspond to that of peroxisome autophagy? In Fig. 5.4, our default values of β, $\Delta\rho_0$, N_0, and R_0 result in $t_{onset} \sim 10^7$. Using $t = t'/\alpha$, $D_b = 1\mu\text{m}^2$ as a typical cytosolic diffusivity, so that $\alpha = 4\pi D_b/\overline{R}^2 \simeq 200\text{s}^{-1}$, the onset of cluster selectivity is as early as $t \sim 10^4 - 10^5$ seconds. This timescale is consistent with mammalian autophagy, which occurs in days [134, 84]. Individual variation of β and N_0, shown in Fig. 5.4(c), can push t_{onset} down to 10^6, and combined variation (data not shown) can push t_{onset} even earlier — these timescales are consistent with peroxisome autophagy in yeast, which occurs in hours [81, 82]. Therefore the segregation of clusters to larger organelles through coarsening, as proposed here, can be fast enough to play a significant role in the selective degradation of larger peroxisomes.

Fig. 5.4 shows how the parameters β, $\Delta\rho_0$, N_0, and R_0 can vary the timing of cluster selectivity, t_{onset}. Increasing either the initial bulk supersaturation $\Delta\rho_0$ or the initial cluster size parameter N_0, i.e. expressing more clustering proteins, has the counterintuitive effect of *delaying* size selectivity. This suggests that experimentally adjusting expression of receptor proteins such as NBR1 would have a significant effect on the speed of autophagy response, with moderately larger expression potentially delaying autophagy. A decreased off-rate of receptor (through Γ_{off} and hence β) also leads to delayed size-selectivity. Larger numbers or more tightly bound receptors both lead to slower size-selectivity for our physical coarsening mechanism, since it depends upon the loss of receptors from smaller clusters. Conversely, increasing variation in drop size, represented by R_0, leads to earlier size-selectivity.

We have explored a physical mechanism of size-selection exploiting cluster coarsening on drops. We were motivated by how this may provide a physical basis for

autophagy substrate selectivity in pexophagy. A similar cluster-coarsening mechanism may allow PEX11, a protein important to the division of peroxisomes that self-interacts and sticks to membranes [17], to target larger peroxisomes. Similarly, SNARE proteins are required to facilitate vesicle fusion [185] and are thought to form membrane clusters. A similar selective coarsening mechanism could thereby select larger vesicles for fusion. Nevertheless, we expect that *in vivo* other biological processes will also also be involved and could modify cluster formation or selectivity. For example, ubiquitin is thought to play a role in recruiting NBR1 to peroxisome membranes [19], and a low peroxisome ubiquitin level [177] or other signals or interactions may prevent NBR1 from forming clusters and selecting peroxisomes for autophagy. In addition, different types of autophagy receptors often interact [5, 6]. We have started with the properties of only one receptor, modelled after NBR1. Another receptor, p62, interacts with NBR1 [103] and enhances pexophagy [19]. It will be interesting to consider how interactions with p62 may modify the selectivity mechanism we have proposed here.

5.5 Conclusion

We model the coarsening behaviour of clusters of molecules on the surface of spherical drops. We determine the dynamical equation for cluster size and, using an ensemble of polydisperse drops, recover the Lifshitz-Slyozov-Wagner exponent for cluster growth and dynamical scaling. The cluster-size scaling function is found to depend on the drop-size distribution, which affects the scaling function to a similar degree as spatial dimension does in bulk systems. Among remaining clusters, evaporation occurs from smaller drops first, with clusters on larger drops growing. This selection of larger drops by clusters may be significant to the cell-biological process of autophagy. Autophagy receptor proteins are seen to cluster, and the receptor protein NBR1 is sufficient for peroxisome autophagy and has domains suggesting it clusters and associates with membranes. Our observation of the selection of larger drops by clusters suggests that clustering NBR1 proteins on peroxisome surfaces could similarly select larger peroxisomes for NBR1 clusters, thereby selecting these larger peroxisomes for degradation by autophagy. This presents a possible physical mechanism to explain reported size selection during peroxisome degradation by autophagy.

5.6 Appendix A

Equation 5.1 describes the change in molecule concentration f on the surface of a sphere of radius R due to diffusion-limited association of molecules from the bulk and dissociation of molecules from the sphere surface. The dissociation term is $-\Gamma_{off} f/R$, and is controlled by the Γ_{off} parameter.

Successful dissociation includes diffusive escape from the immediate surface. The probability of recapture [117] by an absorbing sphere of radius R for a diffusive molecule initially at radial distance r is $P_{\text{capture}} = R/r$. The probability of escape is then $P_{\text{escape}} = 1 - R/r$. A molecule initially immediately adjacent to the sphere surface will be at distance $r = R + b$ for a molecule of radius b, and for $b \ll R$,

$$P_{\text{escape}} = 1 - \frac{R}{R+b} = 1 - (1 + b/R)^{-1} \simeq 1 - (1 - b/R) = b/R. \tag{5.6}$$

We expect that isolated NBR1 molecules will locally unbind from the membrane at a constant rate, independent of the small membrane curvature. However effective escape will be controlled by Eqn. 5.6, since most molecules will immediately rebind. The overall dissociation rate will therefore be proportional to R^{-1}. All dependence on molecule radius, unbinding (and recapture) of anchoring domains such as the NBR1 'J' domain, and other factors will then be contained in the Γ_{off} parameter. Since diffusion limited association has the same R dependence, this results in an R independent surface concentration in steady state.

5.7 Appendix B

This appendix follows the development of dynamical equation for cluster size on a sphere, Eqn. 5.5, starting with equation 5.1

$$\frac{\partial f}{\partial t} = D_s \nabla^2 f + \frac{\rho(t) D_b}{R} - \frac{\Gamma_{off}}{R} f, \tag{5.7}$$

where f is the concentration field, D_s is the surface diffusivity, ρ is the bulk molecule concentration, D_b is the bulk diffusivity, Γ_{off} is the dissociation parameter, and R is the sphere radius. We transform to $\tilde{f} = f - \rho D_b/\Gamma_{off}$, define $\tilde{a} = \Gamma_{off}/R$, go to steady state ($\partial f/\partial t = 0$), and only keep the θ dependence of the Laplacian due to

assumed azimuthal symmetry for a polar cluster:

$$\tilde{a}\tilde{f} = D_s \nabla^2 \tilde{f} = \frac{D}{R^2 \sin\theta} \frac{\partial}{\partial\theta} \left(\sin\theta \frac{\partial \tilde{f}}{\partial\theta} \right). \tag{5.8}$$

We now set $x = \cos\theta$ and $a = \tilde{a}R^2/D_s$ to give us

$$(1-x^2)\frac{\partial^2 \tilde{f}}{\partial x^2} - 2x\frac{\partial \tilde{f}}{\partial x} - a\tilde{f} = 0, \tag{5.9}$$

which is a hypergeometric differential equation [173]. Only f near the polar cluster is needed to determine cluster dynamics, and so we use the limiting form[174] of the solution as $x \to -1$, or equivalently as $\theta \to \pi$

$$P_\lambda(x) = \frac{\sin(\lambda\pi)}{\pi} \left[\ln\left(\frac{1+x}{2}\right) + \gamma + 2\psi(\lambda+1) + \pi\cot(\lambda\pi) \right], \tag{5.10}$$

where $\lambda = -\frac{1}{2} \pm \frac{1}{2}\sqrt{1-4a}$, γ is the Euler-Mascheroni constant, and ψ is the digamma function. So our solution for $\tilde{f}$ is then $\tilde{f} = CP_\lambda(\cos\theta)$, or

$$f = CP_\lambda(\cos\theta) + \rho D_b/\Gamma_{off}. \tag{5.11}$$

The Gibbs-Thomson boundary condition [110, 175, 114, 176] determines the elevated vapour pressure in equilibrium with a curved interface. We apply this condition at the perimeter of our circular cluster on the pole of the sphere, which covers an angle θ_c from the pole:

$$f(\theta)|_{\theta=\pi-\theta_c} = f_\infty \left(1 + \frac{\nu}{R\sin\theta_c}\right). \tag{5.12}$$

Applying this condition to Eqn. 5.11 gives

$$C \equiv \frac{f_\infty(1+\nu/(R\sin\theta_c)) - D_b\rho/\Gamma_{off}}{(\sin(\lambda\pi)/\pi)\left[\log(\frac{1}{2} - \frac{1}{2}\cos\theta_c) + \gamma + 2\psi(\lambda+1) + \pi\cot(\lambda\pi)\right]}, \tag{5.13}$$

where the Euler-Mascheroni constant $\gamma \simeq 0.577$.

Now we apply mass balance, determining the change in cluster area by the diffusive flux of molecules to the cluster perimeter:

$$\frac{d}{dt}\left[2\pi R^2(1-\cos\theta_c)\right] = \left[2\pi R\sin\theta_c D_s \frac{\partial f}{\partial(-R\theta)}_{\theta=\pi-\theta_c}\right] b, \tag{5.14}$$

where b is the area per molecule. Inserting Eqn. 5.12 into Eqn. 5.14 gives

$$\frac{d\theta_c}{dt} = \frac{CD_s b\sin(\lambda\pi)}{\pi R^2} \frac{\sin\theta_c}{1-\cos\theta_c}. \tag{5.15}$$

For $\theta_c \ll 1$ we have $\sin\theta_c \simeq \theta_c$, and $\cos\theta_c \simeq 1 - \theta_c^2/2$. Putting these into the expression for C gives us

$$\frac{d\theta_c}{dt} = \frac{2D_s b\left[D_b\rho/\Gamma_{off} - f_\infty(1+\nu/(R\theta_c))\right]}{R^2\theta_c\left[\log(\theta_c^2/4) + \gamma + 2\psi(\lambda+1) + \pi\cot(\lambda\pi)\right]}. \tag{5.16}$$

The denominator of the right side of this equation has four terms, with the relative size determined by $\theta_c \ll 1$, and $a \ll 1$, which leads to $\lambda \simeq -a$. For the digamma function, $\psi(\lambda+1) \simeq \psi(-a+1) \simeq \psi(1) = -\gamma$, while $\cot(\lambda\pi) \simeq \cot(-a\pi) \simeq -1/(a\pi)$. We assume that $|\ln(\theta_c^2/4)| \ll 1/a$, which is equivalent to $\theta_c^2 \gg e^{-1/a}$, which is expected to be the case for $a \ll 1$. This implies that $\pi\cot(\lambda\pi) \simeq -1/a$ is the dominant term of the denominator, and that

$$\frac{d\theta_c}{dt} \simeq \frac{2D_s ba\left[D_b\rho/\Gamma_{off} - f_\infty(1+\nu/(R\theta_c))\right]}{R^2\theta_c} = \frac{2b\Gamma_{off}\left[D_b\rho/\Gamma_{off} - f_\infty(1+\nu/(R\theta_c))\right]}{R\theta_c}. \tag{5.17}$$

Assuming θ_c is small, $bN = \pi(R\theta_c)^2$, we have $d\theta_c/dt = 1/(2R)\sqrt{b/(\pi N)}dN/dt$ and so

$$\frac{dN}{dt} = 4\pi R\left[D_b\rho - \Gamma_{off}f_\infty\left(1 + \frac{\nu}{R\theta_c}\right)\right]. \tag{5.18}$$

We define a mean sphere radius $\overline{R}$, $\alpha = 4\pi D_b/\overline{R}^2$, a dimensionless time $t' = \alpha t$, and bulk density corresponding to surface saturation $\rho_c = f_\infty\Gamma_{off}/D_b$, and a bulk supersaturation $\Delta\rho = \rho(t) - \rho_c$. This then gives us

$$\begin{aligned}
\frac{1}{(4\pi D_b/\overline{R}^2)}\frac{dN}{dt} &= R\overline{R}^2\left[\rho(t) - \frac{f_\infty\Gamma_{off}}{D_b} - \frac{\sqrt{\pi}\Gamma_{off}f_\infty\nu}{D_b\sqrt{b}}\frac{1}{\sqrt{N}}\right], \text{or} \\
\frac{dN}{dt'} &= R\overline{R}^2\left(\Delta\rho - \frac{\beta}{\sqrt{N}}\right).
\end{aligned} \tag{5.19}$$

Chapter 6

Modelling NBR1 and p62 Dynamics on Peroxisomes with Clustering

6.1 Introduction

Autophagy is an important system for the degradation of large cellular substrates [89], including protein aggregates, organelles, and pathogenic bacteria. During macroautophagy, referred to hereafter as autophagy, substrates are enveloped by an isolating membrane, forming an autophagosome, before being directed to fuse with a lysosome for degradation in a multi-stage process that requires receptor protein attachment [6, 100].

Autophagy was initially thought a non-selective process that randomly consumed regions of the cytosol, largely as a starvation response to obtain necessary resources [5]. More recently, autophagy has been shown to be capable of selective degradation of substrates [8], mediated by what are known as autophagy receptor proteins [6]. Typically containing domains to interact with substrates as well as the proteins of the autophagy system, autophagy receptor proteins interface between substrates and the proteins of the autophagy system [89]. Different receptor proteins and their combinations are thought to select distinct substrate types, e.g. peroxisomes vs. mitochondria, from among the many subcellular targets [6].

We investigate the behaviour of the receptor proteins p62 and NBR1 on one of their autophagy substrates, the peroxisome. Peroxisomes are dynamic organelles with functions including the metabolism of hydrogen peroxide and the oxidation of fatty acids [14]. Peroxisomes are usually spherical [11] with diameter ranging from $\sim 0.1 - 0.8\mu$m, and there can be hundreds in a single mammalian cell [13]. In both mammals and yeast significant peroxisome degradation is through macroautophagy, known as pexophagy [84, 86]. Peroxisome degradation has been observed to begin with large peroxisomes following a change in growth medium [171], and larger peroxisomes can

require more autophagy-related proteins to facilitate degradation [85].

By modelling the behaviour of pexophagy receptor proteins, we aim to address what has been described [80] as a 'burning question' in understanding pexophagy: how are some peroxisomes recognized by the autophagic machinery, while the others are not? The answer could lie with receptor protein domains, which have been observed on the surface of bacteria targeted for autophagy [9, 10, 105]. The membrane-anchoring and self-interaction regions of NBR1 [19] suggest that NBR1 may cluster on the surface of peroxisomes. Our previous work [186] modelled the dynamics of clusters on a polydisperse ensemble of spherical drops. We found that the pre-existing clusters grew on larger drops, and evaporated from small drops. The selection of larger drops for cluster growth suggests that clusters of NBR1 on peroxisomes could select larger peroxisomes for degradation by autophagy, consistent with earlier degradation of larger peroxisomes [171] and dependence of degradation mode on peroxisome size in yeast [85].

In this paper we build on our previous work [186] to further understand the selection of large peroxisomes by NBR1 clusters. In addition to dynamics of existing NBR1 clusters, our model now includes both cluster formation and p62 dynamics. Ubiquitin levels are also explicitly included, as ubiquitin labelling of peroxisomes induces significant pexophagy [18], and ubiquitin levels may self-regulate to control pexophagy [177]. In addition to the selection of existing clusters on large peroxisomes for growth, the formation of clusters is also found to occur preferentially on larger peroxisomes.

We consider global signals for pexophagy vs. the degradation of individual peroxisomes. Peroxisome numbers can be increased in mammals with proliferators [133] and in yeast by a change in growth medium [81]. After these conditions are reversed, peroxisomes can be degraded in yeast in hours and in mammals in days [134, 84, 81, 82]. Peroxisomes are also thought to be degraded by autophagy when damaged [187, 188]. Degradation to reduce peroxisome numbers (deproliferation) may aim to remove peroxisomes with certain characteristics (e.g. size), or the least productive peroxisomes, with a limited response. Experimental evidence of size selection is limited to deproliferation, with degradation beginning with large peroxisomes [171] or degradation of larger peroxisomes requiring more autophagy-related proteins [85]. In contrast, an

effective response to damage may have little additional selectivity, so that a damage signal can take priority. To account for the possible differences between degradation in response to deproliferation or damage, we consider the two as separate cases. Fortunately, ubiquitin may signal for both peroxisome deproliferation and damage [177, 49]. Accordingly, we can raise the ubiquitin level for all peroxisomes for deproliferation, and on individual peroxisomes for damage, to investigate the response of our model receptor proteins.

Although NBR1 is necessary and sufficient for pexophagy, p62 also has an important role [19, 18], and p62 can act as an autophagy receptor protein for many substrates [6]. Knocking down p62 increases catalase fluorescence, indicating that peroxisomal volume has increased, an effect that has been taken as evidence of decreased pexophagy [19, 18]. Along with the inability of p62 alone to induce pexophagy [19], this knockdown effect makes p62 intriguing for pexophagy investigations.

6.2 Receptor Details and Model

We model the accumulation of NBR1 and p62 on the surface of peroxisomes, including clusters of NBR1. The peroxisomes are assumed to be well-separated [186] spherical [11] drops.

NBR1 is modelled to associate with the peroxisome surface using ubiquitin on the membrane as coincidence detectors [19]. Surface NBR1 of sufficiently high concentration are allowed to form clusters, and these clusters grow and shrink according to the peroxisome surface diffusion field. p62 is modelled to bind to both NBR1 and ubiquitin on the peroxisome surface, forming chains. NBR1 can dissociate from the membrane independent of any p62 chain. p62 chains can dissociate from ubiquitin at the base of the chain. p62 chains on ubiquitin block NBR1 from using the particular ubiquitin to associate with the peroxisome membrane. p62 chains on NBR1 prevent NBR1 from participating in cluster formation or growth.

6.2.1 NBR1 Model

NBR1 is an autophagy receptor protein that is both necessary and sufficient for pexophagy [19]. NBR1 contains several regions that are essential to its role as an autophagy receptor protein. The LC3-interacting region (LIR) interacts with the

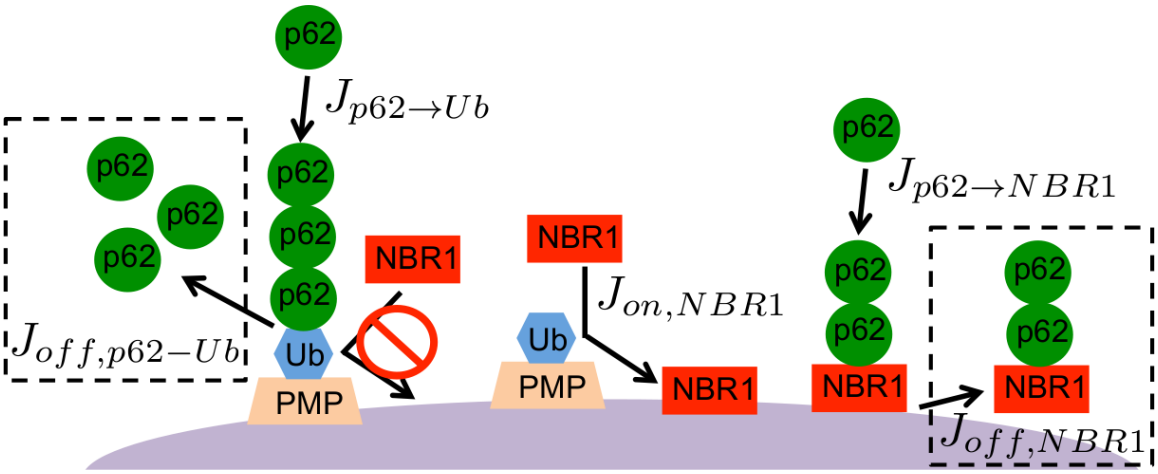

Figure 6.1: NBR1 can associate with the peroxisome surface at a rate $J_{on,NBR1}$ using diffusion-limited arrival to bare ubiquitin — ubiquitin (Ub) with p62 chains cannot facilitate NBR1 association. p62 begin a chain or join an existing chain on ubiquitin with a rate $J_{p62\to Ub}$ or NBR1 with a rate $J_{p62\to NBR1}$. NBR1, with and without p62 chains, dissociates from the peroxisomes surface at a rate $J_{off,NBR1}$. p62 chains dissociate from ubiquitin at the base of the chain at a rate $J_{off,p62-Ub}$. The dissociation rates are shown in dashed boxes. Ubiquitin associates with the peroxisome surface by binding a peroxisome membrane protein (PMP). All the processes in this diagram are quantitatively described in sections 6.2.1, 6.2.2, and 6.2.3.

proteins of the autophagy system [100, 101]. The UBA region can bind to ubiquitin [100, 102], and allows attachment to ubiquitin-tagged substrates [8]. The Phox and Bem1p (PB1) region can bind PB1 domains on other proteins [103], as well as coiled-coil regions for self-interaction [19]. The distinctive 'J' region allows NBR1 to anchor to membranes.

NBR1 is recruited to the peroxisome surface by binding to ubiquitin with its UBA domain, and then transitions to binding to the membrane using the 'J' domain [19]. We assume that the arrival of NBR1 to ubiquitin sites is diffusion-limited — the diffusion-limited rates to circular targets on a sphere are developed in Appendix A, with equation 6.29 describing the diffusion-limited arrival rate to i different target sizes each numbering N_i. For NBR1 there is only one target type [117], ubiquitin, and so $i = 1$. The arrival rate of NBR1 to the surface of a peroxisome is then

$$J_{on,NBR1} = \frac{4\pi D_{NBR1}\rho_{NBR1}s_{Ub}}{N_{Ub}(0)s_{Ub} + \pi R} R N_{Ub}(0), \tag{6.1}$$

with $D_{NBR1} = D$ the bulk NBR1 diffusivity, $\rho_{NBR1} = c_\infty$ the bulk NBR1 concentration, $R = a$ the peroxisome radius, $N_{Ub}(0) = N$ the number of target ubiquitin with

no p62 chain on the peroxisome, and $s_{Ub} = s$ the ubiquitin radius, or target size, corresponding to the quantities in equation 6.29. Diffusion-limited association to NBR1 only includes ubiquitin with no p62 chain because it is assumed the UBA domain of NBR1 cannot bind ubiquitin while the ubiquitin is bound by the UBA domain of p62. NBR1 with a p62 chain of length l dissociates from the peroxisome surface at a rate $J_{off,NBR1}(l) = (\Gamma_{off,NBR1}/R)N_{NBR1}(l)$, where $\Gamma_{off,NBR1}$ is the dissociation parameter for NBR1 from the membrane, and $N_{NBR1}(l)$ is the number of NBR1 on the peroxisome surface with a p62 chain of length l. See Appendix A of Brown and Rutenberg [186] for motivation of the R^{-1} dependence of this dissociation rate. The association and dissociation of NBR1 with the peroxisome surface is schematically shown in Figure 6.1.

NBR1 is modelled to form clusters at sufficiently high surface concentration on peroxisomes. Section 6.2.4 below describes our model for NBR1 cluster formation and growth.

6.2.2 p62 Model

p62 was the first mammalian autophagy receptor protein to be identified [98, 99, 6] and participates in the selection of various substrates for degradation by autophagy [6], including pexophagy [18, 19]. Important p62 regions for autophagy are LIR, UBA region, and PB1 region, which it shares with NBR1 [100, 101, 8, 103]. Significantly, the PB1 region of p62 can bind other PB1 domains on both sides, forming chains, unlike NBR1 which can only bind on one side [103].

We assume that the arrival of p62 to both NBR1 and ubiquitin targets is diffusion limited. Equation 6.29 describes the diffusion-limited arrival to i different target sizes, each numbering N_i. For p62 there are therefore two target types, NBR1 and ubiquitin, so $i = 2$. The arrival rate of p62 to NBR1 on the surface of the peroxisome, both to begin a chain ($l = 0$) and to add to an existing chain of length l, is

$$J_{p62\to NBR1}(l) = \frac{4\pi D_{p62}\rho_{p62}s_{NBR1}}{N_{NBR1}s_{NBR1} + N_{Ub}s_{Ub} + \pi R} R N_{NBR1}(l), \tag{6.2}$$

with D_{p62} the bulk p62 diffusivity, ρ_{p62} the bulk p62 concentration, s_{NBR1} the NBR1 radius, N_{NBR1} the total number of NBR1 on the peroxisome surface, and N_{Ub} the total number of ubiquitin. p62 chains on NBR1 only detach when the NBR1 base

dissociates from the membrane. The arrival rate of p62 to ubiquitin on the surface of the peroxisome, both to begin a chain ($l = 0$) and to add to an existing chain of length l, is

$$J_{p62\to Ub}(l) = \frac{4\pi D_{p62}\rho_{p62}s_{Ub}}{N_{NBR1}s_{NBR1} + N_{Ub}s_{Ub} + \pi R} R N_{Ub}(l). \tag{6.3}$$

The base p62 can dissociate from ubiquitin, detaching the entire chain, at a rate $J_{off,p62-Ub}(l) = \Gamma_{off,p62,Ub}N_{Ub}(l)$, where $\Gamma_{off,p62,Ub}$ is the dissociation parameter for p62 from ubiquitin. The growth and dissociation of p62 chains is schematically shown in Figure 6.1.

p62 is thought to form oligomeric chains due to double-sided binding of the PB1 region [103]. From polymer physics, it is well known that polymer brushes can lead to significant steric repulsion [189, 190]. Indeed, steric interactions of membrane associated proteins can induce membrane curvature [191, 192], oppose lipid phase separation [193], prevent growth of protein clusters [194], and can explain decreased diffusivities [195]. Accordingly, we investigate the hypothesis that steric interactions of p62 chains bound to NBR1 will inhibit NBR1 oligomerization. The cluster formation and growth model in section 6.2.4 does not allow NBR1 with p62 chains to participate in cluster formation or growth.

6.2.3 Discrete Kinetic Model of NBR1 and p62 Chains

Here we describe a non-normalized discrete kinetic model for the number of NBR1, NBR1 with variable p62 chain length, and ubiquitin with variable p62 chain length.

Bringing the rates for NBR1 and p62 arrival to NBR1 together determines the change in time of the number of NBR1 and ubiquitin with different p62 chain lengths. The change in time of the number of NBR1 with chain length l, $N(l)$, is

$$\frac{dN(l)}{dt} = J_{on,NBR1}\delta_{l,0} - J_{off,NBR1}(l) + (1-\delta_{l,0})J_{p62\to NBR1}(l-1) - J_{p62\to NBR1}(l) \tag{6.4}$$

The change in time of the number of ubiquitin with chain length l, $n_{Ub}(l)$, is

$$\frac{dN_{Ub}(l)}{dt} = [J_{p62\to Ub}(l-1) - J_{off,p62-Ub}(l)](1-\delta_{l,0}) - J_{p62\to Ub}(l) + \delta_{l,0}\sum_{i=1}^{\infty} J_{off,p62-Ub}(i) \tag{6.5}$$

Note that p62 chains grow by individual p62 units, and dissociate at the base by either NBR1 dissociating from the membrane or the first p62 in the chain dissociating

from ubiquitin. NBR1-p62 and p62-p62 bonds are through the PB1 region, which has a relatively high affinity in comparison to the p62-Ub UBA bond and the NBR1-membrane J region association [103, 196, 197, 107, 104]. In Appendix D we consider and show all results for a similar model, where p62 can also dissociate from the end of a chain, although there are no qualitative changes found in the results. Also note that NBR1 can only arrive at the membrane by using ubiquitin sites that have zero p62, because a p62 chain on the ubiquitin would block the interaction between the ubiquitin and the UBA region of NBR1. We assume that the total number of ubiquitin on a peroxisome is fixed at N_{Ub} and does not dynamically change — any changes in time are inserted by hand to evaluate the response of the system.

NBR1 significantly colocalizes with catalase and PMP70 (approximately 50%), a peroxisome matrix and membrane protein respectively, while p62 colocalization is much lower (approximately 10%) [19]. The significant colocalization of NBR1 with peroxisomes compared to p62 is consistent with the many roles of p62 for autophagy [6] and other pathways [198], while NBR1 seems to primarily participate in autophagy, although it does have other roles [199]. We expect that any significant uptake of NBR1 by peroxisomes will be the primary sink for any cytosolic NBR1, while uptake of p62 by peroxisomes will be subdominant. Therefore, in the model system the total number of NBR1 in the cytosol and on peroxisomes is conserved, while the cytosolic p62 concentration is held constant. For a system of N_P peroxisomes, the number of bulk NBR1, B_{NBR1}, is described by

$$\frac{dB_{NBR1}}{dt} = -\sum_{j=1}^{N_P}\sum_{l=0}^{\infty}\frac{dN_j(l)}{dt}. \tag{6.6}$$

6.2.4 Cluster Formation and Growth

As mentioned above, we hypothesize that an NBR1 molecule can participate in cluster formation or growth only if it does not have a p62 chain. In our model, rapid cluster formation occurs on the surface of a peroxisome lacking a cluster when there are sufficient cluster-forming molecules (NBR1 with no p62, $N_{NBR1}(0)$) to form a cluster and a surrounding equilibrium vapour. This occurs when the cluster-forming molecule

density σ on the drop surface reaches a threshold value

$$\sigma^* = f_\infty + 3\left(\frac{f_\infty \nu}{4\sqrt{b}R}\right)^{2/3}, \tag{6.7}$$

where f_∞ is the equilibrium vapour density at a flat interface, ν is the capillary length, b is the area per molecule, and R is the drop radius. The threshold concentration σ^* allows the formation of a cluster containing

$$N^*_{clust} = \pi R^{4/3}\left(\frac{2f_\infty \nu}{\sqrt{b}}\right)^{2/3} \tag{6.8}$$

molecules. These quantities are derived by conserving NBR1 before and after cluster formation, and requiring that there are sufficient molecules to generate both a cluster and a surrounding equilibrium vapour satisfying the Gibbs-Thomson equation [114] (see Appendix B).

Existing clusters grow and shrink according to

$$\frac{dN_{clust}}{dt} = 4\pi a R^2\left[w - f_\infty\left(1 + \nu\sqrt{\frac{\pi}{bN_{clust}}}\right)\right], \tag{6.9}$$

where

$$a = \frac{\Gamma_{off,NBR1}}{R} + \frac{4\pi D_{p62} s_{NBR1} R}{N_{tot} s_{NBR1} + N_{Ub} s_{Ub} + \pi R}, \tag{6.10}$$

$$w = \frac{1}{a}\left(\Gamma_{off,p62}\tilde{f}_1 + \frac{D_{NBR1}\rho_{NBR1} s_{Ub} N_{Ub}}{R(N_{Ub} s_{Ub} + \pi R)}\right), \tag{6.11}$$

and $\tilde{f}_1$ is the surface density of NBR1 with one p62. Equations 6.9-6.11 are derived by solving the diffusion equation on a sphere surface surrounding a cluster to determine the diffusive flux to the cluster edge, and applying mass balance to find the change of cluster size in time (see Appendix C).

6.2.5 Parameters, Initial Conditions, and Numerical Details

While detailed variation of parameter values is not expected to affect our results, we aim to estimate all parameters as accurately as possible. These parameters are not tuned or otherwise varied in our modelling.

The radius of a globular protein or protein complex can be approximated can be approximated by $R = 0.066M^{1/3}$ for R in nm and M in Daltons [157], and we use this radius to estimate the size of diffusive targets. For NBR1, with mass of

approximately 107 kDa [200, 201], $r_{NBR1} = 3.14$ nm. For ubiquitin, of mass 8 kDa [202, 203], $r_{Ub} = 1.32$ nm.

To approximate the diffusivity of NBR1 and p62 in the cytosol we note that the diffusion constant of EYFP in the cytosol has been measured at 0.75 ± 0.3 μm^2/s for NLFK cells and 1.83 ± 0.28 μm^2/s in HeLa cells [149]. We assume roughly spherical or globular proteins, and scale the diffusivity with inverse radius, and the radius with the cube root of the protein mass. Using $D_{YFP} = 1\mu$m^2/s with mass $M = 27$kDa, an NBR1 mass of 107 kDa gives $D_{NBR1} = 0.63\mu$m^2/s and a p62 mass of 62 kDa [99, 204] gives $D_{p62} = 0.83\mu$m^2/s.

We use $\Gamma_{off,NBR1} = 0.25\mu$m s^{-1} for the dissociation rate of NBR1 from the peroxisome membrane, so that for typical peroxisomes of radius $R = 0.25\mu$m the timescale of dissociation is 1s. We choose $\Gamma_{off,p62-Ub} = 1$s^{-1} for the dissociation rate of p62 from ubiquitin (interaction through the UBA domain [102, 205, 104]).

For clusters, we assume the capillary length ν is the size of a single NBR1 protein, so $\nu = r_{NBR1} = 3.14$ nm, and that the area per molecule is $b = \nu^2 = 9.86$ nm^2. This is consistent with capillary lengths of one [114] and several [176] particle widths for $2d$ and $3d$ systems, respectively. The vapour pressure f_∞ is taken to be 10μm^{-2} on the peroxisome membrane — for a typical peroxisome of radius $R = 0.25\mu$m, this is approximately a single molecule on the surface.

We use a system volume $V = N_p v$, where N_P is the number of peroxisomes, and $v = 10\mu$m^3 is the volume per peroxisome. 300 peroxisomes has been reported as an average number of for mammalian cells [20]. Therefore the volume inside a spherical cell of radius 10μm, divided among 300 peroxisomes, is 14 μm^3 or approximately 10μm^3 per peroxisome.

We address systems containing a single peroxisome or an ensemble of many peroxisomes. Within our model, systems of many peroxisomes have peroxisome radii distributed exponentially, as peroxisome size distributions [182, 183] are qualitatively similar to an exponential distribution. In ensemble systems, $P(R) \sim e^{-R/R_s}$, where $P(R)$ is the probability of a peroxisome of radius R, and $R_s = 0.1\mu$m. For most ensemble systems used in this paper we simply set the chosen radius R_c of the first peroxisome with $P_c = 0.01 = \int_{R_{min}}^{R_c} P(R)dR$, and the second radius with $P_c = 0.02$

and so on. For some results using a single ensemble of peroxisome radii leads to artifacts, and so for indicated results the peroxisome radii are chosen by sampling from the distribution $P(R)$. The number of ubiquitin on a peroxisome will be proportional to the surface area, $N_{Ub}(R) = n_0(R/R_0)^2$, with the ubiquitin coefficient n_0 typically 100, and $R_0 = 0.25\mu$m.

Initially, all peroxisomes surfaces have zero NBR1 and zero p62, with all NBR1 and p62 initially in the bulk cytosol surrounding the peroxisomes. As discussed above, NBR1 numbers are finite and conserved, while the cytosolic p62 concentration is held constant.

p62 is modelled to form chains on both NBR1 and ubiquitin. For reasons of computational efficiency we have limited p62 chain lengths to a maximum of $l = 10$. With this restriction we found no qualitative changes, and minimal quantitative changes, compared to considered longer maximum chain lengths.

6.3 Results

6.3.1 Systems with Clustering Forbidden

We first investigate systems without clustering, and track the sum of the number of NBR1 and p62 to find the total number of proteins that contain LIRs, which interact with the autophagy system. Figure 6.2(a) shows the equilibrated number of LIRs (one each from every p62 and NBR1) on a single peroxisome as the constant p62 concentration and initial NBR1 concentration are varied. The bulk NBR1 and p62 concentrations surrounding the peroxisome are varied between zero and $150\mu\text{m}^{-3}$. Higher NBR1 or p62 alone can increase the LIR numbers on the peroxisome, but combining high NBR1 and high p62 concentrations induces significantly higher LIR numbers.

Next, ensembles of 100 peroxisomes are considered, rather than a single peroxisome. The peroxisome radii are exponentially distributed along the approximate range of peroxisome sizes, from $R = 0.05\mu$m to 0.50μm. Figure 6.2(b) plots the LIR density on the surface of each peroxisome vs. peroxisome radius, for different initial NBR1 and constant p62 concentrations as indicated. The NBR1 and p62 concentrations are chosen so that the LIR densities are equal for the largest peroxisome

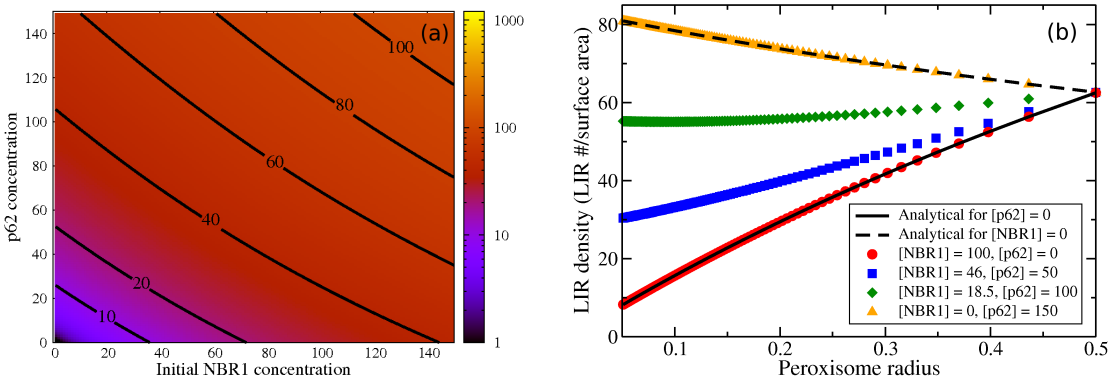

Figure 6.2: Equilibrated number of LIR-domain containing proteins with forbidden clustering. (a) System of one peroxisome, $R = 0.25\mu$m. Intensity plot shows the number of LIR-domain containing proteins, the sum of NBR1 and p62, on the peroxisome after equilibration. Initially there are zero NBR1 and p62 on the peroxisome, and the indicated initial NBR1 concentration in the bulk volume. The indicated p62 concentration is held constant. (b) System of 100 peroxisomes, with radii exponentially distributed between $R = 0.05\mu$m and $R = 0.50\mu$m. Initially there are zero NBR1 and p62 on the peroxisomes, and indicated NBR1 concentrations are the initial concentration in the surrounding bulk volume. p62 concentrations are held constant. LIR density is the number of LIR-domain containing proteins, NBR1 and p62, on a peroxisome, divided by the peroxisome surface area $4\pi R^2$. At each p62 concentration, the NBR1 concentration is varied to match the [p62] = 0 case at the maximum sphere radius. Equation 6.13 is plotted with the black solid line using $D\rho s n_0/\Gamma_{off} = 32.8\mu$m s^{-1}. $\langle L\rangle N_{occ}/(4\pi R^2)$, combining equations 6.16 and 6.17, is plotted with the dashed black line.

radius.

For zero p62, the LIR density is found to increase with peroxisome radius. We can obtain this result analytically by considering the dynamics of NBR1 on a peroxisome. The change in time of the number N_{NBR1} of NBR1 on a peroxisome when the p62 concentration is zero is found by combining $J_{on,NBR1}$ and $J_{off,NBR1}$ from section 6.2.1

$$\frac{dN_{NBR1}}{dt} = \frac{4\pi D_{NBR1}\rho_{NBR1}s_{Ub}RN_{Ub}}{N_{Ub}s_{Ub} + \pi R} - \frac{\Gamma_{off,NBR1}}{R}N_{NBR1}. \tag{6.12}$$

For $N_{NBR1} = N_{eq}$ when $dN_{NBR1}/dt = 0$, and a ubiquitin number proportional to peroxisome surface area, $N_{Ub} = n_0(R/R_0)^2$, the surface density of NBR1 is

$$\frac{N_{eq}}{4\pi R^2} = \frac{D_{NBR1}\rho_{NBR1}s_{Ub}n_0R}{\Gamma_{off}(n_0s_{Ub}R + \pi R_0^2)}. \tag{6.13}$$

Equation 6.13 is shown in Figure 6.2(b) and matches the [p62] = 0 numerical data very well. The diffusive flux per unit surface area to the ubiquitin targets is

$$\frac{J_{on,NBR1}}{4\pi R^2} = \frac{D_{NBR1}\rho_{NBR1}s_{Ub}n_0}{n_0s_{Ub}R + \pi R_0^2}, \tag{6.14}$$

which decreases as R increases, so the increase in NBR1 density with radius is due to the decrease of the dissociation rate with radius, $J_{off,NBR1} \sim 1/R$.

In Figure 6.2(b) the slope of the LIR density vs. R decreases with increasing radius for larger p62 concentrations, and at sufficiently high p62 concentration the slope becomes negative. At sufficiently high p62 concentration, small peroxisomes have a higher LIR density than larger peroxisomes. The result at zero NBR1 can be obtained by considering the dynamics of p62 chains on peroxisomal ubiquitin. When no NBR1 is present, the number of ubiquitin occupied by p62 chains of at least length one, N_{occ}, will be

$$\frac{dN_{occ}}{dt} = \frac{4\pi D_{p62}\rho_{p62}s_{Ub}(N_{Ub} - N_{occ})}{N_{Ub}s_{Ub} + \pi R} - \Gamma_{off,p62,Ub}N_{occ}. \tag{6.15}$$

For $N_{occ,eq}$ when $dN_{occ}/dt = 0$ and $N_{Ub} = n_0(R/R_0)^2$, the surface density of occupied ubiquitin is

$$\frac{N_{occ,eq}}{4\pi R^2} = \frac{n_0/(4\pi R_0^2)}{1 + \Gamma_{off}(n_0s_{Ub}R + \pi R_0^2)/(4\pi D_{p62}\rho_{p62}s_{Ub}.R_0^2)} \tag{6.16}$$

However, these occupied ubiquitin will generally not have a single p62, but rather a p62 chain. On average, a chain will have length $L(T) = 1+4\pi D_{p62}\rho_{p62}s_{Ub}RT/(N_{Ub}s_{Ub}+$

πR) after a growth period of time T. The probability that the base p62 will remain bound to the ubiquitin is $P(T) = \Gamma_{off,p62,Ub}\ e^{-\Gamma_{off,p62,Ub}T}$, so that after equilibration, the average chain length on a peroxisome is

$$\langle L \rangle = \int_0^\infty P(T)L(T)dT = 1 + \frac{4\pi D_{p62}\rho_{p62}R_0^2}{\Gamma_{off,p62,Ub}(n_0 s_{Ub}R + \pi R_0^2)}. \tag{6.17}$$

The surface density of p62 on a peroxisome, with no NBR1, is then $\langle L \rangle N_{occ,eq}/(4\pi R^2)$. This result is shown in Figure 6.2(b) as a dashed black line and matches the [NBR1] = 0 numerical data very well. The LIR density in Figure 6.2(b) transitions from positive slope with [p62] = 0 to negative slope with [NBR1] = 0.

6.3.2 Ubiquitin Increases with Clustering Forbidden

Ubiquitin can induce pexophagy [18] and it has been suggested that increased ubiquitin levels would signal increased pexophagy after peroxisome proliferation[177]. To investigate the response of our system to different ubiquitin levels, we increase the ubiquitin numbers on peroxisomes. We do this in two ways, shown in Figure 6.3(a). The ubiquitin numbers can be increased on all peroxisomes, representing a global or cell-wide response of increased ubiquitin numbers, possibly in response to a removal of proliferators. Alternatively, ubiquitin numbers can be increased on a single peroxisome, representing a damaged peroxisome. The simple time-dependence of the ubiquitin increase that we apply is an instantaneous increase from an initial (low) ubiquitin level to a final (high) ubiquitin level as shown in Figure 6.3(b). This approximation assumes that changes due to the increased ubiquitin level occur on longer timescales than the timescale of the change in ubiquitin level itself. Since all ubiquitin numbers on the model peroxisomes are proportional to surface area, $N_{Ub}(R) = n_0(R/R_0)^2$, the ubiquitin level coefficient n_0 is simply increased to implement the change in the ubiquitin level.

We explore the effect of increasing the ubiquitin number on the number of LIRs (NBR1 + p62) on peroxisomes. Again, ensembles of 100 spheres with radii exponentially distributed between $R = 0.05\mu$m and 0.50μm are used.

In Figure 6.3(c) the ubiquitin level is tripled on all spheres — $n_0 = n_{0,i} = 100$ is changed to $n_{0,f} = 300$. First we consider the case of $[p62] = 0$. Then the equilibrium

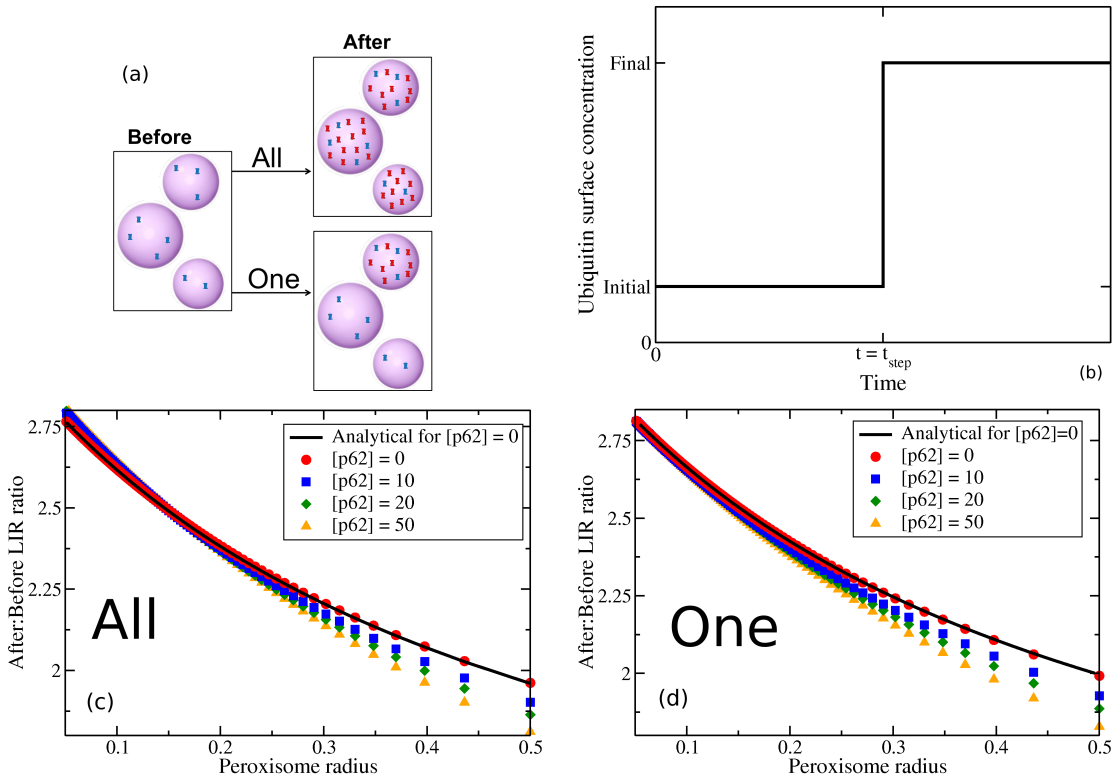

Figure 6.3: Ubiquitin increase on peroxisomes and resulting NBR1 and p62 increases. Clustering forbidden. (a) Schematic of ubiquitin level changes. Purple spheres represent peroxisomes. On left, irregular blue shapes represent ubiquitin present on peroxisomes before a ubiquitin increase. On the right, more ubiquitin is added, shown as irregular red shapes. We increase ubiquitin on all peroxisomes, as shown top right, or on a single peroxisome, shown bottom right. (b) The increase of ubiquitin is modelled as an instantaneous event. At a given time, the ubiquitin on all peroxisomes, or a single peroxisome, is increased to a higher surface concentration. (c) Increases in LIR-domain containing proteins, the sum of NBR1 and p62, expressed as a ratio of after:before an increase of the ubiquitin level on all peroxisomes by a factor of three — with n_0 the ubiquitin coefficient, the number of ubiquitin on each peroxisome is $N_{Ub}(R) = n_0(R/R_0)^2$, with $R_0 = 0.25\mu$m, and before $n_0 = 100$, and after $n_0 = 300$. A system of 100 peroxisomes is used, with the radius exponentially distributed between $R = 0.05\mu$m and $R = 0.50\mu$m. The after:before LIR ratio depends on the peroxisome radius, although each curve represents a single system. Initial NBR1 concentration is $50\mu\text{m}^{-3}$, and the p62 concentration is varied as indicated. Points show numerical results, while the black line shows equation 6.19 with $\rho_f/\rho_i = 0.982$. (d) Increases in LIR numbers, expressed as a ratio of after:before an increase of ubiquitin level on individual peroxisomes by a factor of three, so that before $n_0 = 100$ and after $n_0 = 300$. 100 peroxisomes are used, with radius exponentially distributed between $R = 0.05\mu$m and $R = 0.50\mu$m. The after:before ratio depends on the peroxisome radius, but since the ubiquitin level is increased on a single peroxisome, each point represents a single system, with the curve representing 100 systems (one system for the increase on each peroxisome). Initial NBR1 concentration is $50\mu\text{m}^{-3}$, and the p62 concentration is varied as indicated. Points show numerical results, while the black line shows equation 6.19 with ρ_f/ρ_i of unity.

NBR1 number is as above,

$$N_{eq} = \frac{4\pi D_{NBR1}\rho_{NBR1}s_{Ub}n_0R^3}{\Gamma_{off,NBR1}(n_0 s_{Ub}R + \pi R_0^2)}. \tag{6.18}$$

$N_{eq,i}$ represents the equilibrium number before the ubiquitin increase, and $N_{eq,f}$ after the increase. These will differ in n_0, but also in the bulk NBR1 concentration ρ_{NBR1}. This results in a ratio

$$\frac{N_{eq,f}}{N_{eq,i}} = \frac{n_{0,f}}{n_{0,i}} \times \frac{\rho_f}{\rho_i} \times \frac{n_{0,i}sR + \pi R_0^2}{n_{0,f}sR + \pi R_0^2}. \tag{6.19}$$

Comparing this to the numerical result in Figure 6.3(c) shows excellent agreement using $\rho_f/\rho_i = 0.982$. This concentration ratio of close to unity demonstrates that only a small fraction of the NBR1 in the bulk surrounding the peroxisomes is taken up to the surface of the peroxisomes after the ubiquitin increase.

Equation 6.19 describes how the final:initial NBR1 ratio from the ubiquitin increase has a larger increase for small peroxisomes than for larger peroxisomes, even for the [p62] = 0 systems which only contain NBR1. This occurs because of the diffusion-limited arrival of NBR1 to ubiquitin targets. The first term of equation 6.19 directly reflects the increase in ubiquitin targets, and the second term only has a minor effect as it is close to unity, while the third term reflects the diffusion-limited factor. Total diffusive flux to absorbing targets on spheres increases as the number of targets increases, however there are diminishing returns as the flux per target decreases with increasing number of targets. The third term of equation 6.19 shows that for spheres with target densities independent of size, the diminishing returns are more pronounced for large spheres, leading to a smaller increase in LIR as the ubiquitin levels on peroxisomes are raised.

Increasing the p62 concentration favours even more LIRs on smaller peroxisomes compared to larger peroxisomes in Figure 6.3(c). Again, this is for the same reason as provided for a similar effect in Figure 6.3(b): diminishing returns in increases of the diffusion-limited arrival rate of p62 to NBR1 and ubiquitin targets.

In Figure 6.3(d) the ubiquitin level is tripled on a single peroxisome, rather than the entire system. Each point in Figure 6.3(d) is one such system, with a different peroxisome experiencing a ubiquitin increase in each system. The number of LIR-containing proteins increases more for smaller peroxisomes than larger peroxisomes,

as in Figure 6.3(c). Equation 6.19 again describes the after:before NBR1 ratio for [p62] = 0, showing good agreement for ρ_f/ρ_i of unity. The global NBR1 concentration essentially does not change because only a single peroxisome is taking up additional NBR1, rather than the entire ensemble. The agreement of equation 6.19 with ρ_f/ρ_i of unity is better for smaller peroxisomes compared to larger peroxisomes, as small peroxisomes take up even less material than larger peroxisomes. Again, as with Figure 6.3(c), increasing the p62 concentration leads to an even larger increase in LIR for smaller peroxisomes compared to larger peroxisomes.

While we will return to it in the discussion, here we briefly discuss the results for systems with clustering forbidden. Figure 6.2(a) shows the number of LIR (sum of NBR1 and p62) on a peroxisome increases smoothly as NBR1 and p62 concentrations are increased. For systems with many peroxisomes, the LIR densities are not equal on all peroxisomes. In Figure 6.2(b), with [p62]= 0 large peroxisomes have a greater LIR density, while with [NBR1] = 0 small peroxisomes have a higher LIR density. If higher LIR densities lead to more degradation, then small or large peroxisomes would not consistently be preferred for degradation at all NBR1 and p62 concentrations. In Figures 6.3(c) and 6.3(d) the ubiquitin level is raised on all peroxisomes and on individual peroxisomes, respectively. In both cases, the ubiquitin increase causes a greater relative increase in LIR on small peroxisomes compared to large peroxisomes. NBR1 is both necessary and sufficient for pexophagy [19], and so this greater increase in LIR for smaller peroxisomes in Figures 6.3(c) and 6.3(d), along with the higher LIR densities on large peroxisomes with NBR1 alone in Figure 6.2(b), suggests that with clustering forbidden it would be difficult to select peroxisomes for degradation on the basis of size.

6.3.3 Systems with Clustering Allowed

Now we investigate systems with clustering. Figure 6.4(a) has the time dependence of NBR1 and p62 quantities for a single $R = 0.25\mu$m peroxisome which initially has zero NBR1 and p62 on its surface. At early times the numbers of free (non-cluster) surface NBR1 and p62 on ubiquitin quickly climb. Immediately following is an increase in the number of p62 on free NBR1, as this population needed to wait for NBR1 targets. Once a critical free NBR1 concentration is reached, a cluster forms and quickly grows.

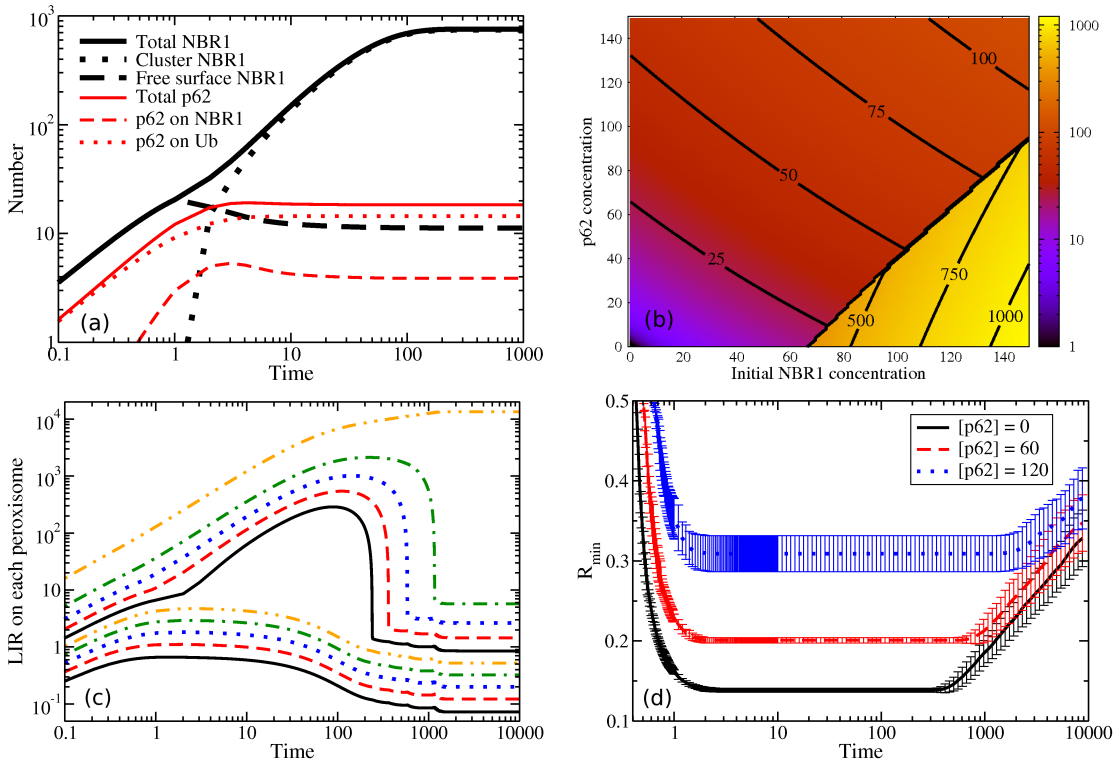

Figure 6.4: Clustering allowed. (a) One peroxisome, $R = 0.25\mu$m. Initially zero NBR1 and p62 on the peroxisome, with initial bulk [NBR1] = $120\mu\text{m}^{-3}$ and [p62] = $40\mu\text{m}^{-3}$. Time dependence of NBR1 and p62 quantities on peroxisome shown. (b) System of one peroxisome, $R = 0.25\mu$m. Intensity plot shows the equilibrium number of LIR-domain containing proteins, the sum of NBR1 and p62, on the peroxisome. Initially there is zero NBR1 and p62 on the peroxisome, and the indicated initial NBR1 concentration in the bulk volume. The indicated p62 concentration is held constant. A clear boundary separates the non-clustering region (roughly the left side, red and purple) from the clustering region (right side, yellow). (c) System of ten peroxisomes, with radii exponentially distributed between $R = 0.05\mu$m and $R = 0.50\mu$m. Initial [NBR1] = $150\mu\text{m}^{-3}$, and [p62] = 0. Each curve represents the number of NBR1 on a different peroxisome. Clusters form on five peroxisomes (top five lines), corresponding to the largest five peroxisomes. Four of the five clusters evaporate through Ostwald ripening interaction. After a cluster remains on only a single peroxisome, the number of LIRs on each peroxisome changes little. (d) System of 100 peroxisomes, with radii exponentially distributed between $R = 0.05\mu$m and $R = 0.50\mu$m. Results are averaged over 100 systems with peroxisome radii independently selected from $P(R) \propto e^{-R/R_s}$ for each system. The radius of the smallest peroxisome with a cluster, R_{min}, is plotted vs. time. Initial [NBR1] = $150\mu\text{m}^{-3}$, and p62 concentration as indicated. Initially all peroxisomes have zero NBR1 and p62. Error bars indicate standard deviation. A cluster forms on the largest peroxisome first, and proceeds with formation on the next largest peroxisome until cluster formation stops. Evaporation occurs first from the smallest peroxisome with a cluster and so the size of the smallest peroxisome with a cluster is plotted against time — all peroxisomes larger than this size have a cluster, and all smaller do not have a cluster.

The number of free NBR1 somewhat decreases, as the free NBR1 now only maintain an equilibrium vapour surrounding the cluster. The number of p62 on free NBR1 correspondingly decreases as there are fewer free NBR1 available, while the number of p62 on ubiquitin is unaffected. The NBR1 cluster grows until there is no longer material available for further growth, and at later times all NBR1 and p62 quantities have settled to unchanging values in this single peroxisome system, although they may continue to change in multiple peroxisome systems.

Similar to Figure 6.2(a), in Figure 6.4(b) we track the total number of LIRs on a single peroxisome as the initial NBR1 and constant p62 concentrations are varied. However, a sudden increase in the number of LIR domains is seen as the NBR1 concentration is increased — this corresponds to clustering. The clustering region of Figure 6.4(b) has approximately $10\times$ the number of LIR domains as the number of LIR domains for the non-clustering system of Figure 6.2(a). In Figure 6.4(b), as the NBR1 concentration is increased, the transition from no cluster to a cluster causes a very non-linear and drastic increase in the number of LIRs over a very small range of NBR1 concentrations. The cluster allows the peroxisome surface to have a much larger number of LIRs than it could otherwise. In the non-clustering region, on the left side of Figure 6.4(b), the LIR numbers are identical to the system with clustering forbidden, in Figure 6.2(a).

In Figure 6.4(b) higher p62 concentrations push the transition to clusters to higher NBR1 concentrations — p62 inhibits cluster formation. This is due to our model forbidding NBR1 with p62 chains from participation in cluster formation or joining an existing cluster, motivated by steric repulsion. Higher p62 concentrations lead to fewer NBR1 lacking p62 at a given NBR1 concentration, requiring higher NBR1 concentrations to provide sufficient NBR1 without p62 for cluster formation.

Next a system of 10 peroxisomes, exponentially distributed between radius $R = 0.05\mu$m and $R = 0.50\mu$m, was examined. Figure 6.4(c) shows the number of LIRs on each of these peroxisomes in time. Initially the number of LIRs increases on all peroxisomes, with some peroxisomes forming a cluster on their surface. The peroxisomes that do not form a cluster experience a decrease in the number of LIRs on their surface. The clusters that do form compete for material — the smallest cluster shrinks until it evaporates, followed by the next smallest cluster, until there is only

a single cluster remaining. This competition between clusters for material, mediated by diffusion between clusters, is known as Ostwald ripening [110, 113]. In previous work [186] we studied the coarsening of clusters on the surface of spherical drops, and found that clusters select larger drops for cluster growth, with clusters on smaller drops evaporating. The selection of clusters on larger peroxisomes for growth in Figure 6.4(c) is the coarsening behaviour seen previously. Additionally, there is size selection in cluster formation, with clusters only forming on the large peroxisomes, and remaining absent from small peroxisomes at all times.

Figure 6.4(d) again shows that large peroxisomes are selected for cluster formation and growth. We track the radius of the smallest peroxisome with a cluster, R_{min}, in time for a system with 100 peroxisomes between $R = 0.05\mu$m and $R = 0.50\mu$m with different p62 concentrations, showing the formation and evaporation of clusters. At short times R_{min} decreases as each cluster forms on the largest peroxisome lacking a cluster, which is smaller than all peroxisomes which have previously formed clusters. Eventually cluster formation ends, and R_{min} stops decreasing. When evaporation begins, the cluster on the smallest peroxisome evaporates first, increasing R_{min}. Evaporation continues until only the largest peroxisome in the system has a cluster. The higher p62 concentrations of Figure 6.4(d) lead to fewer clusters which are only on larger peroxisomes, as well as later cluster formation. Onset of cluster evaporation is also pushed to later times. There are fewer clusters because p62 inhibits cluster formation, both by inhibiting NBR1 uptake onto peroxisomes by blocking ubiquitin, and by preventing NBR1 with p62 from forming or joining clusters. Cluster formation is later because it takes longer for peroxisomes to reach the threshold level (of NBR1 without p62) necessary for cluster formation, due to p62 forming chains on more NBR1. p62 leads to later evaporation of existing clusters because the clusters that do form become larger, and larger clusters will take longer to evaporate. Overall, clusters form on the large peroxisomes and evaporate first from the smallest peroxisomes harbouring a cluster, and p62 enhances this selection of large peroxisomes for NBR1 clusters.

Figures 6.4(c) and 6.4(d) illustrate how clusters on larger peroxisomes are selected for growth and those on smaller peroxisomes for evaporation. Selection of existing clusters on larger peroxisomes for growth is due to faster growth of clusters on large

peroxisomes allowing the slower growing clusters on small peroxisomes to fall below the critical cluster size. This effect can be elucidated from equation 6.9 and is discussed in previous work [186].

Figures 6.4(c) and 6.4(d) also illustrate a selectivity effect distinct from coarsening — the formation of clusters on large peroxisomes rather than on small peroxisomes. This is due to the combination of lower critical concentrations for cluster formation on larger peroxisomes, and higher equilibrium surface NBR1 concentrations on larger peroxisomes.

Larger peroxisomes require a lower concentration for cluster formation, as equation 6.7 states that the critical concentration for cluster formation is $\sigma^* \sim R^{-2/3}$. The critical concentration σ^* corresponds to a cluster radius at formation $r^* \sim (4\pi R^2)^{1/3}$ if the number of molecules initially in a cluster, $N^* = \pi(r^*)^2/b$, where N^* is the cluster size from equation 6.8, r is the cluster radius, and b is the area per molecule. The radius at cluster formation is consistent with the minimum stable island radius of Krishnamachari *et al.* who investigated the formation and growth of islands in finite 2d systems [114]. For a finite system, an increase in cluster size leads to a decrease in vapour pressure, and stability of the cluster size demands the vapour pressure decrease more than the Gibbs-Thomson condition allows, forcing the cluster to shrink to replenish the vapour. This stability requirement leads to a minimum stable island radius $r_{min} \sim V^{1/3}$ for sufficiently large systems, where V is the 2d 'volume' of the system. This result is consistent with our cluster radius at formation, $r^* \sim (4\pi R^2)^{1/3}$.

In addition to larger peroxisomes requiring a lower concentration for cluster formation, the equilibrium surface NBR1 concentration increases with peroxisome radius, as shown by equation 6.13 and the red circles in Figure 6.2(b). Large peroxisomes have a higher equilibrium surface NBR1 concentration and a lower critical concentration for cluster formation, which together explain the strong observed preference for cluster formation on large peroxisomes rather than small peroxisomes.

6.3.4 Ubiquitin Increases with Clustering Allowed

We have seen how clustering evolves in conditions of constant ubiquitin level, but now we examine how changes in the the ubiquitin level affect clustering. In Figure 6.5

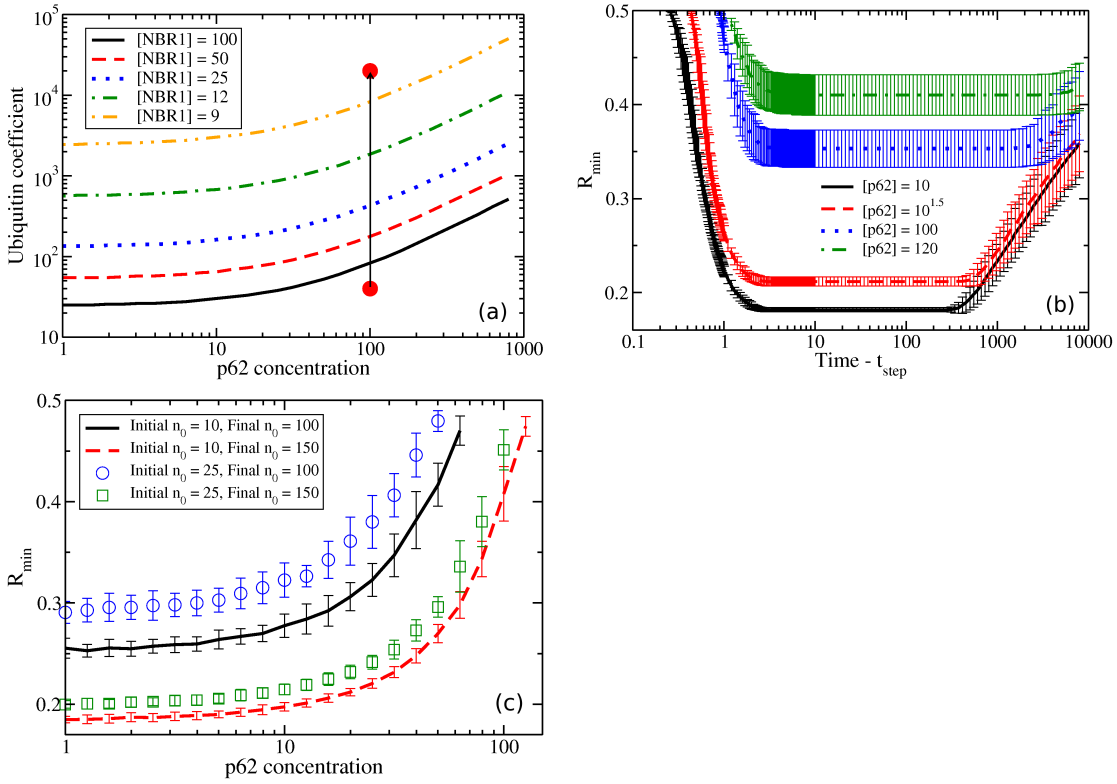

Figure 6.5: Ubiquitin increase on peroxisomes and resulting NBR1 cluster behaviour. Clustering allowed. (a) System of 100 peroxisomes, with radii exponentially distributed between $R = 0.05\mu$m and $R = 0.50\mu$m. Initially zero NBR1 and p62 on peroxisomes, initial NBR1 and p62 concentrations as indicated. With n_0 the ubiquitin coefficient, the number of ubiquitin on each peroxisome is $N_{Ub}(R) = n_0(R/R_0)^2$, with $R_0 = 0.25\mu$m. At a given initial NBR1 concentration (each curve), for each p62 concentration the ubiquitin coefficient n_0 was increased until clustering occurred, and so each curve marks the boundary between no clustering and at least one cluster. The red points mark two ubiquitin coefficients at [p62] = $100\mu\text{m}^{-3}$, and the arrow indicates an increase in the ubiquitin coefficient that would induce clustering. (b) System of 100 peroxisomes, with radii exponentially distributed between $R = 0.05\mu$m and $R = 0.50\mu$m. Results are averaged over 100 systems with peroxisome radii independently selected from $P(R) \propto e^{-R/R_s}$ for each system. There is initially zero NBR1 and p62 on peroxisomes, initial [NBR1] = $80\mu\text{m}^{-3}$, and p62 concentrations as indicated. At $t = t_{step}$ the ubiquitin coefficient increased from $n_0 = 25$ to $n_0 = 150$. The ubiquitin increase induces cluster formation on many peroxisomes, causing an initial very rapid increase in the number of clusters, followed by cluster evaporation due to Ostwald ripening, causing a much slower reduction in number of clusters. The radius of the smallest peroxisome with a cluster, R_{min}, is plotted vs. time. (c) With the same scenario as (b), ubiquitin is increased on a single peroxisome as labelled. The initial [NBR1] = $75\mu\text{m}^{-3}$. The curves show the radius of the smallest peroxisome that forms a cluster, R_{min}. Error bars in (b) and (c) indicate the standard deviation.

the effect of ubiquitin and ubiquitin increases is examined with NBR1 clustering. In Figure 6.5(a), at a set initial NBR1 concentration, we determine the ubiquitin level necessary to cause clustering at a constant p62 concentration. This is done with a system of 100 peroxisomes, with radii exponentially distributed between $R = 0.05\mu$m and 0.50μm. For very low ubiquitin coefficients, there will be no clustering on any peroxisomes. As the ubiquitin coefficient is increased, a coefficient is reached which causes clustering on at least one peroxisome, and this coefficient is determined for each p62 concentration. At the ubiquitin coefficient separating clustering behaviour at high coefficient and non-clustering behaviour at low coefficients is the clustering boundary. As expected, the ubiquitin coefficient needs to be higher for higher p62 concentrations, to overcome the cluster inhibition of p62. At higher NBR1 concentrations, the ubiquitin coefficient needed to cause cluster formation is lower.

The ubiquitin coefficient can be increased to determine the response of the system, as it was in Figure 6.3. Now that clustering is allowed, the ubiquitin coefficient is moved from a non-clustering region, to a clustering region, as shown by the red dots and arrow in Figure 6.5(a). Non-clustering behaviour can reach a steady-state, with the number of NBR1 and p62 on peroxisomes, and the bulk NBR1 concentration, unchanging in time. The increase in ubiquitin then moves the system into a clustering regime, where it cannot reach a steady-state until only a single cluster remains and is instead dynamic for long time periods.

In Figure 6.5(b) the ubiquitin coefficient is increased on all spheres from below the clustering boundary at $t = t_{step}$ for a system of 100 spheres. Following $t = t_{step}$, the number of clusters rapidly increases, does not change for a period of time, and then the number of clusters decreases as clusters begin to evaporate. The clusters that form do so on the largest peroxisomes in the system, and cluster evaporation occurs first on the smallest peroxisomes before proceeding to the next smallest peroxisomes. Higher p62 concentrations lead to less cluster formation and later cluster formation in Figure 6.5(b). Cluster evaporation also begins at a later time. Higher p62 concentrations limit NBR1 clusters to larger peroxisomes.

In Figure 6.5(c) the ubiquitin level is increased on a single peroxisome. We track the radius of the smallest peroxisome that is able to form a cluster when the ubiquitin

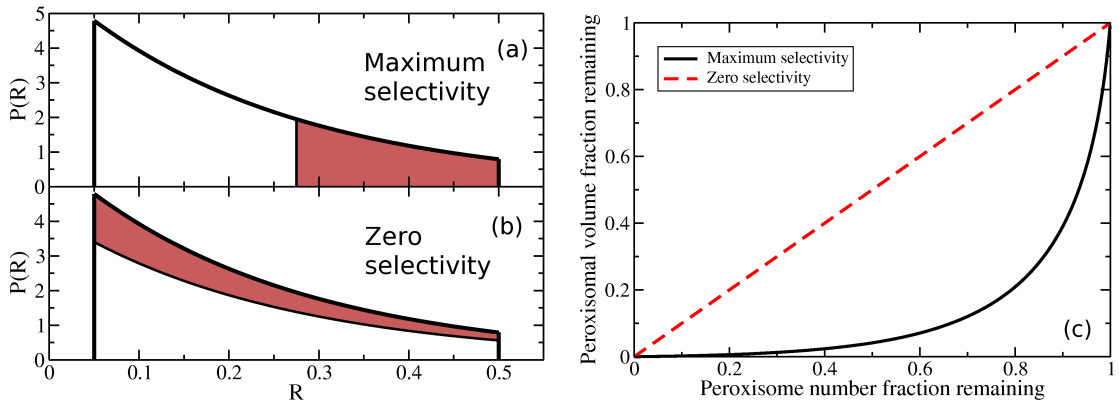

Figure 6.6: (a) The black curve shows a probability distribution of peroxisome radii, $P(R) \propto e^{-R/R_s}$. Maximum selectivity is shown, with the red region indicating that only the peroxisomes with the largest radii will be selected. The red region for maximum selectivity begins on the left at $R = R'_{max}$. (b) is similar to (a), except zero selectivity is shown, so peroxisomes of all radii are equally likely to be selected. The red region for zero selectivity is a factor $p \leq 1$ multiplied by the full probability distribution. The red regions in (a) and (b) are of equal area, and represent an equal number of peroxisomes, when $R'_{max}(p)$ is described by equation 6.20. (c) plots the remaining peroxisome volume as peroxisomes are removed with maximum selectivity (v_{max} in equation 6.21) or with zero selectivity (v_{zero} in equation 6.22).

increase occurs. As the p62 concentration increases, the radius of the smallest peroxisome forming a cluster increases. The radius of the smallest peroxisome able to form a cluster is primarily determined by the final ubiquitin level, rather than the initial ubiquitin level. Larger final ubiquitin levels lead to a decrease in the radius of the smallest peroxisome able to form a cluster, simply explained because the peroxisomes will be able to recruit more NBR1 with more ubiquitin. The final ubiquitin level is the primary factor because, prior to the increase in ubiquitin, much of the NBR1 was in the bulk concentration, rather than on peroxisome surfaces. After the ubiquitin level increases, much of the NBR1 is taken up by the cluster. The initial ubiquitin level has a smaller effect, because it changes how much NBR1 is available in the bulk concentration, but without clusters, these changes will be relatively small.

6.3.5 Observations of Selective vs. Non-selective Degradation

In experiments investigating the degradation of peroxisomes, a common proxy for peroxisome numbers is the amount of catalase [18, 19, 206]. For example, in Figure 1B of Deosaran *et al.* [19], the control measurement of catalase fluorescence intensity

is compared to measurements with siNBR1, and si-p62. Application of si-p62 leads to an increase in catalase fluorescence, application of siNBR1 leads to a larger increase of catalase fluorescence, and combining si-p62 and siNBR1 causes an increase very similar to the application of siNBR1 alone.

Here we ask how the catalase intensity might decrease if some number of peroxisomes were degraded. We compare a scenario with maximum size selectivity, where only the largest peroxisomes are degraded, with a scenario of zero selectivity, where peroxisomes of all sizes are equally likely to be degraded. These two possibilities are shown in Figures 6.6(a) and 6.6(b).

Figure 6.6(c) shows the result of our peroxisome volume calculations below. We assume that catalase intensity is proportional to peroxisome volume, and therefore calculate the fraction of peroxisome volume remaining as the number of peroxisomes is decreased. Prior to any degradation, the probability distribution of peroxisome radii $P(R) = A \cdot \exp(-R/R_s)$ for $R \in [R_{min}, R_{max}]$, with A determined by normalization of $P(R)$ using $R_{min} = 0.05\mu$m, $R_{max} = 0.50\mu$m, and $R_s = 0.10\mu$m, as above. For maximum selectivity, the peroxisome number fraction remaining is $p_{max} = \int_{R_{min}}^{R'_{max}} P(R)dR$, with $R'_{max} \leq R_{max}$ — this selectivity is represented in Figure 6.6(a). For zero selectivity the peroxisome number fraction remaining is $p_{zero} = p_{zero} \int_{R_{min}}^{R_{max}} P(R)dR$ — this selectivity is represented in Figure 6.6(b). Requiring that $p_{max} = p_{zero} = p$, so that an equal number of peroxisomes is removed regardless of selectivity type, gives

$$R'_{max}(p) = -R_s \ln \left[e^{-R_{min}/R_s} - p \left(e^{-R_{min}/R_s} - e^{-R_{max}/R_s} \right) \right]. \tag{6.20}$$

The peroxisome volume remaining for maximum selectivity is

$$v_{max} = \frac{1}{V} \int_{R_{min}}^{R'_{max}(p)} R^3 P(R) dR, \tag{6.21}$$

which is the solid line in Figure 6.6(c). $V = \int_{R_{min}}^{R_{max}} R^3 P(R) dR$ is proportional to the initial average peroxisome volume before any peroxisomes are degraded. For zero selectivity the peroxisome volume fraction remaining is

$$v_{zero} = \frac{p}{V} \int_{R_{min}}^{R_{max}} R^3 P(R) dR, \tag{6.22}$$

which is the dashed line in Figure 6.6(c). With volume remaining after removing peroxisomes with maximum selectivity, v_{max}, and after removing peroxisomes with

zero selectivity, v_{zero}, plotted in Figure 6.6(c), we can see that removing peroxisomes with maximum selectivity decreases the peroxisomal volume significantly more than removing with zero selectivity. Many more peroxisomes need to be removed with zero selectivity to match a volume reduction from the removal of a small number of large peroxisomes at maximum selectivity. This suggests that any mechanism which increases selection of larger peroxisomes could result in significantly less peroxisome volume, and possibly less catalase and less fluorescence intensity from labelled catalase.

6.4 Discussion

Autophagy selectivity of different types of substrates is thought to be mediated by autophagy receptor proteins, which have been observed in domains [6, 9, 10, 105]. Peroxisomes are dynamic organelles, and there can be hundreds of copies in a single mammalian cell [13]. The signalling protein ubiquitin and the autophagy receptor proteins NBR1 and p62 participate in peroxisome autophagy [18, 19, 177].

We have investigated the dynamics of NBR1 and p62 accumulation on ubiquitinated peroxisomes. In our model, ubiquitin recruits NBR1 to the peroxisomes membrane, while p62 can bind to, and form chains on, both ubiquitin and NBR1. At sufficient concentration on the peroxisome surface, NBR1 forms clusters — while NBR1 with p62 chains are forbidden from participating in cluster formation or joining existing clusters.

Our model of NBR1 cluster formation and growth with p62 has several results. NBR1 clustering allows all-or-none colocalization of NBR1 with catalase, and can provide a clear signal of receptor proteins above a critical threshold. Both cluster formation and cluster coarsening select large peroxisomes for NBR1 clusters, providing a clear mechanism to select a subset of peroxisomes for degradation by autophagy. The responses to peroxisome deproliferation and peroxisome damage are distinct, with NBR1 clusters competing during deproliferation and lacking competition if there is damage. p62 inhibits cluster formation leading to enhanced selection of fewer, and larger, peroxisomes. We also argue that selection of large peroxisomes for degradation may lead to a larger decrease in peroxisomal volume, and therefore peroxisomal enzymes such as catalase, compared to peroxisome degradation independent of size.

6.4.1 Impact of Allowing Clustering

In Figure 5 of Deosaran *et al.* [19], catalase (indicating peroxisomes) and NBR1 colocalize in an all-or-none manner, with many catalase puncta with little NBR1 colocalization, and puncta with significant NBR1 colocalization. This all-or-none colocalization suggests that peroxisomes either accumulate many NBR1 or few NBR1. The clustering results of our model, which have a sudden increase in NBR1 at the onset of clustering, are consistent with the observed all-or-none colocalization in Deosaran *et al.* [19]. It is challenging to explain the observations with the smooth increase of NBR1 occurring when clustering is forbidden.

Deosaran *et al.* [19] also introduced the idea of a 'critical mass' of autophagy receptor proteins necessary to target peroxisomes to autophagosomes. Clustering of NBR1, with the sudden increase in LIR numbers it can provide, allows the system to provide a clear signal of receptor proteins that is either above or below a threshold or critical number on each peroxisome. A peroxisome without a cluster has relatively few NBR1 and p62, and is clearly below the threshold for targeting to an autophagosome. A peroxisome with a cluster has relatively many NBR1, and could provide a clear signal for autophagosome targeting. Systems without clustering may struggle to provide a clear low or high level of NBR1 and p62.

6.4.2 Cluster Nucleation and Coarsening

In our previous work [186], we found that clusters on the surface of spherical drops will evaporate first from smaller drops, selecting large drops for cluster growth. In this paper, we found that cluster formation favours larger peroxisomes, in addition to reinforcing the earlier finding of cluster evaporation from smaller peroxisomes. Cluster formation occurs on large peroxisomes because of a higher equilibrium NBR1 concentration prior to cluster formation, and due to a lower surface concentration threshold for cluster formation. The selection of large peroxisomes for cluster formation and coarsening is seen in Figures 6.4(c) and 6.4(d), with the first cluster forming on the largest peroxisomes and then proceeding to the next smallest peroxisome and so on, and cluster evaporation beginning on the smallest peroxisome with a cluster and proceeding to the next smallest peroxisome. Figure 6.5(b) and 6.5(c) show the same behaviour after increases in the ubiquitin level on all peroxisomes and individual

peroxisomes, respectively. NBR1 clustering provides a consistent signal for autophagy to target and degrade large peroxisomes. This is in line with observations that larger peroxisomes are preferentially degraded when the number of peroxisomes is being reduced [171]. A size effect in pexophagy is also consistent with larger peroxisomes requiring more autophagy-related proteins to facilitate degradation [85].

In our previous work [186], we estimated the timescale for selection of larger drops for clusters through Ostwald ripening. In this work, peroxisomes are selected by cluster formation, as well as evaporation due to Ostwald ripening. Cluster formation also selects large peroxisomes and occurs very quickly, with the number of clusters peaking after an increase in the ubiquitin level in < 10s in Figure 6.5(b). Following cluster formation, evaporation of clusters also occurs, leaving clusters only on large peroxisomes, beginning after 10^2-10^4s in Figure 6.5(b). Cluster formation and cluster coarsening are distinct stages of peroxisomes selectivity, both selecting large peroxisomes for NBR1 clusters. The timescale of cluster formation is very rapid in comparison to the 10^4 - 10^5s necessary for the onset of cluster selectivity through Ostwald ripening of existing clusters [177]. Selection of large peroxisomes by NBR1 cluster formation will therefore easily be in place for mammalian and yeast pexophagy, which take place in days [134, 84] and hours [81, 82], respectively. Coarsening of clusters at later times will push the degradation to even larger peroxisomes.

6.4.3 Peroxisome Number Reduction vs. Peroxisome Damage

In this paper we use an increase in ubiquitin number as a initial signal that can lead to additional NBR1 and p62 accumulation, possibly followed by degradation by autophagy. Ubiquitination of peroxisomes has been shown sufficient to induce pexophagy [18], ubiquitin is thought to recruit NBR1, the primary autophagy receptor protein for peroxisomes, to the peroxisomes membrane [19], and earlier modelling suggests that an increase in ubiquitin could be a natural and self-correcting response of the cell to requiring fewer peroxisomes [177]. Ubiquitin is known to play a role in the routine import of peroxisome matrix proteins [177], is part of the quality control system for damaged proteins on peroxisomes [140, 141, 142], in addition to the well known role of ubiquitin as a signal for the ubiquitin-proteasome system [8].

In Figure 6.3(a) we identify two extreme cases of increases in the ubiquitin level:

a global increase, where ubiquitin levels on all peroxisomes increase, and an increase of the ubiquitin level on a single peroxisome. A global increase could be due to the removal of peroxisome proliferators [133], or a change in growth medium [81], both of which can result in a decrease in peroxisome numbers. An increase on a single peroxisome could be due to damage [187, 188].

Figure 6.5(b) shows the clustering response to a ubiquitin increase on all peroxisomes. This results in competition for the NBR1 needed to form clusters, and the large peroxisomes are selected for NBR1 clusters and pexophagy. This would mean that in a situation where the cell required a decrease in peroxisome numbers, the large peroxisomes would be preferentially degraded until the decrease in peroxisome numbers had been achieved. This is consistent with observations that larger peroxisomes are preferentially degraded when reducing peroxisome numbers [171]. The peroxisomes selected following a ubiquitin increase also changes with time, as clusters continue to evaporate.

Figure 6.5(c) shows the clustering response to a ubiquitin increase on a single peroxisome. There is no competition for the NBR1 needed to form clusters, because only a single peroxisome has an elevated ubiquitin level. The selection of an individual peroxisome through a ubiquitin increase is not time dependent, as the clusters formed do not evaporate. The larger peroxisomes more easily form NBR1 clusters in this situation, suggesting that larger peroxisomes may need less damage to be labelled for autophagy. Due to the lack of competition between clusters when individual peroxisomes increase their ubiquitin level, we expect that selection of peroxisomes based on size will be stronger for deproliferation than for damage.

Clustering following a ubiquitin increase on all peroxisomes or on a single peroxisome appears to allow an appropriate clustering response to facilitate a reduction in peroxisome numbers and to damage, respectively. For a ubiquitin increase on all peroxisomes, clustering selects larger peroxisomes for degradation, a clear subpopulation, with this selection becoming tighter with time as clusters evaporate. For a ubiquitin increase on a single peroxisome, larger peroxisomes are still more able to gain a cluster, however the smaller peroxisomes that do gain a cluster do not compete for NBR1 and will retain their cluster. A further elevation in the ubiquitin level of a damaged peroxisome would eventually lead to recruitment of sufficient NBR1 for

cluster formation, without other peroxisomes sequestering NBR1 in their clusters.

6.4.4 Effect of p62

The autophagy receptor protein p62 is important for pexophagy [18]. Application of p62 siRNA results in an increase of catalase fluorescence intensity, but NBR1 siRNA results in a larger increase of catalase fluorescence intensity, with NBR1 thought both necessary and sufficient for pexophagy [19]. However, the increase of p62 resulting in increased catalase intensity suggests that p62 causes increased pexophagy.

p62 is very similar to NBR1, but differs in that NBR1 can bind to membranes while p62 cannot [19], and p62 can form chains using its PB1 domain while the PB1 domain of NBR1 only interacts on one side [93], with coiled-coil domains on NBR1 providing self-interaction [19]. In our model, p62 chains on NBR1 prevent NBR1 from forming or joining clusters, and effectively p62 inhibits clusters and raises the amount of NBR1 necessary for cluster formation. Inhibition is seen in Figure 6.4(b) with the larger NBR1 concentrations necessary for clustering as the p62 concentration increases, and in Figure 6.4(d) fewer clusters are formed with higher p62 concentrations. Above we proposed that NBR1 clustering labels peroxisomes for autophagy — what is the effect of p62 in this system?

We have demonstrated that for clustering NBR1 with p62 inhibiting clustering, increased p62 levels cause greater selectivity. In Figure 6.4(d), higher p62 concentrations lead to an increase in the minimum peroxisome size with a cluster. Figure 6.5(b) shows the same effect after an increase in the ubiquitin concentration on all peroxisomes — increasing p62 concentration restricts clusters to ever-larger peroxisomes. In Figure 6.5(c), an increase of the ubiquitin concentration on a single peroxisome is only able to induce cluster formation on the larger peroxisomes, and again clustering is pushed to even larger peroxisomes as the p62 concentration is increased.

The inhibitory effect of p62 in our model is primarily due to steric interactions preventing NBR1 with p62 chains from participating in cluster formation or cluster growth. Without the steric interaction, the only inhibitory effect on clustering from p62 would be from p62 chains on ubiquitin blocking the recruitment of NBR1 to the peroxisome surface, and so without the steric interaction only relatively quite high p62 concentrations are expected to cause significant increases in selectivity.

In our model, increasing p62 pushes the NBR1 clusters to larger peroxisomes, and the corresponding degradation of the peroxisomes holding those clusters, implying less pexophagy and a larger number of peroxisomes compared to systems lacking p62. However, observations [19, 18] suggest that p62 knockdown results in more catalase, which has been interpreted as more peroxisomes. If our model is correct, then pexophagy may be due to more than a simple count of the number of LIR domains on a peroxisome, but other properties, such as ability of p62 to form chains [103], may allow systems with p62 to increase recruitment of autophagosomes to peroxisomes, compared to systems lacking p62.

However, we propose a possible alternative explanation of the experimental observations. When p62 siRNA is applied, the catalase fluorescence intensity increases [19, 18]. From our results, we expect that removing p62 would decrease the selectivity of pexophagy. Figures 6.6(a) and (b) illustrate two extremes of pexophagy selectivity: maximum selectivity, where the largest peroxisomes are degraded first; and zero selectivity, where peroxisomes of all sizes are equally likely to be degraded. The volume loss from these two extremes of selectivity is plotted in Figure 6.6(c), showing that with maximum selectivity the peroxisome volume can decrease significantly more for a given number of peroxisomes degraded, compared to zero selectivity. If catalase fluorescence is proportional to peroxisome volume lost, the decrease of selectivity from p62 knockdown could cause a significant increase in catalase fluorescence as the larger peroxisomes are no longer preferentially degraded.

We have seen how NBR1 clusters can select some peroxisomes for degradation by autophagy, and not others, by preferentially clustering on large peroxisomes. We have seen that through inhibiting NBR1 cluster formation and growth, p62 can enhance the selection of large peroxisomes, showing a possible effect of autophagy receptor protein interaction. The response to damage on a single peroxisome can also be distinct from a deproliferation signal on all peroxisomes, with the latter leading to competition between growing clusters.

6.5 Appendix A: Diffusion-limited Rates

For NBR1 and p62 dynamics we use diffusion-limited rates for the arrival of these proteins to targets on peroxisomes. Berg and Purcell [117] determined the diffusion-limited arrival rate of molecules to a population of absorbing circular targets of the same radius on the surface of a sphere. The absorbing targets in our system are not all the same size, and so we determine the diffusion-limited arrival rate for a sphere with several populations of targets, each population with a different target radius. In this appendix we follow the approach of Berg and Purcell [117] to find the diffusion-limited rates in our system.

The diffusive flux to an absorbing surface J is related to the capacitance C of the surface by

$$J = \frac{CDc_\infty}{\epsilon_0}, \tag{6.23}$$

where D is the diffusivity, c_∞ is the concentration far from the surface, and ϵ_0 is the permittivity of free space. We seek the capacitance of N circular targets (discs), of different radii s_i, on a sphere of radius a. A population of discs will be considered, where N_1 discs have radius s_1, and N_2 discs have a radius s_2, and so on, so that $N = \sum_i N_i$.

The potential of the j'th disc, ϕ_j, is determined by

$$\phi_j = \sum_k h_{jk} q_k, \tag{6.24}$$

where h_{jk} are the potential coefficients, which relate the charge of the k'th disc, q_k to the potential ϕ_j. First it is assumed that only the k'th disc has a charge q_k, and all other discs have no charge. The capacitance of an isolated conducting disc of radius s is $4\epsilon_0 s$, and $h_{kk} = 1/(4\epsilon_0 s)$. The average potential on the sphere surface due to this charged disc is $q_k/(4\pi\epsilon_0 a)$, as the average potential on the surface is equal to the potential in the centre of the sphere, and the net image charge is zero. For a subset of N_i discs of radius s_i

$$\frac{q_k}{4\pi\epsilon_0 a} = \frac{\sum_{j\neq k} \phi_j}{N_i - 1} = \frac{q_k}{N_i - 1} \sum_{j\neq k \in N_i} h_{jk}. \tag{6.25}$$

If N_i is large then $\sum_{j\neq k\in N_i} h_{jk} = N_i/(4\pi\epsilon_0 a)$. Putting this result and $h_{kk} = 1/(4\epsilon_0 s)$

into equation 6.24 gives us for a disc in population k

$$\phi_j = \frac{q_k}{4\epsilon_0 s_k} + \sum_i \frac{q_i N_i}{4\pi\epsilon_0 a}. \tag{6.26}$$

Now we determine the capacitance, $C = Q/\phi$. Any ϕ_j may be used because the potentials of all discs are equal — this also forces $q_i 1/s_i 1 = q_i 2/s_i 2$.

$$C = \frac{\sum_i N_i q_i}{\frac{q_k}{4\epsilon_0 s} + \sum_i \frac{q_i N_i}{4\pi\epsilon_0 a}}. \tag{6.27}$$

This can be rewritten as

$$C = \frac{4\pi\epsilon_0 a \sum_i N_i s_i}{\pi a + \sum_i N_i s_i}. \tag{6.28}$$

Putting equation 6.28 into equation 6.23 gives us our flux

$$J = \frac{4\pi D c_\infty a \sum_i N_i s_i}{\pi a + \sum_i N_i s_i}. \tag{6.29}$$

For a single disc of radius s, among disc populations of radius s_i numbering N_i, the flux will be

$$J = \frac{4\pi D c_\infty a s}{\pi a + \sum_i N_i s_i}. \tag{6.30}$$

Equation 6.30 is used to determine the NBR1 and p62 fluxes to peroxisomal targets.

6.6 Appendix B: Cluster Formation

Above a critical surface concentration NBR1 will form clusters. In this appendix we derive the self-consistency condition for cluster formation, given the peroxisome radius R and applying the Gibbs-Thomson effect.

To determine the threshold surface concentration of molecules necessary to form a cluster, we first require that the number of molecules before and after formation is conserved:

$$4\pi R^2 \sigma = N_{clust} + N_{vapour}. \tag{6.31}$$

R is the sphere radius, σ is the surface concentration of molecules prior to formation, N_{clust} is the number of molecules in the cluster after formation, and N_{vapour} is the number of molecules in the vapour after formation. Since the edge of the cluster is not

straight, but rather a circle on the surface of the sphere, we must satisfy the Gibbs-Thomson condition [114] for curved interfaces, which requires an elevated vapour pressure,

$$N_{vapour} = 4\pi R^2 f_\infty \left(1 + \frac{\nu}{r}\right). \tag{6.32}$$

f_∞ is the equilibrium vapour pressure at a flat interface, ν is the capillary length, and r is the radius of the cluster. Combining equation 6.31 with equation 6.32, and setting $N_{clust}b = \pi r^2$, with b the area per molecule, we have

$$\sigma = \frac{N_{clust}}{4\pi R^2} + f_\infty \left(1 + \frac{\sqrt{\pi}\nu}{\sqrt{bN_{clust}}}\right). \tag{6.33}$$

By setting $\partial\sigma/\partial N_{clust} = 0$ we find the minimum cluster size, N^*_{clust}, and corresponding minimum concentration σ^*

$$N^*_{clust} = \pi R^{4/3} \left(\frac{2f_\infty \nu}{\sqrt{b}}\right)^{2/3}, \tag{6.34}$$

$$\sigma^* = f_\infty + 3\left(\frac{f_\infty \nu}{4\sqrt{b}R}\right)^{2/3}. \tag{6.35}$$

A cluster of size N^*_{clust} from equation 6.34 is formed when the NBR1 concentration reaches σ^* from equation 6.35 on a peroxisome surface.

Our cluster formation results are consistent with a free-energy formulation of cluster formation from Krishnmachari *et al.* [114]. They have the free energy change for a cluster formation as

$$\Delta F_{tot} = 2\pi r\gamma + \rho_s \pi r^2 k_B T \ln\left(\frac{\rho_\infty}{\rho_i}\right) - \pi r^2 k_B T(\rho_\infty - \rho_s) - (N - \rho_s \pi r^2) k_B T \ln\left(\frac{V - \pi r^2}{V - \rho_s \pi r^2 V/N}\right), \tag{6.36}$$

where r is the cluster radius, γ is the interface energy, ρ_s is the number density of the cluster, $k_B T$ is the thermal energy scale, ρ_∞ is the vapour density for a flat interface, ρ_i is the initial number density, N is the initial number of molecules in the vapour, and V is the two-dimensional 'volume' (the area) of the system. If the free energy, equation 6.36 is extremized by taking $\partial F_{tot}/\partial r = 0$ then we have [114]

$$\ln\left(\frac{\rho_f}{\rho_\infty}\right) = \frac{\gamma}{r\rho_s k_B T} + \frac{\rho_f - \rho_\infty}{\rho_s}, \tag{6.37}$$

with $\rho_f = (N - \rho_s \pi r^2)/(V - \pi r^2)$. The second term on the RHS of equation 6.37 is usually small, as the cluster is usually much more dense than the vapour, so

$$\ln\left(\frac{\rho_f}{\rho_\infty}\right) \simeq \frac{\gamma}{r\rho_s k_B T} \tag{6.38}$$

can be used. This approximation leads to the Gibbs-Thomson formula:

$$\rho(r) = \rho_\infty \exp\left[\gamma / \left(r \rho_s k_B T\right)\right]. \tag{6.39}$$

Converting to the variables for the cluster formation model presented in this paper, $r = \sqrt{N_{clust} b/\pi}$, $\rho_i = N_{vapour}/(4\pi R^2)$, $\rho_s = 1/b$, $V = 4\pi R^2$, $\rho_\infty = f_\infty$, $N = 4\pi R^2 \sigma$, and $\nu = \gamma b/(k_B T)$, equation 6.38 can be rewritten

$$\frac{1}{f_\infty}\left(\frac{4\pi R^2\sigma - N_{clust}}{4\pi R^2 - N_{clust} b}\right) = \exp\left(\frac{\sqrt{\pi}\nu}{\sqrt{N_{clust} b}}\right). \tag{6.40}$$

If the capillary length ν is small in comparison to the cluster size, then $\exp(\sqrt{\pi}\nu/\sqrt{N_{clust}b}) \simeq 1 + \sqrt{\pi}\nu/\sqrt{N_{clust}b}$, and

$$\frac{1}{f_\infty}\left(\frac{4\pi R^2\sigma - N_{clust}}{4\pi R^2 - N_{clust} b}\right) \simeq 1 + \frac{\sqrt{\pi}\nu}{\sqrt{N_{clust} b}}. \tag{6.41}$$

Solving for the pre-cluster formation concentration, σ, gives us

$$\sigma = \frac{N_{clust}}{4\pi R^2} + f_\infty\left(1 + \frac{\sqrt{\pi}\nu}{\sqrt{N_{clust} b}}\right) - \frac{N_{clust} b}{4\pi R^2}\left(f_\infty + \frac{\sqrt{\pi}\nu f_\infty}{\sqrt{N_{clust} b}}\right). \tag{6.42}$$

The final term on the RHS of equation 6.42 has coefficient $N_{clust}b/(4\pi R^2)$, the fraction of the sphere surface area covered by the cluster, which will be small for small clusters. Neglecting this final term allows equation 6.42 to exactly match equation 6.33, demonstrating that our cluster formation results are consistent with a free energy approach to cluster formation.

6.7 Appendix C: Cluster Growth

Existing clusters can gain molecules and grow, or lose molecules and shrink. Here we determine the change in time of the size of NBR1 clusters on peroxisomes by considering the diffusive behaviour of NBR1 with and without p62 chains on peroxisome surfaces.

Equation 6.4 describes the change in time of the number of NBR1 with p62 chains of length l. Only NBR1 with no p62 chain ($l = 0$) can contribute to cluster growth. Number of NBR1 with no p62, $N(0)$, is divided by surface area, $4\pi R^2$, to give the surface concentration f_0. f_0 can be a spatial field on the surface of the sphere, and so

converting to f_0 from $N(0)$ and adding a surface diffusion term, equation 6.4 becomes

$$\frac{d\tilde{f}_0}{dt} = D_s\nabla^2\tilde{f}_0 - \frac{4\pi D_{p62}\rho_{p62}s_{NBR1}R}{N_{tot}s_{NBR1} + n_{Ub}s_{Ub} + \pi R}\tilde{f}_0 - \frac{\Gamma_{off,NBR1}}{R}\tilde{f}_0 + \frac{D_{NBR1}\rho_{NBR1}s_{Ub}n_{Ub}}{R(n_{Ub}s_{Ub} + \pi R)}. \tag{6.43}$$

D_s is the surface diffusivity of NBR1, $\Gamma_{off,p62}$ is the rate parameter for p62 falling off NBR1, $\tilde{f}_1$ is the concentration of NBR1 with one p62, D_{p62} is the bulk diffusivity of p62, ρ_{p62} is the bulk concentration of p62, s_{NBR1} is the radius of NBR1, R is the sphere radius, $\Gamma_{off,NBR1}$ is the rate parameter for NBR1 falling off the membrane, D_{NBR1} is the bulk diffusivity of NBR1, ρ_{NBR1} is the bulk concentration of NBR1, s_{Ub} is the radius of ubiquitin, and n_{Ub} is the number of ubiquitin on the sphere.

We want to determine the growth of a cluster on the pole of the sphere, and assume azimuthal symmetry, keeping only the θ dependence of the Laplacian. $\tilde{f}_1(\theta)$ is assumed to be a constant, so that $\tilde{f}_0(\theta)$ is the only function of θ. In steady state, $d\tilde{f}_0/dt = 0$,

$$D_s\nabla^2\tilde{f}_0 = \left(\frac{\Gamma_{off,NBR1}}{R} + \frac{4\pi D_{p62}s_{NBR1}R}{N_{tot}s_{NBR1} + n_{Ub}s_{Ub} + \pi R}\right)\tilde{f}_0 - \frac{D_{NBR1}\rho_{NBR1}s_{Ub}n_{Ub}}{R(n_{Ub}s_{Ub} + \pi R)}. \tag{6.44}$$

By defining

$$a = \frac{\Gamma_{off,NBR1}}{R} + \frac{4\pi D_{p62}s_{NBR1}R}{N_{tot}s_{NBR1} + n_{Ub}s_{Ub} + \pi R}, \tag{6.45}$$

$$w = \frac{D_{NBR1}\rho_{NBR1}s_{Ub}n_{Ub}}{aR(n_{Ub}s_{Ub} + \pi R)}, \tag{6.46}$$

$$f_0 = \tilde{f}_0 - w, \tag{6.47}$$

and going to steady state, $d\tilde{f}_0/dt = 0$, we have

$$af_0 = D_s\nabla^2 f_0 = \frac{D_s}{R^2\sin\theta}\frac{\partial}{\partial\theta}\left(\sin\theta\frac{\partial f_0}{\partial\theta}\right). \tag{6.48}$$

Following the derivation in Appendix B of Brown and Rutenberg [186], equation 6.48 is solved with a hypergeometric function, and the Gibbs-Thomson boundary condition and mass balance applied to a limiting form of the hypergeometric function. This gives an equation describing the change in cluster molecule number N_{clust} in time,

$$\frac{dN_{clust}}{dt} = 4\pi aR^2\left[w - f_\infty\left(1 + \nu\sqrt{\frac{\pi}{bN_{clust}}}\right)\right]. \tag{6.49}$$

Equation 6.49 is used to determine the change in time of NBR1 clusters on peroxisomes.

6.8 Appendix D: Alternate Model Results

The dynamics of p62 chains are not well-established. Our primary model assumes the p62-p62 and NBR1-p62 bonds, which are due to interactions between PB1 domains on both proteins [103, 93], are quite strong, and only dissociate following dissociation of the NBR1 base from the membrane of the p62 base from ubiquitin. Here we explore an alternative model to determine how significant the details of p62 chain dynamics are to our results.

The alternate model allows p62 to dissociate from the end of chains, in addition to p62 chain dissociation from ubiquitin and NBR1 dissociation from the membrane. p62 dissociates from the ends of each chains of length l on NBR1 (or from each NBR1 if there is only one p62 monomer, $l = 1$) at a rate $J_{off,p62-NBR1}(l) = \Gamma_{off,p62} N_{NBR1}(l)$, where $\Gamma_{off,p62}$ is the dissociation parameter for p62 from the end of a p62 chain on NBR1, or from NBR1. p62 dissociates from the end of each chain, or the base p62 can dissociate from ubiquitin, at a rate $J_{off,p62-Ub}(l) = \Gamma_{off,p62,Ub} N_{Ub}(l)$, where $\Gamma_{off,p62,Ub}$ is the dissociation parameter for p62 from the end of a p62 chain on ubiquitin, or from ubiquitin. The change in time of NBR1 with chain length l is then

$$\begin{aligned}\frac{dN(l)}{dt} =& J_{on,NBR1}\delta_{l,0} - J_{off,NBR1}(l) + \left[J_{p62\to NBR1}(l-1) - J_{off,p62-NBR1}(l)\right](1-\delta_{l,0}) \\ &+ J_{off,p62-NBR1}(l+1) - J_{p62\to NBR1}(l).\end{aligned} \tag{6.50}$$

The change in time of the number of ubiquitin with chain length l, $N_{Ub}(l)$, is

$$\begin{aligned}\frac{dN_{Ub}(l)}{dt} =& [J_{p62\to Ub}(l-1) - (2-\delta_{l,1})J_{off,p62-Ub}(l)](1-\delta_{l,0}) \\ &+ J_{off,p62-Ub}(l+1) - J_{p62\to Ub}(l) + \delta_{l,0}\sum_{i=2}^{\infty} J_{off,p62-Ub}(i)\end{aligned} \tag{6.51}$$

For cluster growth, this model has a modified value for w:

$$w = \frac{1}{a}\left(\Gamma_{off,p62}\tilde{f}_1 + \frac{D_{NBR1}\rho_{NBR1}s_{Ub}N_{Ub}}{R(N_{Ub}s_{Ub} + \pi R)}\right), \tag{6.52}$$

Using this alternate model to find the results as in figures 6.2 - 6.5, shown in figures 6.7 - 6.10. No qualitative differences in behaviour of the system are found.

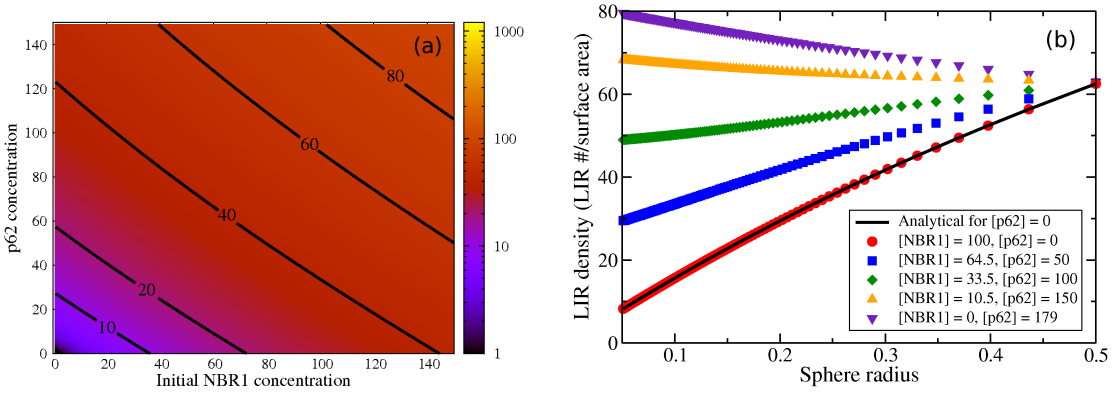

Figure 6.7: Equilibrated number of LIR-domain containing proteins with forbidden clustering. (a) System of one peroxisome, $R = 0.25\mu$m. Intensity plot shows the number of LIR-domain containing proteins, the sum of NBR1 and p62, on the peroxisome after equilibration. Initially there are zero NBR1 and p62 on the peroxisome, and the indicated initial NBR1 concentration in the bulk volume. The indicated p62 concentration is held constant. (b) System of 100 peroxisomes, with radii exponentially distributed between $R = 0.05\mu$m and $R = 0.50\mu$m. Initially there are zero NBR1 and p62 on the peroxisomes, and indicated NBR1 concentrations are the initial concentration in the surrounding bulk volume. p62 concentrations are held constant. LIR density is the number of LIR-domain containing proteins, NBR1 and p62, on a peroxisome, divided by the peroxisome surface area $4\pi R^2$. At each p62 concentration, the NBR1 concentration is varied to match the [p62] = 0 case at the maximum sphere radius. Equation 6.13 is plotted with the black line using $D\rho s n_0/\Gamma_{off} = 32.8\mu\text{m s}^{-1}$.

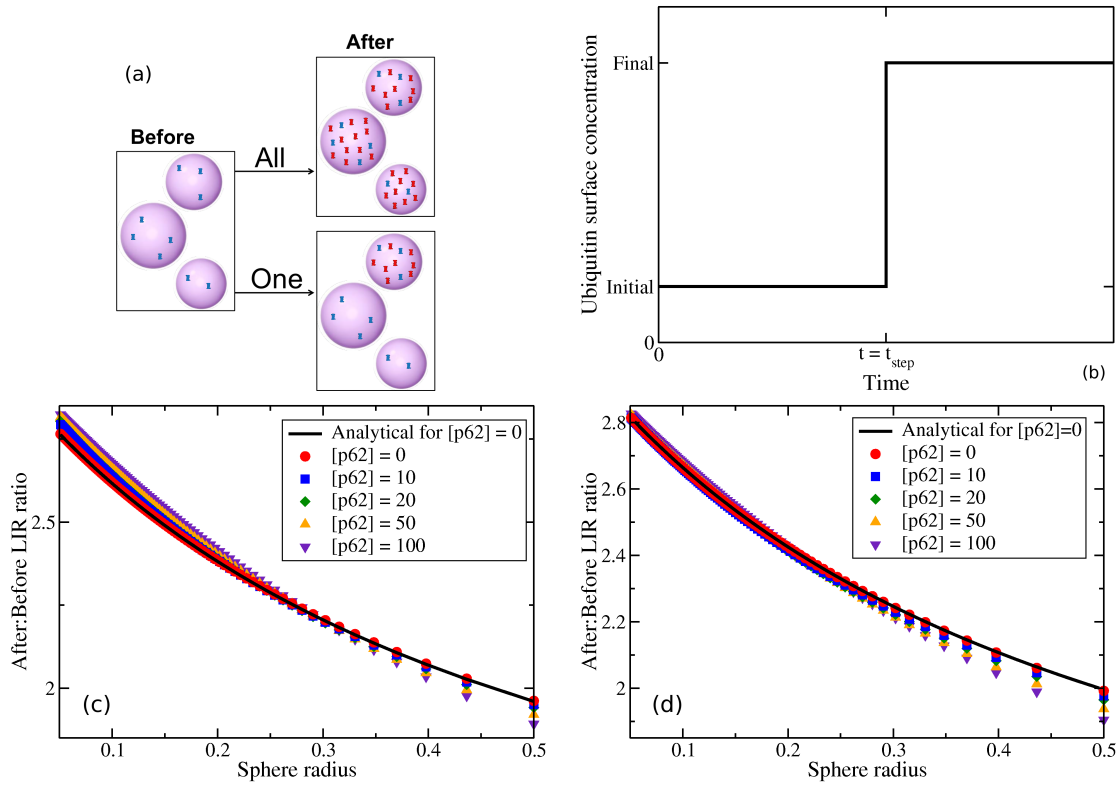

Figure 6.8: Ubiquitin increase on peroxisomes and resulting NBR1 and p62 increases. Clustering forbidden. (a) Schematic of ubiquitin level changes. Purple spheres represent peroxisomes. On left, irregular blue shapes represent ubiquitin present on peroxisomes before a ubiquitin increase. On the right, more ubiquitin is added, shown as irregular red shapes. We increase ubiquitin on all peroxisomes, as shown top right, or on a single peroxisome, shown bottom right. (b) The increase of ubiquitin is modelled as an instantaneous event. At a given time, the ubiquitin on all spheres, or a single sphere, is increased to a higher surface concentration. (c) Increases in LIR-domain containing proteins, the sum of NBR1 and p62, expressed as a ratio of after:before an increase of the ubiquitin level on all peroxisomes by a factor of three — with n_0 the ubiquitin coefficient, the number of ubiquitin on each peroxisome is $N_{Ub}(R) = n_0(R/R_0)^2$, with $R_0 = 0.25\mu$m, and before $n_0 = 100$, and after $n_0 = 300$. A system of 100 peroxisomes is used, with the radius exponentially distributed between $R = 0.05\mu$m and $R = 0.50\mu$m. The after:before LIR ratio depends on the peroxisome radius, although each curve represents a single system. Initial NBR1 concentration is $50\mu\text{m}^{-3}$, and the p62 concentration is varied as indicated. Points show numerical results, while the black line shows equation 6.19 with $\rho_f/\rho_i = 0.982$. (d) Increases in LIR numbers, expressed as a ratio of after:before an increase of ubiquitin level on individual peroxisomes by a factor of three, so that before $n_0 = 100$ and after $n_0 = 300$. 100 peroxisomes are used, with radius exponentially distributed between $R = 0.05\mu$m and $R = 0.50\mu$m. The after:before ratio depends on the peroxisome radius, but since the ubiquitin level is increased on a single peroxisome, each point represents a single system, with the curve representing 100 systems (one system for the increase on a different peroxisome). Initial NBR1 concentration is $50\mu\text{m}^{-3}$, and the p62 concentration is varied as indicated. Points show numerical results, while the black line shows equation 6.19 with ρ_f/ρ_i of unity.

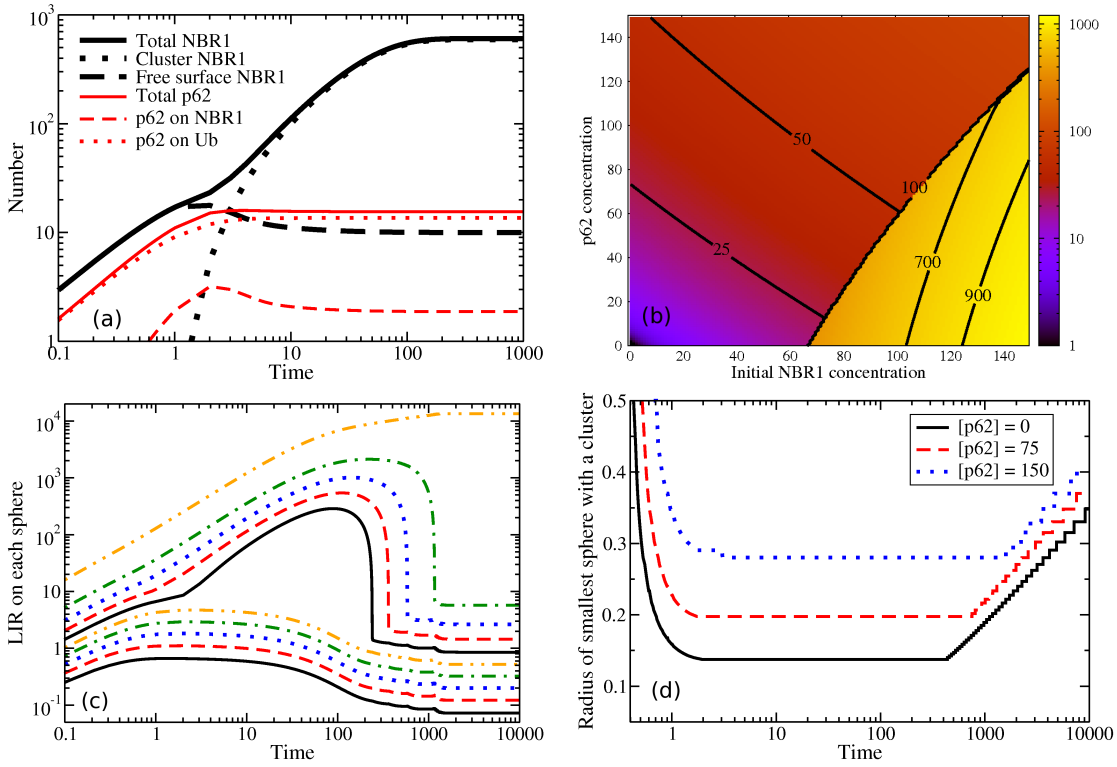

Figure 6.9: Clustering allowed. (a) One peroxisome, $R = 0.25\mu$m. Initially zero NBR1 and p62 on the peroxisome, with initial bulk [NBR1] = $100\mu\text{m}^{-3}$ and [p62] = $40\mu\text{m}^{-3}$. Time dependence of NBR1 and p62 quantities on peroxisome shown. (b) System of one peroxisome, $R = 0.25\mu$m. Intensity plot shows the equilibrium number of LIR-domain containing proteins, the sum of NBR1 and p62, on the peroxisome. Initially there is zero NBR1 and p62 on the peroxisome, and the indicated initial NBR1 concentration in the bulk volume. The indicated p62 concentration is held constant. A clear boundary separates the non-clustering region (roughly the left side, red and purple) from the clustering region (right side, yellow). (c) System of ten peroxisomes, with radii exponentially distributed between $R = 0.05\mu$m and $R = 0.50\mu$m. Initial [NBR1] = $150\mu\text{m}^{-3}$, and [p62] = 0. Each curve represents the number of NBR1 on a different peroxisome. Clusters form on five peroxisomes (top five lines), corresponding to the largest five peroxisomes. Four of the five clusters evaporate through Ostwald ripening interaction. After a cluster remains on only a single sphere, the number of LIR domains on each peroxisome changes little. (d) System of 100 peroxisomes, with radii exponentially distributed between $R = 0.05\mu$m and $R = 0.50\mu$m. Initial [NBR1] = $150\mu\text{m}^{-3}$, and p62 concentration as indicated. Initially all peroxisomes have zero NBR1 and p62. A cluster forms on the largest peroxisome first, and proceeds with formation on the next largest peroxisome until cluster formation stops. Evaporation occurs first from the smallest peroxisome with a cluster and so the size of the smallest peroxisome with a cluster is plotted against time — all peroxisomes larger than this size have a cluster, and all smaller do not have a cluster.

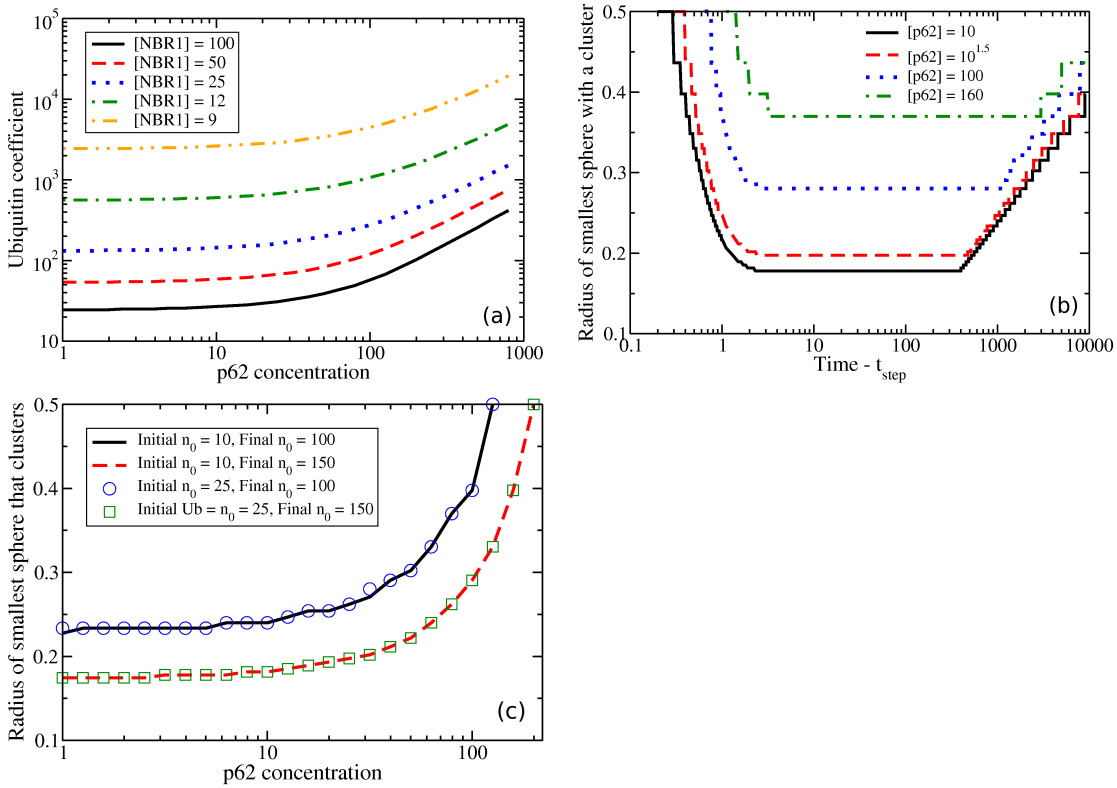

Figure 6.10: Ubiquitin increase on peroxisomes and resulting NBR1 cluster behaviour. Clustering allowed. (a) System of 100 peroxisomes, with radii exponentially distributed between $R = 0.05\mu$m and $R = 0.50\mu$m. Initially zero NBR1 and p62 on peroxisomes, initial NBR1 and p62 concentrations as indicated. With n_0 the ubiquitin coefficient, the number of ubiquitin on each peroxisome is $N_{Ub}(R) = n_0(R/R_0)^2$, with $R_0 = 0.25\mu$m. At a given initial NBR1 concentration (each curve), for each p62 concentration the ubiquitin coefficient n_0 was increased until clustering occurred, and so each curve marks the boundary between no clustering and at least one cluster. The red points mark two ubiquitin coefficients at [p62] = $100\mu\text{m}^{-3}$, and the arrow indicates an increase in the ubiquitin coefficient that would induce clustering. (b) System of 100 peroxisomes, with radii exponentially distributed between $R = 0.05\mu$m and $R = 0.50\mu$m. There is initially zero NBR1 and p62 on peroxisomes, initial [NBR1] = $80\mu\text{m}^{-3}$, and p62 concentrations as indicated. At $t = t_{step}$ the ubiquitin coefficient from $n_0 = 25$ to $n_0 = 150$. The ubiquitin increase causes cluster formation on many peroxisomes, causing an initial very rapid increase in the number of clusters, followed by cluster evaporation due to Ostwald ripening, causing a much slower reduction in number of clusters. The radius of the smallest peroxisome with a cluster, R_{min}, is plotted vs. time. (c) With the same scenario as (b), ubiquitin is increased on a single peroxisome as labelled. The initial [NBR1] = $75\mu\text{m}^{-3}$. The curves show the radius of the smallest peroxisome that forms a cluster, R_{min}. Error bars in (b) and (c) indicate the standard deviation.

Chapter 7

Discussion of Chapters 4, 5, and 6

7.1 Summary of Results

We investigated three distinct systems in chapters 4, 5, and 6.

Chapter 4 modelled the peroxisome matrix protein import system, in particular the accumulation of ubiquitin associated with import complexes. Ubiquitin labelling of peroxisomes has been shown to induce degradation of peroxisomes by autophagy [18], and we explored how the ubiquitin associated with import could provide a signal for degradation. The actual translocation of the new peroxisome matrix protein across the peroxisome membrane, as well as the energy source for this translocation, are not well understood. It has been speculated that Pex5 export could drive protein translocation. Accordingly, we modelled three types of translocation coupling: no coupling, direct coupling to export, and proposed a third type we call cooperative coupling. Our proposed translocation coupling involves two Pex5, one in the process of export from the membrane, and the other associated with the matrix protein to be translocated across the membrane, driven by the export of the other Pex5. We found that comparing no coupling and direct coupling to cooperative coupling, the ubiquitin accumulation behaved in a qualitatively distinct manner. With no coupling and direct coupling, as the production of proteins to be imported increased, the amount of ubiquitin increased. In contrast, as the protein production increased with cooperative coupling, the amount of ubiquitin decreased. The cell would be expected to need many peroxisomes when there is high production of peroxisome proteins, and need few peroxisomes when there is low protein production. Cooperative coupling of protein translocation therefore provides a signal consistent with more peroxisome degradation when peroxisomes are less needed, and less degradation when peroxisomes are more needed. The import system naturally produces the appropriate signal for the protein production level.

Chapter 5 modelled the dynamics of clusters on the surface of spherical drops.

Drops, and their harboured clusters, could interact through the inter-drop medium. Clusters on the surface of drops were found to follow Lifshitz-Slyozov-Wagner coarsening behaviour, with power law growth of the average cluster size with appropriate exponent, and dynamic scaling of the cluster size distribution. The cluster size distribution depended on the drop radius distribution in a similar way to scaling function dependence on dimension in bulk systems. The clusters evaporate from small drops, and grew on large drops, a process that continued until only a single drop harboured a cluster. Degradation of cellular substrates by autophagy is thought to be signalled by the accumulation of autophagy receptor proteins. These receptor proteins have been observed in non-overlapping microdomains surrounding autophagy substrates, with NBR1, a receptor protein for peroxisomes, a good candidate for clustering. Our results suggest NBR1 coarsening could select large peroxisomes for clusters, to be followed by degradation by the autophagy system.

Chapter 6 expands on the clustering work of chapter 5, adding cluster formation and more proteins involved in peroxisome autophagy. Ubiquitin is included to recruit NBR1 to the peroxisome membrane, as well as p62 to form chains on NBR1 and ubiquitin. NBR1 cluster formation occurs at sufficiently high NBR1 membrane concentration. NBR1 clustering on peroxisomes is shown as a possible explanation for observed all-or-none colocalization of NBR1 with catalase [19] and clusters can clearly exceed any threshold for degradation by autophagy. As in chapter 5, the NBR1 clusters also select large peroxisomes, which would lead to their degradation. In the model, p62 chains on NBR1 cannot participate in cluster formation or growth due to steric repulsion. This leads p62 to increase selectivity, decreasing the number of clusters and limiting clusters to even larger peroxisomes. Increasing the ubiquitin level on peroxisomes can allow a system without clusters to accumulate sufficient NBR1 on peroxisomes for cluster formation, tying back to the results of chapter 4. Selection of fewer, but larger, peroxisomes for degradation could lead to a greater reduction in peroxisome volume compared to less selective degradation of peroxisomes of all sizes.

7.2 Chapter 4

In chapter 4 we propose an alternative coupling model to drive peroxisome matrix protein translocation across the peroxisome membrane, and argue that our model

provides a reasonable ubiquitin signal to control autophagy for disuse.

This directly connects to the theme of self-regulation presented in chapter 1. With our model, and assuming our cooperative coupling hypothesis from chapter 1, the routine matrix protein import process can naturally provide a signal for peroxisome degradation by autophagy. Low cargo traffic leads to a high ubiquitin signal, and high cargo traffic to a low ubiquitin signal. Ubiquitin is known to induce pexophagy, and the cell is expected to provide matrix protein cargo when it requires peroxisomes. This mechanism does not exclude external signals for peroxisome degradation, but rather provides a degradation signal. Here I emphasize that this organization of the degradation signal is in time, deciding when peroxisomes should be degraded.

In the model, the change in the ubiquitin level of the system is only due to changes in the amount of Pex5 cargo — the number of peroxisomes, importomers, Pex5, export complexes, as well as the concentration of ubiquitination enzymes remain unchanged.

The model of chapter 4 provides a disuse signal for peroxisome degradation, to control peroxisome numbers. However, peroxisome degradation could be due to damage, a possibility brought up later in chapter 6. How might the model of chapter 4 mediate degradation due to damage, allowing the ubiquitin level to rise on a damaged peroxisome? A probable source for damage on a peroxisome would be reactive oxygen species inside peroxisomes. Any damage that inhibited the import of more catalase to deal with peroxide would likely lead to further peroxisome damage. Damaged docking proteins would prevent the docking of additional Pex5, which would lead to a ubiquitinated Pex5 stranded at an importomer. A damaged export complex would lead to more ubiquitinated Pex5 stranded on an importomer. In contrast, a damaged RING complex would lead to less ubiquitinated Pex5 in the short term. If a damage level was non-specific and rising, it seems plausible that it could lead to less Pex5 arrival and fewer docking complexes, which would be followed by an elevated ubiquitin level. The same pathway for a high ubiquitin signal from disuse does not appear to be ruled out for generating a ubiquitin signal for damage.

In chapter 4 we do not include all proteins and other factors that may be relevant, instead focusing on a core model. Below we outline some limitations of our chosen model.

In chapter 4 ubiquitin is the only pexophagy-inducing molecule discussed. In later

chapters we introduced the role of autophagy receptor proteins NBR1 and p62, but here we briefly explain how they connect. Both p62 and NBR1 have UBA domains that can bind ubiquitin. NBR1 also has a J domain to stick to peroxisome membranes, while p62 will simply bind to ubiquitin. The UBA domains allow high levels of ubiquitin on peroxisomes to recruit more NBR1 and p62 to peroxisome membranes. NBR1 and p62 are then able to interact with proteins of the autophagy system to recruit an autophagosome, leading to degradation.

In chapter 4 we do not include polydisperse peroxisomes — they all have the same radius. First, the story is complete without size effects for peroxisomes. We can show how Pex5 and ubiquitin behave without the polydispersity. To address peroxisome size effects we must use a dependence of importomer and export complex numbers on the peroxisome radius, which is unknown. Despite not addressing size effects in chapter 4, they play a central role in chapters 5 and 6.

In chapter 4 we do not include polyubiquitination because we do not expect it to change the behaviour of the system as peroxisome matrix protein traffic is changed. While this is not an unreasonable assumption, it may not be perfect, and there may be situations where polyubiquitination could do more than perturb results. For example, the high ubiquitin signal relies on monoubiquitinated Pex5 waiting for other Pex5 to arrive. During this waiting period, it is possible that the Pex5 could be polyubiquitinated, attenuating any disuse signal. It is also possible that the configuration or binding partners of Pex5 following monoubiquitination could prevent polyubiquitination.

The ubiquitin level on peroxisomes is similar to a repressing genetic network. At very low cargo protein production the ubiquitin level is high, and does not change with further decreases in cargo protein production. At high cargo protein production, the ubiquitin level is low, and does not decrease with further increases in cargo protein production. This is similar to repression in protein expression, which can lead to switch-like behaviour in the expression of the repressed protein [207]. In our peroxisome system, we can make an analogy of the number of ubiquitin on Pex5 with the expression of the repressed protein and cargo protein production with the expression of the repressor protein.

7.3 Chapter 5

In chapter 5 we investigated the dynamics of clusters on the surface of spherical drops which interact through the bulk medium, looking at the coarsening behaviour as well as how drops are selected for growing clusters at later times.

Chapter 5 addresses our hypothesis of self-regulation, presented in chapter 1. Clusters on larger drops are selected for growth, suggesting the autophagy receptor protein clusters may similarly select larger peroxisomes, labelling the large peroxisomes for degradation. Following the discussion of section 7.2, this size selection mechanism does not exclude external signals, but instead allows selection without external signals. In contrast to section 7.2, where the organization of the degradation signal was in time, here the clustering behaviour organizes the autophagy signal between substrates. Also, as mentioned in section 7.2, the investigation of the ubiquitin response in chapter 4 did not explore the effect of peroxisome size. In contrast, chapter 5 very explicitly addresses peroxisome size.

Degradation of substrates by the autophagy system was only recently found to be selective, and basic understanding of how autophagy selects substrates is developing. Much of the focus has been on how autophagy selects different substrate types, for example peroxisomes rather than mitochondria [6]. This substrate-type selectivity is thought to be controlled by autophagy receptor proteins, which can interact with both the substrate and the autophagy system. The receptor proteins or their combinations can label different substrate types for degradation. It is not typical for many of the substrates of the autophagy system to be entirely absent from a cell, and therefore rare for the autophagy system to degrade the entire population of a substrate. The autophagy system must be capable of selection within a substrate type, and we have investigated how some peroxisomes could be selected for degradation, but not other peroxisomes. We have shown that coarsening clusters on the surface of spherical drops evaporate from small drops and grow on larger drops. This suggests that clusters of NBR1, an autophagy receptor protein for peroxisomes, could localize to larger peroxisomes. This would select larger peroxisomes for degradation by autophagy, rather than smaller peroxisomes.

Missing from chapter 5 is cluster formation, as the clusters are simply assumed to be present on the spheres as an initial condition. This is addressed in chapter 6, which

includes cluster formation and explores how it affects which peroxisomes clusters form on. Chapter 5 also takes the idealization of NBR1 clusters to an extreme, with no other cellular context. Chapter 6 will connect back to the ubiquitin signal of chapter 4, and will also include a second receptor protein, p62.

There is evidence that large peroxisomes can be selected earlier for degradation [171], and that degradation mode can depend on peroxisome size [85]. But what could a cell gain by removing big peroxisomes first? I suggest it could be that big peroxisomes are older, have more broken proteins, and are less effective at performing the reactions necessary for their cellular role. A significant amount of membrane proteins are trafficked to existing peroxisomes through the ER, along with lipids [65]. As peroxisomes gain membrane proteins and membrane lipids, they will increase in size. Peroxisome matrix proteins only have an import system, and no path to escape the peroxisome matrix. Lack of exchange of matrix proteins between peroxisomes has been used to rule out peroxisome fusion [20], but also suggests that matrix proteins do not leave the peroxisome matrix once imported. Both the gain of lipids with membrane proteins and the lack of escape for matrix proteins suggests older peroxisomes are larger. A fraction of the peroxisome population is unable to import new matrix proteins, thought to indicate age-related defects [20], suggesting old peroxisomes are less functional. The presence of reactive oxygen species inside peroxisomes [14] and the lack of inheritance of matrix proteins to newly budding peroxisomes [20, 73] suggests that matrix proteins can be damaged. Membrane proteins are also asymmetrically divided between the mother peroxisome and the new, budding peroxisome [73, 75, 76], which has been suggested to allow the new peroxisome to take functional proteins, and the older peroxisome to retain damaged proteins [76]. Given that older peroxisomes are likely larger, the fraction of peroxisomes that are not import-competent, and the buildup of broken matrix and membrane proteins, it does not seem unreasonable that larger peroxisomes are less functional, and may be an appropriate target for selective degradation. Any test of this reasoning would likely be indirect, as there is no direct assay of peroxisome damage.

Clusters on spherical drops were found to follow Lifshitz-Slyozov-Wagner coarsening dynamics: the average number of particles in the clusters grew as a power law with exponent 2/3 (consistent with a power law for radius with exponent 1/3), and

the cluster size distribution collapsed to a single function when scaled by the average cluster size. The cluster size scaling function was found to depend on the drop radius distribution, introducing drop polydispersity as a characteristic that can vary the cluster size scaling function similar to dimension in bulk systems. The scaling functions for the clusters on drops was found to qualitatively better resemble the two-dimensional bulk scaling function, compared to the three-dimensional bulk scaling function. This suggests that systems of clusters on drops are more influenced by the two-dimensional surface dynamics, rather than the three-dimensional medium connecting the drops.

7.4 Chapter 6

In the chapter 6 we explored a model for NBR1 cluster formation and dynamics on peroxisomes. This model includes ubiquitin to recruit NBR1 to the peroxisome membrane, and p62 chain formation on both NBR1 and ubiquitin — on NBR1, these chains inhibit cluster formation and growth, and on ubiquitin the chains prevent NBR1 recruitment.

The investigation of chapter 6 was similar to that of chapter 5, with both examining cluster dynamics on spherical drops, motivated by segregated domains of autophagy receptor proteins. As before, the NBR1 clusters select larger peroxisomes for cluster growth, and smaller peroxisomes for cluster evaporation, leading to selection of larger peroxisomes for degradation by the autophagy system. Ubiquitin recruits NBR1 to the membrane, and serves as a base for p62 chain formation. Increases in the ubiquitin level lead to increases in the surface NBR1 concentration and possibly NBR1 cluster formation. p62 chains on NBR1 prevent NBR1 from participating in cluster formation or cluster growth, leading to p62 inhibition of cluster formation. Increasing p62 levels allowed fewer NBR1 clusters, which selected the largest peroxisomes even more tightly than systems with only NBR1.

Chapter 6 and chapter 5 connect to our hypothesis in chapter 1 in a similar way, as the theme of self-regulation is again raised. As before, self-regulation of the selection of peroxisomes for degradation is through the selection of larger peroxisomes by NBR1 clusters. This selection has added complexity with the enhanced selectivity with p62, the switch from a state without clusters to a state with clusters when ubiquitin levels

are sufficiently increased, and the introduction of cluster formation. NBR1 cluster selection of larger peroxisomes is self-regulating because the cell simply must provide NBR1 in sufficient concentration and clusters will form on large peroxisomes and coarsen to even larger peroxisomes. The cell simply must provide p62 to cause tighter selection of larger peroxisomes. Tying back to chapter 4, the cell simply can reduce the production of peroxisome matrix proteins and the ubiquitin level will rise of its own accord. The rise in ubiquitin will be followed by corresponding increases in the NBR1 concentrations on peroxisome membranes, cluster formation on large peroxisomes, and coarsening of clusters to the largest peroxisomes with clusters. Overall the cell simply provides proteins with certain properties and the selection can occur without further direction. However, the possibility of selection of large peroxisomes does not rule out specific signals or proteins from the cell that do select peroxisomes for degradation, on the basis of size or otherwise.

In chapter 5, size selection was only through coarsening of existing clusters, while chapter 6 shows that there is also size selection in cluster formation. Notably, the size selection during cluster formation is orders of magnitude faster than during coarsening. Chapter 6 was also able to investigate the difference between a deproliferation ubiquitin signal for degradation, occurring on all peroxisomes, and a damage ubiquitin signal, occurring on a single peroxisome. A key difference between these two types of ubiquitin signalling is that deproliferation induces many clusters, which will compete and coarsen, while damage induces a single cluster that does not compete and will not evaporate once formed.

In section 7.3 the possibility was raised that the cell could prefer to degrade large peroxisomes because they may not be as functional as younger, smaller peroxisomes. In chapter 6, a second possibility was raised: selection of large peroxisomes for degradation more greatly reduces peroxisome volume for each peroxisome degraded. In chapter 6 this is suggested as one way that observations of catalase fluorescence intensity with and without p62 knockdown could be explained. A more effective reduction of peroxisome volume and therefore a reduction of the metabolic potential of the peroxisome population, rather than reduction of peroxisome number, could also be a cellular goal. Peroxisomes play an important role in controlling cellular reactive oxygen species, which can cause cellular damage, but also can serve as signalling

molecules [14]. Eliminating ineffective large peroxisomes could allow resource recovery without a significant increase in reactive oxygen species, or removing effective large peroxisomes could increase reactive oxygen species so they can participate in other activities such as signalling. These considerations do not seem mutually exclusive from the efficiency argument of section 7.3, or each could occur when appropriate.

Another question raised by the result of chapter 6 is why the cell would benefit from the tighter size regulation for degradation of large peroxisomes brought on by p62. Without p62, the cell could simply decrease the amount of NBR1 to cause fewer clusters on larger peroxisomes, if tighter selection was the only goal. It may be that modelling dynamic peroxisome numbers, along with the depletion of autophagy receptor proteins as the organelles are degraded, is necessary to understand this aspect of the roles of NBR1 and p62.

Within our model, p62 chains on NBR1 inhibit NBR1 cluster formation and growth. This leads to tighter selection of large peroxisomes for NBR1 clusters and degradation by the autophagy system. In chapter 6, we suggest that selective degradation of large peroxisomes leads to a greater reduction of peroxisome volume, and that p62 could push the system towards this extreme, away from less selective degradation. This could be an alternative explanation for the observed increase in catalase fluorescence intensity when p62 is knocked down, which suggests that there are more peroxisomes and less pexophagy [19]. Instead, the p62 knockdown leads to less strict selection of large peroxisomes for degradation, resulting in an increase of peroxisomal volume over time. I would like to emphasize that there are other possibilities, although these possibilities are, to my knowledge, not put forward in the current literature, with or without support. p62 chain formation could be more effective at recruiting autophagosomes, leading to more pexophagy per LIR for p62 compared to NBR1. NBR1 clusters could incorporate NBR1 with p62 chains, without p62 inhibition of clustering. This would lead to more LIRs present with p62 compared to an NBR1-only system (this possibility was not explored in chapter 6 because it is not expected to significantly affect selectivity and it presents an entire new set of modelling challenges).

7.5 Further Discussion

With the explicit inclusion in the model of ubiquitin to recruit NBR1, chapter 6 directly relates to the ubiquitin narrative of chapter 4. The ubiquitin level increases of chapter 6 tie in to the ubiquitin increases from decreased peroxisome matrix protein production in chapter 4. In a situation where the cell significantly decreased the production of peroxisome matrix proteins, the ubiquitin associated with Pex5 would quickly increase as the existing pool of matrix protein in the cytosol was depleted through import into peroxisomes. This would be followed by NBR1 cluster formation and degradation of peroxisomes with clusters by autophagy. The decrease in peroxisome numbers could push the ubiquitin level down to a level that no longer induces NBR1 cluster formation, leading to the peroxisome number regulation brought up in chapter 4. NBR1 clusters also allow the conversion of a graded ubiquitin increase due to graded peroxisome matrix protein production into an all-or-none presence or absence of a cluster on a smaller number of peroxisomes, allowing rapid autophagy response with only a small overall autophagy rate.

In chapter 6 the colocalization of NBR1 and catalase is addressed. The NBR1 and catalase colocalization in Figure 5 of Deosaran *et al.* [19] appears in an all-or-none manner, with many catalase puncta with little NBR1 colocalization, and puncta with significant NBR1 colocalization. In chapter 6 we argue that this observation is difficult explain without NBR1 clusters, but simple to explain with NBR1 clusters. Additionally, although it is not quantified, in Figure 2B of Deosaran *et al.* [19] the NBR1 appears to significantly colocalize on larger region of catalase fluorescence. This suggests that NBR1 is on the large peroxisomes, rather than the small peroxisomes.

Park *et al.* [208] investigated the aggregation of p62 and NBR1 on vesicles harbouring EDEM1 proteins from the endoplasmic reticulum. They found that p62 and NBR1 aggregate colocalized with EDEM1, selecting the vesicles for degradation by autophagy. The aggregates appear to be approximately 10 nm in size. This is the size range expected for NBR1 clusters on peroxisomes.

Cemma *et al.* [9] argues that they have shown that autophagy receptor proteins p62 and NDP52 form microdomains, and Park *et al.* [208] observes p62 in tight aggregates. p62 [97] and NDP52 [209] are not thought to have membrane binding domains. Due to the lack of direct observation of NBR1 domains or clusters on

membranes, we have used the membrane binding of the 'J' domain of NBR1 to argue that NBR1 is a good candidate for clustering on peroxisome membranes. However, the domain-forming and aggregation behaviour of p62 and NDP52 suggest that domain and cluster formation on membranes and other surfaces may not require a membrane binding domain, and that clustering may be more general.

So far we only have suggestions that NBR1 can cluster on membranes and use clustering to select larger substrates. MAVS (also known as CARD or IPS) proteins on mitochondria and peroxisomes play a role in the cellular anti-viral response [210]. Before viral infection, MAVS are not activated, and are spread out on the mitochondrial membrane [211]. Upon viral infection MAVS are activated, and activated MAVS cluster on the mitochondrial membrane [211, 212]. It has been shown that in cells without viral infection, MAVS is evenly distributed between mitochondria [213]. However, in cells that have been infected, some mitochondria have significant MAVS while other mitochondria have little to no MAVS [213]. Additionally, although the data is limited it suggests that large mitochondria retain MAVS while small mitochondria do not [213]. These observations suggest that MAVS clusters may form on and/or coarsen to larger substrates. This is similar to our modelled behaviour of NBR1 cluster formation and growth selecting large peroxisomes and its circumstantial support.

7.6 Experimental Tests

In this section I suggest some experimental tests that may help evaluate our hypotheses.

7.6.1 Chapter 4

In chapter 4, our key prediction is that with cooperative coupling, at low cargo traffic there will be a high ubiquitin signal, and at high cargo traffic there will be a low ubiquitin signal. After peroxisome proliferators are introduced the cargo traffic is expected to be high, as the number of peroxisomes is increasing, and conversely when proliferators are removed or application stopped cargo traffic is expected to be low as the number of peroxisomes is decreasing. These two situations would be appropriate times to measure the amount of ubiquitinated Pex5. Detection of

ubiquitinated Pex5 has been done [141] and in principle a similar measurement could be performed for the two suggested situations. With cooperative coupling we would expect less ubiquitinated Pex5 following removal of peroxisome proliferators compared to following the application of proliferators.

Although much is known about the structure of the peroxisome matrix protein importomer, there are significant gaps in understanding, and filling these gaps could narrow the possibilities for the actual mechanism of cargo protein translocation. Cryoelectron tomography has been used to help determine the structure of the nuclear pore complex [214] and the type IV secretion system of gram negative bacteria [215], both of which are protein structures associated with membranes. These experiments suggest cryoelectron tomography of peroxisome importomers is possible, and may even reveal some dynamics as in the case of the nuclear pore [214]. For example, a successful cryoelectron tomography investigation may more conclusively show that all importomers are associated with Pex5 or not, or could catch Pex5, Pex14, and/or other proteins forming a translocation channel.

Limited measurements of an *in vitro* system of importomers embedded in a planar lipid membrane have been performed [43], focusing on conductance of the system of importomers. Including ATP and ubiquitin with such a system, and considering systems with key proteins modified or missing could provide circumstantial evidence of importomer operation. For example, removing ubiquitin from the system would be expected to eliminate translocation of cargo proteins as Pex5 would be unable to export and drive translocation.

7.6.2 Chapters 5 and 6

We have hypothesized the existence of NBR1 clusters and there is circumstantial evidence for their existence, but direct observation would be much stronger. NBR1 has been fluorescently labelled in living cells and observed to colocalize with peroxisomal proteins [19]. Super-resolution microscopy can achieve resolutions of 30-60 nm on membranes [216], suggesting that a super-resolution microscopy investigation of NBR1 localization on peroxisomes would be able to distinguish clusters from other possibilities.

Fluorescent labelling of peroxisomes could be used to track which peroxisomes are

degraded, using fluorescence intensity as a proxy for peroxisome size. An experiment could observe which peroxisomes are degraded (fluorescence disappearing) or which peroxisomes colocalize with proteins present in autophagosomes. Such an investigation may be able to determine whether and how peroxisomes are degraded based on their size. If a size effect could be observed, then a knockdown of p62 similar to the p62 knockdown in Figure 1B of Ref. [19], could then determine any effect on the size selection of peroxisomes for degradation.

Our hypothesis in chapter 6 is that p62 oligomerization on peroxisome membrane-attached NBR1 inhibits NBR1 clustering. To test this mechanism, the PB1 domain of NBR1 could be modified so that it now longer binds to the PB1 domain of p62. This would prevent p62 chains from forming on NBR1, which could manifest itself as a change in the catalase intensity seen in an experiment similar to Figure 1B of Ref. [19] or in a peroxisome size selection through fluorescence intensity, as described above. This test would rely on the modification of the PB1 domain of NBR1 not leading to other significant effects in the cell which overwhelm the desired effect.

Chapter 8

Conclusion and Future Outlook

In this thesis we have developed quantitative models for two processes related to the autophagy of peroxisomes. The first is the accumulation of the protein ubiquitin on peroxisomes as part of peroxisome matrix protein import. The second is the formation and dynamics of clusters of the autophagy receptor protein NBR1 on peroxisomes, including interactions with a second receptor protein, p62, and changes in ubiquitin level.

8.1 Connection to Overall Themes

The results all support the self-regulation of peroxisome autophagy signalling.

Chapter 4 demonstrates how the ubiquitin level on the matrix protein import machinery of peroxisomes naturally rises to signal for an increase in autophagy, or falls to signal for a decrease in autophagy, as the production of peroxisome matrix proteins decreases or increases respectively. This response organizes the degradation of peroxisomes by autophagy in time. All that is required is the peroxisome matrix protein import system and variation of peroxisome matrix protein production.

Chapter 5 shows coarsening clusters on the surface of spherical drops will select clusters on large peroxisomes for growth, and clusters on small peroxisomes for evaporation. This suggests NBR1 clusters will select large peroxisomes for degradation over small peroxisomes, which organizes the selection of peroxisomes for degradation. The cell simply needs to provide NBR1 to form the clusters for our selection mechanism to occur.

Chapter 6 adds detail to the clustering system of chapter 5 by including cluster formation, p62 chains, and ubiquitin. The results show that cluster formation, in addition to the cluster growth/evaporation of chapter 5, will also select large peroxisomes. p62 further enhances the selection of large peroxisomes. NBR1 and p62 together organize the selection of large peroxisomes. Initially, ubiquitin recruits NBR1

to the peroxisome membrane. This relates the ubiquitin signal, which organizes in time, to the NBR1 clustering to induce autophagy, so the organization of peroxisome degradation signalling in time and the organization of the selection of distinct peroxisomes are connected.

Overall, we demonstrate how the peroxisome matrix protein import system and the peroxisome autophagy receptor proteins can organize timing and selection of peroxisome degradation. However, this does not rule out direction of peroxisome degradation by systems external to peroxisomes and their associated proteins.

The assumed clustering dynamics of NBR1 are also crucial to the organization of peroxisome degradation selection.

8.2 Future Directions

8.2.1 For Work from Chapter 4

In chapter 4 the number and components of importomers on each peroxisome are static. It may be interesting to include a model of dynamic importomer formation, with subcomplexes of the importomer (e.g. Pex14 and other docking proteins, the RING complex) able to move independently and join together to form a complete importomer, and split apart and join other importomers. Such a model could be guided by current and future biochemical evidence of peroxisome membrane protein complex mass and the stability of different membrane proteins. This may be able to produce different average numbers of Pex5 sites depending on the subcomplex concentrations and details of the model, so that the number of sites does not need to be imposed.

The model of chapter 4 assumed that Pex5 instantly found any available matrix proteins, and that the concentration of these molecules was the same for all peroxisomes. A more realistic diffusion scenario could be explored, with a spatial concentration field, sources of matrix protein symbolizing ribosomes, or even mRNA diffusing from the nucleus and finishing translation so that sources could turn on and off. This could smooth out any sharpness in the data, lead a better estimate of the amount of Pex5 and matrix proteins that are on/in the peroxisome at a given time, and allow an investigation into how peroxisome localization may affect matrix protein

import and the buildup of Pex5 or ubiquitin.

In chapter 4 all peroxisomes are the same size. Ensembles with polydisperse peroxisomes could be studied to determine how the ubiquitin levels might vary with peroxisome size. Chapters 5 and 6 very directly confront size effects, and they likely could play a role in the type of modelling from chapter 4.

8.2.2 For Work from Chapter 5

In chapter 5 we apply the standard Lifshitz-Slyozov-Wagner assumption of a uniform concentration field outside clusters. A spatial concentration field between peroxisomes could be explored. This could alter the timescale of the coarsening process, as diffusion in the bulk between drops which retain clusters would take longer as fewer clusters remain. It could also better inform how evaporating clusters quantitatively evaporate and how recently evaporated material distributes, as an evaporating cluster may locally elevate the bulk concentration.

The diffusion field on the surface of peroxisomes is assumed to equilibrate rapidly in comparison to the rate of arrival and dissociation of molecules to and from the surface. This ensures a single cluster and allows a steady-state diffusion field. Investigating a more slowly adjusting diffusion field could lead to multiple clusters on a single drop. It is possible this could significantly affect the results, even if all drops with multiple clusters eventually resolve into only a single cluster.

Clustering material is conserved, and could be allowed to degrade or be produced. Drops, and the clustering molecules they harbour, could be removed or added to the system to determine how the coarsening behaviour and drop selection may be altered. These possibilities could be used to address protein production and degradation, or peroxisome division/formation and degradation. For example, degrading proteins in a cluster could be proportional to cluster size, and would push large clusters towards decreasing in size more than small clusters.

8.2.3 For Work from Chapter 6

In chapter 6 the ubiquitin levels on the peroxisomes are set by hand, but in chapter 4 the ubiquitin levels are determined by the matrix protein import system. These two models could be combined to allow the ubiquitin levels in chapter 6 to respond to

matrix protein import. This could allow determination of an overall timescale, from the decrease in the production of peroxisome matrix proteins to the formation of the first NBR1 clusters during deproliferation.

A significant question in chapter 6 is when peroxisomes might be degraded as they accumulate NBR1 and p62. Removing peroxisomes and their associated proteins from the system when they are thought to be surrounded by the autophagosome could significantly alter the dynamics. NBR1 and p62 production could be added to the system, especially if peroxisomes were being removed.

I think all of the ideas above would present significant modelling, calculation, and/or computational challenges, and would not be trivially adopted.

Bibliography

[1] I. Stewart. *Life's other secret.* John Wiley, New York, 1998.

[2] C. He and D. J. Klionsky. Regulation mechanisms and signaling pathways of autophagy. *Annu. Rev. Genet.*, 43:67–93, 2009.

[3] R. Mathew, V. Karantza-Wadsworth, and E. White. Role of autophagy in cancer. *Nat. Rev. Cancer*, 7:961–967, 2007.

[4] R. A. Nixon. The role of autophagy in neurodegenerative disease. *Nat. Med.*, 19:983–997, 2013.

[5] G. M. Fimia, G. Kroemer, and M. Piacentini. Molecular mechanisms of selective autophagy. *Cell Death Differ.*, 20:1–2, 2013.

[6] V. Rogov, V. Dotsch, T. Johansen, and V. Kirkin. Interactions between autophagy receptors and ubiquitin-like proteins form the molecular basis for selective autophagy. *Mol. Cell*, 53:167–178, 2014.

[7] W-D. Le and Z-H. Qin. New horizon in autophagy research. *Acta Pharmacol. Sin.*, 34:583–584, 2013.

[8] C. Kraft, M. Peter, and K. Hofmann. Selective autophagy: ubiquitin-mediated recognition and beyond. *Nat. Cell Biol.*, 12:836–841, 2010.

[9] M. Cemma, P. K. Kim, and J. H. Brumell. The ubiquitin-binding adaptor proteins p62/SQSTM1 and NDP52 are recruited independently to bacteria-associated microdomains to target Salmonella to the autophagy pathway. *Autophagy*, 7:341–345, 2011.

[10] P. Wild, H. Farhan, D. G. McEwan, S. Wagner, V. V. Rogov, N. R. Brady, B. Richter, J. Korac, O. Waidmann, C. Choudhary, V. Dotsch, D. Bumann, and I. Dikic. Phosphorylation of the autophagy receptor optineurin restricts *Salmonella* growth. *Science*, 333:228–233, 2011.

[11] J. J. Smith and J. D. Aitchison. Peroxisomes take shape. *Nat. Rev. Mol. Cell Biol.*, 14:803–817, 2013.

[12] E. H. Hettema and A. M. Motley. How peroxisomes multiply. *J. Cell Sci.*, 122:2331–2336, 2009.

[13] J. Ezaki, E. Kominami, and T. Ueno. Peroxisome degradation in mammals. *IUBMB Life*, 63:1001–1008, 2011.

[14] M. Islinger, S. Grille, and H. D. Fahimi. The peroxisome: an update on mysteries. *Histochem. Cell Biol.*, 137:547–574, 2012.

[15] Y. Fujiki, Y. Matsuzono, T. Matsuzaki, and M. Fransen. Import of peroxisomal membrane proteins: the interplay of Pex3p- and Pex19p-mediated interactions. *Biochim. Biophys. Acta*, 1763:1639–1646, 2006.

[16] R. Rucktaschel, W. Girzalsky, and R. Erdmann. Protein import machineries of peroxisomes. *Biochim. Biophys. Acta*, 1808:892–900, 2011.

[17] N. A. Bonekamp, S. Grille, M. J. Cardoso, M. Almeida, M. Aroso, S. Gomes, A. C. Magalhaes, D. Ribeiro, M. Islinger, and M. Schrader. Self-interaction of human Pex11pβ during peroxisomal growth and division. *PLOS One*, 8:e53424, 2013.

[18] P. K. Kim, D. W. Hailey, R. T. Mullen, and J. Lippincott-Schwartz. Ubiquitin signals autophagic degradation of cytosolic proteins and peroxisomes. *Proc. Natl. Acad. Sci. USA*, 105:20567–20574, 2008.

[19] E. Deosaran, K. B. Larsen, R. Hua, G. Sargent, Y. Wang, S. Kim, T. Lamark, M. Jauregui, K. Law, J. Lippincott-Schwartz, A. Brech, T. Johansen, and P. K. Kim. NBR1 acts as an autophagy receptor for peroxisomes. *J. Cell Sci.*, 126:939–952, 2013.

[20] S. J. Huybrechts, P. P. van Veldhoven, C. Brees, G. P. Mannaerts, G. V. Los, and M. Fransen. Peroxisome dynamics in cultured mammalian cells. *Traffic*, 10:1722–1733, 2009.

[21] P. K. Kim, R. T. Mullen, U. Schumann, and J. Lippincott-Schwartz. The origin and maintenance of mammalian peroxisomes involves a de novo PEX16-dependent pathway from the ER. *J. Cell Biol.*, 173:521–532, 2006.

[22] F. Ikeda, N. Crosetto, and I. Dikic. What determines the specificity and outcomes of ubiquitin signaling? *Cell*, 143:677–681, 2010.

[23] H. Wang, N. S. Wingreen, and R. Mukhopadhyay. Self-organized periodicity of protein clusters in growing bacteria. *Phys. Rev. Lett.*, 101:218101, 2008.

[24] R. Kollar, K. Bodova, J. Nosek, and L. Tomaska. Mathematical model of alternative mechanism of telomere length maintenance. *Phys. Rev. E*, 89:032701, 2014.

[25] P. Verbruggen, T. Heinemann, E. Manders, G. von Bornstaedt, R. van Driel, and T. Hofer. Robustness of DNA repair through collective rate control. *PLoS Comput. Biol.*, 10:e1003438, 2014.

[26] R. Saraya, A. M. Krikken, M. Veenhuis, and I. J. van der Klei. Peroxisome reintroduction in *Hansenula polymorpha* requires Pex25 and Rho1. *J. Cell Biol.*, 193:885–900, 2011.

[27] H. R. Waterham and M. S. Ebberink. Genetics and molecular basis of human peroxisome biogenesis disorders. *Biochim. Biophys. Acta*, 1822:1430–1441, 2012.

[28] F. Fanelli, S. Sepe, M. D'Amelio, C. Bernardi, L. Cristiano, A. Cimini, F. Cecconi, M. P. Ceru, and S. Moreno. Age-dependent roles of peroxisomes in the hippocampus of a transgenic mouse model of Alzheimer's disease. *Mol. Neurodegener*, 8:8, 2013.

[29] A. Lobo da Cunha, C. Batista, and E. Oliveira. The peroxisomes of the hepatopancreas in marine gastropods. *Biol. Cell*, 82:67–74, 1994.

[30] V. D. Antonenkov, R. T. Sormunen, and J. K. Hiltunen. The rat liver peroxisomal membrane forms a permeability barrier for cofactors but not for small metabolites in vitro. *J. Cell Sci.*, 117:5633–5642, 2004.

[31] S. Reumann, E. Maier, H. W. Heldt, and R. Benz. Permeability properties of the porin of spinach leaf peroxisomes. *Eur. J. Biochem.*, 251:359–366, 1998.

[32] V. D. Antonenkov, A. Rokka, R. T. Sormunen, R. Benz, and J. K. Hiltunen. Solute traffic across mammalian peroxisomal membrane - single channel conductance monitoring reveals pore-forming activities in peroxisomes. *Cell. Mol. Life Sci.*, 62:2886–2895, 2005.

[33] S. Grunau, S. Mindthoff, H. Rottensteiner, R. T. Sormunen, J. K. Hiltunen, R. Erdmann, and V. D. Antonenkov. Channel-forming activities of peroxisomal membrane proteins from the yeast *Saccharomyces cerevisiae*. *FEBS J.*, 276:1698–1708, 2009.

[34] B. Fournier, J. A. M. Smeitink, L. Dorland, R. Berger, J. M. Saudubray, and B. T. Poll-The. Peroxisomal disorders: a review. *J. Inher. Metab. Dis.*, 17:470–486, 1994.

[35] A. Volkl, E. Baumgart, and H. D. Fahimi. Localization of urate oxidase in the crystalline cores of rat liver peroxisomes by immunocytochemistry and immunoblotting. *J. Histochem. Cytochem.*, 36:329–336, 1988.

[36] P. B. Lazarow and Y. Fujiki. Biogenesis of peroxisomes. *Annu. Rev. Cell Biol.*, 1:489–530, 1985.

[37] S. Nagotu, V. C. Kalel, R. Erdmann, and H. W. Platta. Molecular basis of peroxisomal biogenesis disorders caused by defects in peroxisomal matrix protein import. *Biochim. Biophys. Acta*, 1822:1326–1336, 2012.

[38] M. O. Freitas, T. Francisco, T. A. Rodrigues, I. S. Alencastre, M. P. Pinto, C. P. Grou, A. F. Carvalho, M. Fransen, C. Sa-Miranda, and J. E. Azevedo. PEX5 protein binds monomeric catalase blocking its tetramerization and releases it upon binding the N-terminal domain of PEX14. *J. Biol. Chem.*, 286:40509–40519, 2011.

[39] C. Williams, M. van den Berg, R. R. Sprenger, and B Distel. A conserved cysteine is essential for Pex4p-dependent ubiquitination of the peroxisomal import receptor Pex5p. *J. Biol. Chem.*, 282:22534–22543, 2007.

[40] I. S. Alencastre, T. A. Rodrigues, C. P. Grou, M. Fransen, C. Sá-Miranda, and J. E. Azevedo. Mapping the cargo protein membrane translocation step into the PEX5 cycling pathway. *J. Biol. Chem.*, 284:27243–27251, 2009.

[41] C. P. Grou, A. F. Carvalho, M. P. Pinto, S. Wiese, H. Piechura, H. E. Meyer, B. Warscheid, C. Sa-Miranda, and J. E. Azevedo. Members of the E2D (UbcH5) family mediate the ubiquitination of the conserved cysteine of Pex5p, the peroxisomal import receptor. *J. Biol. Chem.*, 283:14190–14197, 2008.

[42] A. M. Gouveia, C. P. Guimaraes, M. E. Oliveira, C. Sa-Miranda, and J. E. Azevedo. Insertion of Pex5p into the peroxisomal membrane is cargo protein-dependent. *J. Biol. Chem.*, 278:4389–4392, 2003.

[43] M. Meinecke, C. Cizmowski, W. Schliebs, V. Kruger, S. Beck, R. Wagner, and R. Erdmann. The peroxisomal importomer constitutes a large and highly dynamic pore. *Nat. Cell Biol.*, 12:273–277, 2010.

[44] Y. Fujiki, C. Nashiro, N. Miyata, S. Tamura, and K. Okumoto. New insights into dynamic and functional assembly of the AAA peroxins, Pex1p and Pex6p, and their membrane receptor Pex26p in shuttling of PTS1-receptor Pex5p during peroxisome biogenesis. *Biochim. Biophys. Acta*, 1823:145–149, 2012.

[45] M. O. Debelyy, H. W. Platta, D. Saffian, A. Hensel, S. Thoms, H. E. Meyer, B. Warscheid, W. Girzalsky, and R. Erdmann. Ubp15p, a ubiquitin hydrolase associated with the peroxisomal export machinery. *J. Biol. Chem.*, 286:28223–28234, 2011.

[46] C. M. Pickart. Mechanisms underlying ubiquitination. *Annu. Rev. Biochem.*, 70:503–533, 2001.

[47] C. Williams, M. van den Berg, E. Geers, and B. Distel. Pex10p functions as an E3 ligase for the ubc4p-dependent ubiquitination of Pex5p. *Biochem. Biophys. Res. Commun.*, 374:620–624, 2008.

[48] C. Williams, M. van den Berg, S. Panjikar, W. A. Stanley, B. Distel, and M. Wilmanns. Insights into ubiquitin-conjugating enzyme/co-activator interactions from the structure of the Pex4p:Pex22p complex. *EMBO J.*, 31:391–402, 2012.

[49] A. F. Carvalho, M. P. Pinto, C. P. Grou, I. S. Alencastre, M. Fransen, C. Sa-Miranda, and J. E. Azevedo. Ubiquitination of mammalian Pex5p, the peroxisomal import receptor. *J. Biol. Chem.*, 282:31267–31272, 2007.

[50] B. K. Zolman, M. Monroe-Augustus, I. D. Silva, and B. Bartel. Identification and functional characterization of *Arabidopsis* PEROXIN4 and the interaction protein PEROXIN22. *Plant Cell*, 17:3422–3435, 2005.

[51] H. W. Platta, F. El Magraoui, B. E. Baumer, D. Schlee, W. Girzalsky, and R. Erdmann. Pex2 and Pex12 function as protein-ubiquitin ligases in peroxisomal protein import. *Mol. Cell Biol.*, 29:5505–5516, 2009.

[52] K. Okumoto, S. Misono, N. Miyata, Y. Matsumoto, S. Mukai, and Y. Fujiki. Cysteine ubiquitination of PTS1 receptor Pex5p regulates Pex5p recycling. *Traffic*, 12:1067–1083, 2011.

[53] I. Birschmann, A. K. Stroobants, M. van den Berg, A. Schafer, K. Rosenkranz, W. Kunau, and H. F. Tabak. Pex15p of *Saccharomyces cerevisiae* provides a molecular basis for recruitment of the AAA peroxin Pex6p to peroxisomal membranes. *Mol. Biol. Cell*, 14:2226–2236, 2003.

[54] K. Rosenkranz, I. Birschmann, S. Grunau, W. Girzalsky, W. Kunau, and R. Erdmann. Functional association of the AAA complex and the peroxisomal importomer. *FEBS J.*, 273:3804–3815, 2006.

[55] C. P. Grou, T. Francisco, T. A. Rodrigues, M. O. Freitas, M. P. Pinto, A. F. Carvalho, P. Domingues, S. A. Wood, J. E. Rodriguez-Borges, C. Sa-Miranda, M. Fransen, and J. E. Azevedo. Identification of ubiquitin-specific protease 9X (Usp9X) as a deubiquitinase acting on ubiquitin-peroxin 5 (PEX5) thioester conjugate. *J. Biol. Chem.*, 287:12815–12827, 2012.

[56] A. M. M. Gouveia, C. Reguenga, M. E. M Oliveira, C. Sa-Miranda, and J. E. Azevedo. Characterization of peroxisomal Pex5p from rat liver. *J. Biol. Chem.*, 275:32444–32451, 2000.

[57] P. A. Walton, P. E. Hill, and S. Subramani. Import of stably folded proteins into peroxisomes. *Mol. Biol. Cell*, 6:675–683, 1995.

[58] C. Ma, G. Agrawal, and S. Subramani. Peroxisome assembly: matrix and membrane protein biogenesis. *J. Cell Biol.*, 193:7–16, 2011.

[59] V. D. Antonenkov and J. K. Hiltunen. Peroxisomal membrane permeability and solute transfer. *Biochim. Biophys. Acta*, 1763:1697–1706, 2006.

[60] D. Wang, N. V. Visser, M. Veenhuis, and I. J. van der Klei. Physical interactions of the peroxisomal targeting signal 1 receptor Pex5p, studied by fluorescence correlation spectroscopy. *J. Biol. Chem.*, 278:43340–43345, 2003.

[61] C. P. Grou, A. F. Carvalho, M. P. Pinto, I. S. Alencastre, T. A. Rodrigues, M. O. Freitas, T. Francisco, C. Sá-Miranda, and J. E. Azevedo. The peroxisomal protein import machinery — a case report of transient ubiquitination with a new flavor. *Cell Mol. Life Sci.*, 66:254–262, 2009.

[62] W. Schliebs, W. Girzalsky, and R. Erdmann. Peroxisomal protein import and ERAD: variations on a common theme. *Nat. Rev. Mol. Cell. Biol.*, 11:885–890, 2010.

[63] H. W. Platta, S. Hagen, and R. Erdmann. The exportomer: the peroxisomal receptor export machinery. *Cell Mol. Life Sci.*, 70:1393–1411, 2013.

[64] J. M. Nuttall, A. Motley, and E. H. Hettema. Peroxisome biogenesis: recent advances. *Curr. Opin. Cell Biol.*, 23:421–426, 2011.

[65] A. Aranovich, R. Hua, A. D. Rutenberg, and P. K. Kim. PEX16 contributes to peroxisome maintenance by constantly trafficking PEX3 via the ER. *J. Cell Sci.*, 127:3675–3686, 2014.

[66] A. van der Zand, I. Braakman, and H. F. Tabak. Peroxisomal membrane proteins insert into the endoplasmic reticulum. *Mol. Biol. Cell*, 21:2057–2065, 2010.

[67] S. Thoms, I. Harms, K-U. Kalies, and J. Gartner. Peroxisome formation requires the endoplasmic reticulum channel protein Sec61. *Traffic*, 13:599–609, 2012.

[68] A. van der Zand, J. Gent, I. Braakman, and H. F. Tabak. Biochemically distinct vesicles from the endoplasmic reticulum fuse to form peroxisomes. *Cell*, 149:397–409, 2012.

[69] V. I. Titorenko, H. Chan, and R. A. Rachubinski. Fusion of small peroxisomal vesicles in vitro reconstructs an early step in the in vivo multistep peroxisome assembly pathway of *Yarrowia lipolytica*. *J. Cell Biol.*, 2000:29–43, 2000.

[70] M. Schrader and H. D. Fahimi. Growth and division of peroxisomes. *Int. Rev. Cytol.*, 255:237–290, 2006.

[71] D. Hoepfner, D. Schildknegt, I. Braakman, P. Philippsen, and H. F. Tabak. Contribution of the endoplasmic reticulum to peroxisome formation. *Cell*, 122:85–95, 2005.

[72] S. Nagotu, M. Veenhuis, and I. J. van der Klei. Divide et impera: the dictum of peroxisomes. *Traffic*, 11:175–184, 2010.

[73] M. Schrader, N. A. Bonekamp, and M. Islinger. Fission and proliferation of peroxisomes. *Biochim. Biophys. Acta*, 1822:1343–1357, 2012.

[74] M. Schrader, B. E. Reubers, J. C. Morrell, G. Jimenez-Sanchez, C. Obie, T. A. Stroh, D. Valle, T. A. Schroer, and S. J. Gould. Expression of $PEX11\beta$ mediates peroxisome proliferation in the absence of extracellular stimuli. *J. Biol. Chem.*, 273:29607–29614, 1998.

[75] H. K. Delille, B. Agricola, S. C. Guimaraes, H. Borta, G. H. Luers, M. Fransen, and M. Schrader. Pex11pβ-mediated growth and division of mammalian peroxisomes follows a maturation pathway. *J. Cell Sci.*, 123:2750–2762, 2010.

[76] M. N. Cepinska, M. Veenhuis, I. J. van der Klei, and S. Nagotu. Peroxisome fission is associated with reorganization of specific membrane proteins. *Traffic*, 12:925–937, 2011.

[77] W-H. Kunau. Peroxisome biogenesis: end of the debate. *Curr. Biol.*, 15:R774–R776, 2005.

[78] G. Agrawal, S. Joshi, and S. Subramani. Cell-free sorting of peroxisomal membrane proteins from the endoplasmic reticulum. *Proc. Natl. Acad. Sci. USA*, 108:9113–9118, 2011.

[79] S. K. Lam, N. Yoda, and R. Schekman. A vesicle carrier that mediates peroxisome protein traffic from the endoplasmic reticulum. *Proc. Natl. Acad. Sci. USA*, 108:E51–E52, 2011.

[80] M. Nordgren, B. Wang, O. Apanasets, and M. Fransen. Peroxisome degradation in mammals: mechanisms of action, recent advances, and perspectives. *Front. Physiol.*, 4:145, 2013.

[81] H. W. Platta and R. Erdmann. Peroxisomal dynamics. *Trends Cell Biol.*, 17:474–484, 2007.

[82] M. Veenhuis, A. Douma, W. Harder, and M. Osumi. Degradation and turnover of peroxisomes in the yeast *Hansenula polymorpha* induced by selective inactivation of peroxisomal enzymes. *Arch. Microbiol.*, 134:193–203, 1983.

[83] A. Till, R. Lakhani, S. F. Burnett, and S. Subramani. Pexophagy: the selective degradation of peroxisomes. *Intl. J. Cell Biol.*, 2012:Article ID 512721, 2012.

[84] J. Iwata, J. Ezaki, M. Komatsu, S. Yokota, T. Ueno, I. Tanida, T. Chiba, K. Tanaka, and E. Kominami. Excess peroxisomes are degraded by autophagic machinery in mammals. *J. Biol. Chem.*, 281:4035–4041, 2006.

[85] T. Y. Nazarko, J-C. Farre, and S. Subramani. Peroxisome size provides insights into the function of autophagy-related proteins. *Mol. Biol. Cell*, 20:3828–3839, 2009.

[86] I. Monastryska, K. Sjollema, I. J. van der Klei, J. A. K. W. Kiel, and M. Veenhis. Microautophagy and macropexophagy may occur simultaneously in *Hansenula polymorpha*. *FEBS Lett.*, 568:135–138, 2004.

[87] Y. Sakai, A. Koller, L. K. Rangell, G. A. Keller, and S. Subramani. Peroxisome degradation by microautophagy in *Pichia pastoris*: identification of specific steps and morphological intermediates. *J. Cell Biol.*, 141:625–636, 1998.

[88] K. Okamoto. Organellophagy: eliminating cellular building blocks via selective autophagy. *J. Cell Biol.*, 205:435–445, 2014.

[89] A. Stolz, A. Ernst, and I. Dikic. Cargo recognition and trafficking in selective autophagy. *Nat. Cell. Biol.*, 16:495–501, 2014.

[90] D. C. Rubinsztein, G. Marino, and G. Kroemer. Autophagy and aging. *Cell*, 146:682–695, 2011.

[91] C. Puri, M. Renna, C. F. Bento, K. Moreau, and D. C. Rubinsztein. Diverse autophagosome membrane sources coalesce in recycling endosomes. *Cell*, 154:1285–1299, 2013.

[92] B. Ravikumar, S. Sarkar, J. E. Davies, M. Futter, M. Garcia-Arencibia, Z. W. Green-Thompson, M. Jimenez-Sanchez, V. I. Korolchuk, M. Lichtenberg, S. Luo, D. C. O. Massey, F. M. Menzies, K. Moreau, U. Narayanan, M. Renna, F. H. Siddiqui, B. R. Underwood, A. R. Winslow, and D. C. Rubinsztein. Regulation of mammalian autophagy in physiology and pathophysiology. *Physio. Rev.*, 90:1383–1435, 2010.

[93] T. Johansen and T. Lamark. Selective autophagy mediated by autophagic adapter proteins. *Autophagy*, 7:279–296, 2011.

[94] T. Y. Nazarko, K. Ozeki, A. Till, G. Ramakrishnan, P. Lotfi, M. Yan, and S. Subramani. Peroxisomal Atg37 binds Atg30 palmitoyl-CoA to regulate phagophore formation during pexophagy. *J. Cell Biol.*, 204:541–557, 2014.

[95] T-C Kuo, C-T Chen, D. Baron, T. T. Onder, S. Loewer, S. Almeida, C. M. Weismann, P. Xu, J-M. Houghton, F-B. Gao, G. Q. Daley, and S. Doxsey. Midbody accumulation through evasion of autophagy contributes to cellular reprogramming and tumorigenicity. *Nat. Cell Biol.*, 13:1214–1223, 2011.

[96] K. O. Schink and H. Stenmark. Cell differentiation: midbody remnants - junk or fate factors? *Curr. Biol.*, 21:R958–R960, 2011.

[97] V. Kirkin, D. G. McEwan, I. Novak, and I. Dikic. A role for ubiquitin in selective autophagy. *Mol. Cell*, 34:259–269, 2009.

[98] G. Bjorkoy, T. Lamark, A. Brech, H. Outzen, M. Perander, A. Overvatn, H. Stenmark, and T. Johansen. p62/SQSTM1 forms protein aggregates degraded by autophagy and has a protective effect on huntingtin-induced cell death. *J. Cell Biol.*, 171:603–614, 2005.

[99] S. Pankiv, T. H. Clausen, T. Lamark, A. Brech, J-A. Bruun, H. Outzen, A. Overvatn, G. Bjorkoy, and T. Johansen. p62/SQSTM1 binds directly to Atg8/LC3 to facilitate degradation of ubiquitinated protein aggregates by autophagy. *J. Biol. Chem.*, 282:24131–24145, 2007.

[100] X. Lin, S. Li, Y. Zhao, X. Ma, K. Zhang, X. He, and Z. Wang. Interaction domains of p62: a bridge between p62 and selective autophagy. *DNA Cell Biol.*, 32:220–227, 2013.

[101] A. B. Birgisdottir, T. Lamark, and T. Johansen. The LIR motif - crucial for selective autophagy. *J. Cell Sci.*, 126:3237–3247, 2013.

[102] R. K. Vadlamudi, I. Joung, J. L. Strominger, and J. Shin. p62, a phosphotyrosine-independent ligand of the SH2 domain of p56, belongs to a new class of ubiquitin-binding proteins. *J. Biol. Chem.*, 271:20235–20237, 1996.

[103] T. Lamark, M. Perander, H. Outzen, K. Kristiansen, A. Overvatn, E. Michaelsen, G. Bjorkoy, and T. Johansen. Interaction codes within the family of mammalian Phox and Bem1p domain-containing proteins. *J. Biol. Chem.*, 278:34568–34581, 2003.

[104] V. Kirkin, T. Lamark, Y-S. Sou, G. Bjorkoy, J. L. Nunn, J-A. Bruun, E. Shvets, D. G. McEwan, T. H. Clausen, P. Wild, I. Bilusic, J-P. Theurillat, A. Overvatn, T. Ishii, Z. Elazar, M. Komatsu, I. Dikic, and T. Johansen. A role for NBR1 in autophagosomal degradation of ubiquitinated substrates. *Mol. Cell*, 33:505–516, 2009.

[105] S. Mostowy, V. Sancho-Shimizu, M. A. Hamon, R. Simeone, R. Brosch, T. Johansen, and P. Cossart. p62 and NDP52 proteins target intracytosolic *Shigella* and *Listeria* to different autophagy pathways. *J. Biol. Chem.*, 286:26987–26995, 2011.

[106] A. Ciechanover. The ubiquitin-proteasome proteolytic pathway. *Cell*, 79:13–21, 1994.

[107] E. Walinda, D. Morimoto, K. Sugase, T. Konuma, H. Tochio, and M. Shirakawa. Solution structure of the ubiquitin-associated (UBA) domain of human autophagy receptor NBR1 and its interaction with ubiquitin and polyubiquitin. *J. Biol. Chem.*, 289:13890–13902, 2014.

[108] A. J. Bray. Theory of phase-ordering kinetics. *Adv. Phys.*, 51:481–587, 2002.

[109] K. Binder. Theory of first-order phase transitions. *Rep. Prog. Phys.*, 50:783–859, 1987.

[110] J. H. Yao, K. R. Elder, H. Guo, and M. Grant. Theory and simulation of Ostwald ripening. *Phys. Rev. B*, 47:110–125, 1993.

[111] I. M. Lifshitz and V. V. Slyozov. The kinetics of precipitation from supersaturated solid solutions. *J. Phys. Chem. Solids*, 19:35–50, 1961.

[112] C. Wagner. Theory of the aging of precipitates by dissolution-reprecipitation (ostwald ripening). *Z. Electrochem.*, 65:581–591, 1961.

[113] P. W. Voorhees. The theory of ostwald ripening. *J. Stat. Phys.*, 38:231–252, 1985.

[114] B. Krishnamachari, J. McLean, B. Cooper, and J. Sethna. Gibbs-thomson formula for small island sizes: corrections ofr high vapor densities. *Phys. Rev. B*, 54:8899–8907, 1996.

[115] T. M. Rogers and R. C. Desai. Numerical study of late-stage coarsening for off-critical quenches in the Cahn-Hilliard equation of phase separation. *Phys. Rev. B*, 39:956–964, 1989.

[116] O. G. Berg and P. H. von Hippel. Diffusion-controlled macromolecular interactions. *Ann. Rev. Biophys. Biophys. Chem.*, 14:131–160, 1985.

[117] H. C. Berg and E. M. Purcell. Physics of chemoreception. *Biophys. J.*, 20:193–219, 1977.

[118] O. G. Berg, R. B. Winter, and P. H. von Hippel. Diffusion-driven mechanisms of protein translocation on nucleic acids. 1. models and theory. *Biochemistry*, 20:6929–6948, 1981.

[119] S. E. Halford and J. F. Marko. How do site-specific DNA-binding proteins find their targets. *Nucleic Acids Res.*, 32:3040–3052, 2004.

[120] N. P. Stanford, M. D. Szczelkun, J. F. Marko, and S. E. Halford. One- and three-dimensional pathways for proteins to reach specific DNA sites. *EMBO J.*, 19:6546–6557, 2000.

[121] D. T. Gillespie. Exact stochastic simulation of coupled chemical reactions. *J. Phys. Chem.*, 81:2340–2361, 1977.

[122] D. J. Barnes and D. Chu. *Introduction to modeling for biosciences*. Springer, London, 2010.

[123] S. Mukherji and E. K. O'Shea. Mechanisms of organelle biogenesis govern stochastic fluctuations in organelle abundance. *eLife*, 3:e02678, 2014.

[124] C. S. Borlin, V. Lang, A. Hamacher-Brady, and N. R. Brady. Agent-based modeling of autophagy reveals emergent regulatory behavior of spatio-temporal autophagy dynamics. *Cell Commun. Signal.*, 812:56, 2014.

[125] C. R. Nayak, A. I. Brown, and A. D. Rutenberg. Protein translocation without specific quality control in a computational model of the Tat system. *Phys. Biol.*, 11:056005, 2014.

[126] A. Zilman, S. Di Talia, T. Jovanovic-Talisman, B. T. Chait, M. P. Rout, and M. O. Magnasco. Enhancement of transport selectivity through nano-channels by non-specific competition. *PLoS Comput. Biol.*, 6:e1000804, 2010.

[127] G. L. Ryan and A. D. Rutenberg. Clocking out: modeling phase-induced lysis of *Escherichia coli*. *J. Bacteriol.*, 189:4749–4755, 2007.

[128] J. Derr and A. D. Rutenberg. Monodisperse domains by protelytic control of the coarsening instability. *Phys. Rev. E*, 84:011928, 2011.

[129] A. S. Howell, M. Jin, C-F. Wu, T. R. Zyla, T. C. Elston, and D. J. Lew. Robustness in the yeast polarity establishment circuit. *Cell*, 149:322–333, 2012.

[130] M. S. Turner, P. Sens, and N. D. Socci. Nonequilibrium raftlike membrane domains under continuous recycling. *Phys. Rev. Lett.*, 95:168301, 2005.

[131] M. Schrader and H. D. Fahimi. The peroxisome: still a mysterious organelle. *Histochem. Cell Biol.*, 129:421–440, 2008.

[132] R. J. A. Wanders and H. R. Waterham. Biochemistry of mammalian peroxisomes revisited. *Annu. Rev. Biochem.*, 75:295–332, 2006.

[133] R. Hess, W. Staubli, and R. Riess. Nature of the hepatomegalic effect produced by ethy-chlorophenoxy-isobutyrate in the rate. *Nature*, 208:856–858, 1965.

[134] D. E. Moody and J. K. Reddy. Morphometric analysis of the ultrastructural changes in rat liver induced by the peroxisome proliferator SaH. *J. Cell Biol.*, 71:768–780, 1976.

[135] S. Yokota. Degradation of normal and proliferated peroxisomes in rat hepatocytes: regulation of peroxisomes quantity in cells. *Micosc. Res. Tech.*, 61:151–160, 2003.

[136] X. Liu, C. Ma, and S. Subramani. Recent advances in peroxisomal matrix protein import. *Curr. Opin. Cell Biol.*, 24:484–489, 2012.

[137] R. Natsuyama, K. Okumoto, and Y. Fujiki. Pex5p stabilizes Pex14p: a study using a newly isolated *pex5* CHO cell mutant, ZPEG101. *Biochem. J.*, 449:195–207, 2013.

[138] K. Shiozawa, P. V. Konarev, C. Neufeld, M. Wilmanns, and D. I. Svergun. Solution structure of human Pex5·Pex14·PTS1 protein complexes obtained by small angle X-ray scattering. *J. Biol. Chem.*, 284:25334–25342, 2009.

[139] A. Schell-Steven, K. Stein, M. Amoros, C. Landgraf, R. Volkmer-Engert, H. Rottensteiner, and R. Erdmann. Identification of a novel, intraperoxisomal Pex14-binding site in Pex13: Association of Pex13 with the docking complex is essential for peroxisomal matrix protein import. *Mol. Cell Biol.*, 25:3007–3018, 2005.

[140] H. W. Platta, W. Girzalsky, and R. Erdmann. Ubiquitination of the peroxisomal import receptor Pex5p. *Biochem. J.*, 384:37–45, 2004.

[141] J. A. K. W. Kiel, K. Emmrich, H. Meyer, and W. Kunau. Ubiquitination of the the peroxisomal targeting signal type 1 receptor, Pex5p, suggests the presence of a quality control mechanism during peroxisomal matrix protein import. *J. Biol. Chem.*, 280:1921–1930, 2005.

[142] R. Erdmann and W. Schliebs. Peroxisomal matrix protein import: the transient pore model. *Nat. Rev. Mol. Cell Biol.*, 6:738–742, 2005.

[143] H. W. Platta, F. el Magraoui, D. Schlee, S. Grunau, W. Girzalsky, and R. Erdmann. Ubiquitination of the peroxisomal import receptor Pex5p is required for its recycling. *J. Cell Biol.*, 177:197–204, 2007.

[144] M. E. Oliveira, A. M. Gouveia, R. A. Pinto, C. Sa-Miranda, and J. E. Azevedo. The energetics of Pex5p-mediated peroxisomal protein import. *J. Biol. Chem.*, 278:39483–39488, 2003.

[145] N. Miyata and Y. Fujiki. Shuttling mechanism of peroxisome targeting signal type 1 receptor Pex5: ATP-independent import and ATP-dependent export. *Mol. Cell Biol.*, 25:10822–10832, 2005.

[146] J. E. Azevedo and W. Schliebs. Pex14p, more than just a docking protein. *Biochim. Biophys. Acta*, 1763:1574–1584, 2006.

[147] N. Miyata, K. Hosoi, S. Mukai, and Y. Fujiki. In vitro import of peroxisome-targeting signal type 2 (PTS2) receptor Pex7p into peroxisomes. *Biochim. Biophys. Acta*, 1793:860–870, 2009.

[148] A. Hensel, S. Beck, F. el Magraoui, H. W. Platta, W. Girzalsky, and R. Erdmann. Cysteine-dependent ubiquitination of Pex18p is linked to cargo translocation across the peroxisomal membrane. *J. Biol. Chem.*, 286:43495–43505, 2011.

[149] T. Kuhn, T. O. Ihalainen, J. Hyvaluoma N. Dross, S. F. Willman, Langowski, M. Vihinen-Ranta, and J. Timonen. Protein diffusion in mammalian cell cytoplasm. *PLoS ONE*, 6:e22962, 2011.

[150] W. Schliebs, J. Saidowsky, B. Agianian, G. Dodt, F. W. Herberg, and W. Kunau. Recombinant human peroxisomal targeting signal receptor PEX5. *J. Biol. Chem.*, 274:5666–5673, 1999.

[151] M. Scheffner, J. M. Huibregtse, and P. M. Howley. Identification of a human ubiquitin-conjugating enzyme that mediates the E6-AP-dependent ubiquitination of p53. *Proc. Natl. Acad. Sci. USA*, 91:8797–8801, 1994.

[152] J. P. Jensen, P. W. Bates, M. Yang, R. D. Vierstra, and A. M. Weissman. Identification of a family of closely related human ubiquitin conjugating enzymes. *J. Biol. Chem.*, 270:30408–30414, 1995.

[153] M. K. Summers, B. Pan, K. Mukhyala, and P. K. Jackson. The unique N terminus of the UbcH10 E2 enzyme controls the threshold for the APC activation and enhances checkpoint regulation of the APC. *Mol. Cell*, 31:544–556, 2008.

[154] P. S. Pyenta, P. Schwille, W. W. Webb, D. Holowka, and B. Baird. Lateral diffusion of membrane lipid-anchored probes before and after aggregation of cell surface IgE-receptors. *J. Phys. Chem. A*, 107:8310–8318, 2003.

[155] J. Valdez-Taubas and H. R. B. Pelham. Slow diffusion of proteins in the yeast plasma membrane allows polarity to be maintained by endocytic cycling. *Curr. Biol.*, 13:1636–1640, 2003.

[156] E. Marco, R. Wedlich-Soldner, R. Li, S. J. Altschuler, and L. F. Wu. Endocytosis optimizes the dynamic localization of membrane proteins that regulate cortical polarity. *Cell*, 129:411–422, 2007.

[157] H. P. Erickson. Size and shape of protein molecules at the nanometer level determined by sedimentation, gel filtration, and electron microscopy. *Biol. Proced. Online*, 11:32–51, 2009.

[158] G. Dodt, N. Braverman, C. Wong, A. Moser, H. W. Moser, P. Watkins, D. Valle, and S. J. Gould. Mutations in the PTS1 receptor gene, PXR1, define complementation group 2 of the peroxisome biogenesis disorders. *Nat. Genet.*, 9:115–125, 1995.

[159] G. Dodt and S. J. Gould. Multiple PEX genes are required for proper subcellular distribution and stability of Pex5p, the PTS1 receptor: evidence that PTS1 protein import is mediated by a cycling receptor. *J. Cell Biol.*, 135:1763–1774, 1996.

[160] M. Lazarou, S. M. Jin, L. A. Kane, and R. J. Youle. Role of PINK1 binding to the TOM complex and alternate intracellular membranes in recruitment and activation of the E3 ligase Parkin. *Dev. Cell*, 22:320–333, 2012.

[161] S. Hara-Kuge and Y. Fujiki. The peroxin Pex14p is involved in LC3-dependent degradation of mammalian peroxisomes. *Exp. Cell Res.*, 314:3531–3541, 2008.

[162] N. Macdonald, S. Chevalier, R. Tonge, M. Davison, R. Rowlinson, J. Young, S. Rayner, and R. Roberts. Quantitative proteomic analysis of mouse liver response to the peroxisome proliferator diethylhexylphthalate (DEHP). *Arch. Toxicol.*, 75:415–424, 2001.

[163] M. Rakhshandehroo, B. Knoch, M. Müller, and S. Kersten. Peroxisome proliferator-activated receptor alpha target genes. *PPAR Res.*, 2010:612089, 2010.

[164] N. Matsumoto, S. Tamura, and Y. Fujiki. The pathogenic peroxin Pex26p recruits the Pex1p-Pex6p AAA ATPase complexes to peroxisomes. *Nat. Cell Biol.*, 5:454–460, 2003.

[165] M. B. Rosen, J. R. Schmid, J. C. Corton, R. D. Zehr, K. P. Das, B. D. Abbott, and C. Lau. Gene expression profiling in wild-type and and PPARα-null mice exposed to perfluorooctane sulfonate reveals PPARα-independent effects. *PPAR Res.*, 2010:794739, 2010.

[166] H. W. Platta, M. O. Debelyy, F. El Magraoui, and R. Erdmann. The AAA peroxins Pex1p and Pex6p function as dislocases for the ubiquitinated peroxisomal import receptor Pex5p. *Biochem. Soc. Trans.*, 36:99–104, 2008.

[167] N. Miyata, K. Okumoto, S. Mukai, M. Noguchi, and Y. Fujiki. AWP1/ZFAND6 functions in Pex5 export by interacting with cys-monoubiquitinated Pex5 and Pex6 AAA ATPase. *Traffic*, 13:168–183, 2012.

[168] A. M. Motley, J. M. Nuttall, and E. H. Hettema. Pex3-anchored Atg36 tags peroxisomes for degradation in *Saccharomyces cerevisiae*. *EMBO J.*, 31:2852–2868, 2012.

[169] C. Williams and I. J. van der Klei. Pexophagy-linked degradation of the peroxisomal membrane protein Pex3p involves the ubiquitin-proteasome system. *Biochem. Biophys. Res. Commun.*, 438:395–401, 2013.

[170] M. Semplice, A. Veglio, G. Naldi, G. Serini, and A. Gamba. A bistable model of cell polarity. *PLOS One*, 7:e30977, 2012.

[171] M. Veenhuis, K. Zwart, and W. Harder. Degradation of peroxisomes after transfer of methanol-grown *Hansenula polymorpha* into glucose-containing media. *FEMS Microbiol. Lett.*, 3:21–28, 1978.

[172] R. White, S. Chiba, T. Pang, J. S. Dewey, C. G. Savva, A. Holzenburg, K. Pogliano, and R. Young. Holin triggering in real time. *Proc. Natl. Acad. Sci. USA*, 108:798–803, 2011.

[173] I. A. Stegun. *Handbook of mathematical functions*, chapter Legendre functions. Number 8. National Bureau of Standards, 1970.

[174] A. Erdelyi, W. Magnus, F. Oberhettinger, and F. G. Tricomi. *Higher Transcendental Functions*, volume 1. McGraw-Hill, 1953.

[175] D. O. Yi, M. H. Jhon, I. D. Sharp, Q. Xu, C. W. Yuan, C. Y. Liao, J. W. Ager III, E. E. Haller, and D. C. Chrzan. Modeling nucleation and growth of encapsulated nanocrystals: kinetic monte carlo simulations and rate theory. *Phys. Rev. B*, 78:245415, 2008.

[176] M. Strobel, K-H. Heinig, and W. Moller. Three-dimensional domain growth on the size scale of the capillary length: effective growth exponent and comparative atomistic and mean-field simulations. *Phys. Rev. B.*, 64:245422, 2001.

[177] A. I. Brown, P. K. Kim, and A. D. Rutenberg. PEX5 and ubiquitin dynamics on mammalian peroxisome membranes. *PLOS Comput. Biol.*, 10:e1003426, 2014.

[178] B. P. Vollmayr-Lee and A. D. Rutenberg. Fast and accurate coarsening simulation with an unconditionally stable time step. *Phys. Rev. E*, 68:066703, 2003.

[179] I. Ispolatov and A. Musch. A model for the self-organization of the vesicular flux and protein distributions in the Golgi apparatus. *PLOS Comput. Biol.*, 9:e1003125, 2013.

[180] C. C. Hayden, J. S. Hwang, E. A. Abate, M. S. Kent, and D. Y. Sasaki. Directed formation of lipid membrane microdomains as high affinity sites for his-tagged proteins. *J. Am. Chem. Soc.*, 131:8728–8729, 2009.

[181] A. D. Rutenberg and B. P. Vollmayr-Lee. Anisotropic coarsening: grain shapes and nonuniversal persistence. *Phys. Rev. Lett.*, 83:3772–3775, 1999.

[182] F. Liu, Y. Lu, L. Pieuchot, T. Dhavale, and G. Jedd. Import oligomers induce positive feedback to promote peroxisome differentiation and control organelle abundance. *Dev. Cell*, 21:457–468, 2011.

[183] F. J. Vizeacoumar, J. C. Torres-Guzman, D. Bouard, J. D. Aitchison, and R. A. Rachubinski. Pex30p, Pex31p, and Pex32p form a family of peroxisomal integral membrane proteins regulating peroxisome size and number in *Saccharomyces cerevisiae*. *Mol. Biol. Cell*, 15:665–677, 2004.

[184] L. Golubovic and M. Golubovic. Nonequilibrium size distributions of fluid membrane vesicles. *Phys. Rev. E*, 56:3219–3230, 1997.

[185] J. J. Sieber, K. I. Willig, R. Heintzmann, S. W. Hell, and T. Lang. The SNARE motif is essential for the formation of syntaxin clusters in the plasma membrane. *Biophys. J.*, 90:2843–2951, 2006.

[186] A. I. Brown and A. D. Rutenberg. Cluster coarsening on drops exhibits strong and sudden size-selectivity. *Soft Matter*, 11:3786–3793, 2015.

[187] M. Shibata, K. Oikawa, K. Yoshimoto, M. Kondo, S. Mano, K. Yamada, M. Hayashi, W. Sakamoto, Y. Ohsumi, and M. Nishimura. Highly oxidized peroxisomes are selectively degraded via autophagy in *Arabidopsis*. *The Plant Cell*, 25:4967–4983, 2013.

[188] T. van Zutphen, M. Veenhuis, and I. J. van der Klei. Damaged peroxisomes are subject to rapid autophagic degradation in the yeast *Hansenul polymorpha*. *Autophagy*, 7:863–872, 2011.

[189] W. J. Brittain and S. Minko. A structural definition of polymer brushes. *J. Polym. Sci. A*, 45:3505–3512, 2007.

[190] K. Hristova and D. Needham. The influence of polymer-grafted lipids on the physical properties of lipid bilayers: a theoretical study. *J. Colloid Inter. Sci.*, 168:302–314, 1994.

[191] J. C. Stachowiak, E. M. Schmid, C. J. Ryan, H. S. Ann, D. Y. Sasaki, M. B. Sherman, P. L. Geissler, D. A. Fletcher, and C. C. Hayden. Membrane bending by protein-protein crowding. *Nat. Cell Biol.*, 14:944–949, 2012.

[192] J. C. Stachowiak, C. C. Hayden, and D. Y. Sasaki. Steric confinement of proteins on lipid membranes can drive curvature and tubulation. *Proc. Natl. Acad. Sci. USA*, 107:7781–7786, 2010.

[193] C. S. Scheve, P. A. Gonzales, N. Momin, and J. C. Stachowiak. Steric pressure between membrane-bound proteins opposes lipid phase separation. *J. Am. Chem. Soc.*, 135:1185–1188, 2013.

[194] J. J. Sieber, K. I. Willig, C. Kutzner, C. Gerding-Reimers, B. Harke, G. Donnert, B. Rammner, C. Eggeling, S. W. Hell, H. Grubmuller, and T. Lang. Anatomy and dynamics of a supramolecular membrane protein cluster. *Science*, 317:1072–1076, 2007.

[195] T. A. Ryan, J. Myer, D. Holowka, B. Baird, and W. W. Webb. Molecular crowing on the cell surface. *Science*, 239:61–64, 1988.

[196] R. B. Cornell and S. G. Taneva. Amphipathic helices as mediators of the membrane interaction of amphitropic proteins, and as modulators of bilayer physical properties. *Curr. Protein Pept. Sci.*, 7:539–552, 2006.

[197] M. I. Wilson, D. J. Gill, O. Perisic, M. T. Quinn, and R. L. Williams. PB1 domain-mediated heterodimerization in NADPH oxidase and signaling complexes of atypical protein kinase C with Par6 and p62. *Mol. Cell*, 12:39–50, 2003.

[198] M. Komatsu, S. Kageyama, and Y. Ichimura. p62/SQSTM1/A170: physiology and pathology. *Pharmacol. Res.*, 66:457–462, 2012.

[199] C. A. Whitehouse, S. Waters, K. Marchbank, A. Horner, N. W. A. McGowan, J. V. Jovanovic, G. M. Xavier, T. G. Kashima, M. T. Cobourne, G. O. Richards, P. T. Sharpe, T. M. Skerry, A. E. Grigoriadis, and E. Solomon. Neighbor of Brca1 gene (Nbr1) functions as a negative regulator of postnatal osteoblastic bone formation and p36 MAPK acvitity. *Proc. Natl. Acad. Sci. USA*, 107:12913–12918, 2010.

[200] A-S. Nicot, F. L. Verso, F. Ratti, F. Pilot-Storck, N. Streichenberger, M. Sandri, L. Schaeffer, and E. Goillot. Phosphorylation of NBR1 by GSK3 modulates protein aggregation. *Autophagy*, 10:1036–1053, 2014.

[201] S. Waters, K. Marchbank, E. Solomon, C. Whitehouse, and M. Gautel. Interactions with LC3 and polyubiquitin chains link nbr1 to autophagic protein turnover. *FEBS Lett.*, 583:1846–1852, 2009.

[202] J. Peng, D. Schwartz, J. E. Elias, C. C. Thoreen, D. Cheng, G. Marsischky, J. Roelofs, D. Finley, and S. P. Gygi. A proteomics approach to understanding protein ubiquitination. *Nat. Biotechnol.*, 21:921–926, 2003.

[203] S. van Delft, R. Govers, G. J. Strous, A. J. Verkleij, P. M. P. van Bergen, and B. en Henegouwen. Epidermal growth factor induces ubiquitination of Eps15. *J. Biol. Chem.*, 272:14013–14016, 1997.

[204] T. Geetha and M. W. Wooten. Structure and functional properties of the ubiquitin binding protein p62. *FEBS Lett.*, 512:19–25, 2002.

[205] J. Long, T. R. A. Gallagher, J. R. Cavey, P. W. Sheppard, S. H. Ralston, R. Layfield, and M. S. Searle. Ubiquitin recognition by the ubiquitin-associated domain of p62 involves a novel conformational switch. *J. Biol. Chem.*, 283:5427–5440, 2008.

[206] J. J. F. P. Luiken, M. van den Berg, J. C. Heikoop, and A. J. Meijer. Autophagic degradation of peroxisomes in isolated rat hepatocytes. *FEBS Lett.*, 304:93–97, 1992.

[207] U. Alon. *An introduction to systems biology.* Taylor and Francis, Boca Raton, 2007.

[208] S. Park, I. Jang, C. Zuber, Y. Lee, J. W. Cho, I. Matsuo, and Y. Ito. ERADication of EDEM1 occurs by selective autophagy and requires deglycosylation by cytoplasmic peptide N-glycanase. *Histochem. Cell Biol.*, 142:153–169, 2014.

[209] S. Shaid, C. H. Brandts, H. Serve, and I. Dikic. Ubiquitination and selective autophagy. *Cell Death Differ.*, 20:21–30, 2013.

[210] C. Odendall, E. Dixit, F. Stavru, H. Bierne, K. M. Franz, A. F. Durbin, S. Boulant, L. Gehrke, P. Cossart, and J. C. Kagan. Diverse intracellular pathogens activate type III interferon expression from peroxisomes. *Nat. Immunol.*, 15:717–726, 2014.

[211] F. Hou, L. Sun, H. Zheng, B. Skaug, Q-X. Jiang, and Z. J. Chen. MAVS forms functional prion-like aggregates to activate and propagate antiviral innate immune response. *Cell*, 146:448–461, 2011.

[212] H. Xu, X. He, H. Zheng, L. J. Huang, F. Hou, Z. Yu, M. J. de la Cruz, B. Borkowski, X. Zhang, Z. J. Chen, and Q-X. Jiang. Structural basis for the prion-like MAVS filaments in antiviral innate immunity. *eLife*, 3:e01489, 2014.

[213] K. Onoguchi, K. Onomoto, S. Takamatsu, M. Jogi, A. Takemura, S. Morimoto, I. Julkunen, H. Namiki, M. Yoneyama, and T. Fujita. Virus-infection or 5'ppp-RNA activates antiviral signal through redistribution of IPS-1 mediated by MFN1. *PLoS Pathog.*, 6:e1001012, 2010.

[214] M. Beck, F. Forster, M. Ecke, J. M. Plitzko, F. Melchior, G. Gerisch, and W. Baumeister. Nuclear pore complex structure and dynamics revealed by cryoelectron tomography. *Science*, 306:1387–1390, 2004.

[215] V. Chandran, R. Fronzes, S. Duquerroy, N. Cronin, J. Navaza, and G. Waksman. Structure of the outer membrane complex of a type IV secretion system. *Nature*, 462:1011–1015, 2009.

[216] S-H. Shim, C. Xia, G. Zhong, H. P. Babcock, J. C. Vaughn, B. Huang, X. Wang, C. Xu, G-Q. Bi, and X. Zhuang. Super-resolution fluorescence imaging of organelles in live cells with photoswitchable membrane probes. *Proc. Natl. Acad. Sci. USA*, 109:13978–13983, 2012.

Appendix A

Workflow

This appendix is intended to provide some idea of my workflow when programming, running programs I have written, and other related tasks.

For all three of my papers (chapters 4, 5, and 6), the programs to obtain the data were written in C. The only 'black box' routine I have used is a random number generator. All other parts of my programs are written from scratch using standard C functions.

The random number generator I use is ran1.c. This routine requires a seed to initiate the sequence of random numbers, and I draw the seed from the current time.

In my three papers, there is a variety of data taken, and the amount of runtime to obtain a data set can vary significantly. Data from chapter 4 ran no longer than overnight. Data from chapter 5 took up to two days to run. Data from chapter 6 took up to several hours to run.

Most of my data was obtained by running my programs on ACEnet. ACEnet is a consortium of universities in Atlantic Canada the provides computer clusters for researchers in the region. ACEnet clusters may be accessed over the internet. By running on ACEnet I have simultaneously ran hundreds of programs simultaneously. ACEnet allows users to submit to a queue to wait for computer use, and the system has rules which determine the queue position of programs based on the users recent ACEnet usage. There are three queues, which separate out programs asking for different amounts of runtime: short ($<$ 2 days runtime), medium (2 days - 1 week runtime), and long (1 week - 2 weeks runtime). The wait for a medium or long slot is usually much longer than the wait for a short slot. To minimize the wait for computer time, I have only used short slots, and all my code runs in two days or less.

The ACEnet process for submitting a job involves submitting a script to the queue, which can then call your program when the job is called to run by the queuing system. These scripts are standard, with information such as program location, runtime

requirement, memory requirement, and a name for the job. I separate each program I am running into a separate folder on ACEnet, and so I also used scripts to compile my program and submit the job script in each folder. My third use for scripts was to change parameters inside the code, so that the programs running in different folders were able to vary the parameter values.

The plotting program Gnuplot can perform fits to data sets, using a nonlinear least-squares Marquardt-Levenberg algorithm. I have used this function in gnuplot for some of my plots. To start you define a function to fit, e.g.

$$\text{f(x) = a*x + b.}$$

This is a linear equation, and we would want to find the values of the parameters a and b, given the data for $f(x)$ and x. The data needs to be in a file, e.g. data.dat. To instruct Gnuplot to find values for a and b, set initial values for a and b (e.g. $a = 1$ and $b = 2$), and type

$$\text{fit f(x) 'data.dat' via a, b.}$$

Gnuplot will then run the algorithm and print to the terminal window the estimated values of a and b.

I have also used the plotting program Gnuplot to make contour plots. This involves two scripts. The first script plots the (three-dimensional) data, except the usual plotting commands are bookended by setting and unsetting a table, so that the gnuplot plotting information is written to a file, e.g. colours.dat. The first script also sets up contours, selecting specific contour levels. The data is again written to file, this time holding the coordinates for contours, e.g. in contours.dat. The first script has produced a file containing plotting information, colours.dat, and a file containing contour information, contours.dat. The second script plots colours.dat, with contours.dat imposed on top so the contour lines are not blocked by the colour map of the image. To place contour labels in gaps of the contour lines, I simply instructed Gnuplot to print text labelling the lines at the desired coordinates, and opened the contour.dat file and removed the contour lines points at those coordinates to create a gap.

Appendix B

Permissions

Chapter 4 is the paper 'PEX5 and ubiquitin dynamics on mammalian peroxisome membranes', authored by Aidan I Brown (myself), Peter K Kim, and Andrew D Rutenberg, published in PLoS Computational Biology in 2014, volume 10, page e1003426, doi 10.1371/journal.pcbi.1003426. Under the PLOS Creative Commons Attribution License, the article is allowed to be downloaded, resused, reprinted, modified, distributed, and/or copied by anyone, so long as the original authors and source are cited, as they are immediately above.

Chapter 5 is the paper 'Cluster coarsening on drops exhibits strong and sudden size-selectivity', authored by Aidan I Brown (myself) and Andrew D Rutenberg, published in Soft Matter in 2015, volume 11, pages 3786-3793, doi 10.1039/C5SM00284B. The paper is reproduced by permission of The Royal Society of Chemistry (RSC). Authors of articles in journals of the Royal Society of Chemistry do not need to formally request permission to reproduce their article in their thesis or dissertation. For all cases of reproduction the correct acknowledgement should be given in the reproduced material, as it is above.